DESIGN AND DEVELOPMENT OF INTRICATE NANOMEDICAL DEVICES THROUGH COMPOSITIONAL, DIMENSIONAL AND STRUCTURAL CONTROL

A Dissertation

by

YUN LIN

Submitted to the Office of Graduate Studies of
Texas A&M University
in partial fulfillment of the requirements for the degree of

DOCTOR OF PHILOSOPHY

May 2012

Major Subject: Chemistry

Design and Development of Intricate Nanomedical Devices

through Compositional, Dimensional and Structural Control

DESIGN AND DEVELOPMENT OF INTRICATE NANOMEDICAL DEVICES THROUGH COMPOSITIONAL, DIMENSIONAL AND STRUCTURAL CONTROL

A Dissertation

by

YUN LIN

Submitted to the Office of Graduate Studies of
Texas A&M University
in partial fulfillment of the requirements for the degree of

DOCTOR OF PHILOSOPHY

Approved by:

Chair of Committee,	Karen L. Wooley
Committee Members,	Kevin Burgess
	Paul S. Cremer
	Melissa A. Grunlan
Head of Department,	David H. Russell

May 2012

Major Subject: Chemistry

ABSTRACT

Design and Development of Intricate Nanomedical Devices
through Compositional, Dimensional and Structural Control. (May 2012)

Yun Lin, B.S., University of Nebraska at Omaha;
M.S., Washington University in St. Louis
Chair of Advisory Committee: Dr. Karen L. Wooley

Nanomedicine, the medical application of nanotechnology, uses nanoscale objects that exist at the interface between small molecule and the macroscopic world for medical diagnosis and treatment. One of the healthcare applications of nanomedicine is drug delivery: the development of nanoscale objects to improve therapeutics' bioavailability and pharmacokinetics. Shell crosslinked knedel-like nanoparticles (SCKs), that are self assembled from amphiphilic block copolymers into polymeric micelles and then further stabilized with crosslinkers isolated throughout the peripheral shell layer, have been investigated for drug delivery applications that take advantage of their core-shell morphology and tunable surface chemistry. SCKs are attractive nanocarriers because the cores of the SCKs are used for sequestering and protecting guests. The readily adjustable shell crosslinking density allows for gating of the guest transport into and out of the core domain, while retaining the structural integrity of the SCKs. Moreover, the highly functionalizable shell surface provides opportunity for incorporation of targeting ligands for enhanced therapeutic delivery.

The optimization of nanoparticle size, surface chemistry, composition, structure, and morphology has been pursued towards maximization of the SCKs' therapeutic efficacy. With distinctively different dimensions, compositions and structures of the core and shell domains of SCKs, and an ability to modify each independently, probing the effects of each is one of the major foci of this dissertation. Utilization of a living radical polymerization technique, reversible addition-fragmentation chain transfer (RAFT) polymerization, has allowed for facile manipulation of the block lengths of the polymer precursors and thus resulted in various dimensions of the nanoparticles. SCKs constructed from poly(acrylic acid)-*b*-polystyrene (PAA-*b*-PS) with various chain lengths, have been investigated on the loading and release of doxorubicin (DOX). The effect of PEGylation on paclitaxel (PTX) loaded SCKs on the cell internalization and killing was investigated. Apart from chemotherapies, the SCKs were explored as antimicrobial agents by incorporating silver species. Conjugation of the SCK surface with a protein adhesin through amidation chemistry to promote epithelial cell targeting and internalization was developed. Nanoscale assemblies with complex morphologies constructed from a linear triblock copolymer was investigated. Furthermore, a highly multifunctional nanodevice for imaging and drug delivery functionalized with a chelator for radio-labeling, polyethylene glycol (PEG) for improved biodistribution, targeting ligands, a chromophore and a therapeutic agent was evaluated *in vivo* as active-targeted delivery of therapeutics.

DEDICATION

To my father, Zhen Lin and my mother Lizhong Yin

ACKNOWLEDGEMENTS

When I entered graduate school, I have never even heard of most of the topics that were covered in this dissertation, thus to be able to accomplish all the cutting-edge work included here is a surreal experience. Though only one person’s name appears on the cover of this dissertation, its production would not have been possible without many people’s contribution and guidance. I owe my greatest appreciation to all those people who have helped with the completion this dissertation and because of whom my graduate experience has been the one that I will cherish forever.

My deepest and most sincere gratitude is to my advisor, Dr. Karen L Wooley, for her guidance, support, patience and most importantly trust during my graduate study at both Washington University in St. Louis and Texas A&M University. I was most fortunate to have an advisor who has given me the freedom to explore on my own and develop self-sufficiency to grow as an independent thinker yet at the same time she had provided insightful advice and constructive criticism at different stages of my research to help me focus. Dr. Wooley has high expectations for me and she guides me to meet those expectations with constant support, encouragement and self-demonstration. I am grateful to her for holding me to a high research standard and enforcing strict validations, which has not only taught me to be a thorough research scientist, but a better person with positive and healthy attitude. I also want to thank my committee members, Dr. Kevin Burgess, Dr. Paul S. Cremer and Dr. Melissa A. Grunlan for their valuable advice, input and discussions towards the completion of this dissertation.

The majority work of this dissertation was a collaborative effort with many brilliant scientists from both industry and academia. I have learned tremendously and enjoyed the collaboration with Dr. Richard B. Dorshow and his team from Covidien Pharmaceuticals. Intellectual contributions from Dr. John N. Freskos, Dr. Jeng J. Shieh, Mr. Amolkumar Karwa, Dr. James G. Kostelc, Dr. Gary E. Cantrell, Dr. David Berberich, Dr. Dennis A. Moore, Dr. William McGhee, Dr. Thomas Rogers, Dr. Amruta R. Poreddy, and Dr. Raghavan Rajagopalan are greatly appreciated. Professor David A. Hunstad's brilliant ideas, insightful advice and professional opinions have yielded one of the most important chapters in this dissertation, the relationship with his group was a very enjoyable experience. I also want to thank Dr. Jeffery R. Leonard and Dr. Carolyn L. Cannon for allowing me to learn *in vitro/in vivo* techniques in their labs and performing experiments.

I would like to acknowledge many past and present Wooley group members' mentorship and friendship. Particularly, I would like to thank Dr. Andreas M. Nyström and Dr. Guorong Sun for teaching me many useful techniques and having many valuable discussions that helped me understand my research areas better. Support and care from many friends have not only helped me overcome setbacks and stay focused on my graduate study but in my life as well. I greatly value the friendship from Dr. Yali Li, Dr. Ke Zhang, Dr. Jeremy Bartles, Dr. Jiong Zou, Mr. Ang Li, Mr. Shiyi Zhang and Mr. Fuwu Zhang. I appreciate many faculty, staff members and colleagues from both Washington University in St. Louis and Texas A&M University department of chemistry for their help in many aspects of my graduate school career.

The most important person during my graduate school career other than my advisor is Dr. Nam S. Lee. Nam has believed in my ability to succeed even before I believed in myself. Nam’s meticulous work ethics, innovative spirit, and positive attitude have influenced me to be a better scientist and taking on challenges with full confidence. The accomplishments of my graduate school career and the completion of this dissertation are undeniably attributed to the encouragement, patience, support and dedication from Nam. I was able to concentrate on the writing of my dissertation because Nam assumed full responsibility of our Goldendoodle, Mulligan, and for that I owe him my deepest gratitude.

Most importantly, none of this would have been possible without the love of my Mom and Dad, to whom this dissertation is dedicated to. They have been a constant source of love, support, encouragement and strength all these years. I was unable to fulfill my daughterly duties during the study of my graduate school career; the accomplishments and achievements are a small token to express my sincere gratefulness towards their unwavering love, devotion and nourishments.

NOMENCLATURE

AFM	Atomic force microscopy
AIBN	2,2'-Azobis(isobutyronitrile)
CFU	Colony-forming unit
CMC	Critical micelle concentration
CTA	Chain transfer agent
DDMAT	*S*-1-dodecyl-*S*'-(α, α'-dimethyl-α''-acetic acid)trithiocarbonate
DLS	Dynamic light scattering
DMAP	4-(Dimethylamino)pyridine
DMF	*N*, *N*-Dimethylformamide
DMSO	Dimethyl sulfoxide
DOX	Doxorubicin
DP_n	Degrees of polymerization
DSC	Differential scanning calorimetry
EDCI	1-[3´-(dimethylamino)propyl]-3-ethyl-carbodiimide methiodide
EDDA	2,2´-(ethylenedioxy)bis(ethylamine)
EPR	Enhanced permeation and retention
FITC	Fluorescein isothiocyanate
GPC	Gel permeation chromatography
HOBt	1-Hydroxybenzotriazole hydrate
HPLC	High performance liquid chromatography

ICP-MS	Inductively coupled plasma mass spectrometry
IR	Infrared spectroscopy
MIC	Minimum inhibitory concentration
MWCO	Molecular weight cut-off
NAS	*N*-Acryloyloxysuccinimide
NHS	*N*-Hydroxysuccinimide
NMR	Nuclear magnetic resonance spectroscopy
PAA	Poly(acrylic acid)
PBS	Phosphate buffered saline
PDI	Polydispersity index
PEG	Poly(ethylene glycol)
PEO	Poly(ethylene oxide)
PS	Polystyrene
PTA	Phosphotungstic acid
P*t*BA	Poly(*tert*-butyl acrylate)
PTX	Paclitaxel
RAFT	Reversible addition-fragmentation chain transfer
SATP	*N*-succinimidyl-*S*-acetylthiopropionate
SANS	Small angel neutron scattering
SCK	Shell crosslinked knedel-like nanoparticle
SEC	Size exclusion chromatography
SDS	Sodium dodecyl sulfate

T_g	Glass transition temperature
T_m	Crystalline melting temperature
TEM	Transmission electron microscopy
TFA	Trifluoroacetic acid
THF	Tetrahydrofuran
UPEC	Uropathogenic strains of *Escherichia coli*
UTI	Urinary tract infections
UV-vis	Ultraviolet-visible

TABLE OF CONTENTS

Page

ABSTRACT iii

DEDICATION v

ACKNOWLEDGEMENTS vi

NOMENCLATURE ix

TABLE OF CONTENTS xii

LIST OF FIGURES xv

LIST OF TABLES xxiv

CHAPTER

I INTRODUCTION 1

II TUNING CORE *VS.* SHELL DIMENSIONS TO ADJUST THE PERFORMANCE OF NANOSCOPIC CONTAINERS FOR THE LOADING AND RELEASE OF DOXORUBICIN 14

- 2.1. Introduction 14
- 2.2. Materials and methods 18
- 2.3. Results and discussion 30
- 2.4. Conclusions 52
- 2.5. Acknowledgments 53

III PACLITAXEL-LOADED SCK NANOPARTICLES: AN INVESTIGATION OF LOADING CAPACITY AND CELL KILLING ABILITIES *IN VITRO* 54

- 3.1. Introduction 54
- 3.2. Materials and methods 57
- 3.3. Results and discussion 66
- 3.4. Conclusions 81
- 3.5. Acknowledgments 82

CHAPTER Page

IV SYNTHESIS, CHARACTERIZATION, AND *IN VIVO* EFFICACY EVALUATION OF SHELL CROSSLINKED NANOPARTICLE FORMULATIONS CARRYING SILVER ANTIMICROBIALS AS ANTI-PSEUDOMONAL THERAPEUTICS 83

4.1. Introduction 83
4.2. Materials and methods 88
4.3. Results and discussion.. 93
4.4. Conclusions 101
4.5. Acknowledgments 101

V SYNTHETIC POLYMER NANOPARTICLES CONJUGATED WITH FIMH$_A$ FROM *E. COLI* PILI TO EMULATE THE BACTERIAL MODE OF EPITHELIAL INTERNALIZATION 102

5.1. Introduction 102
5.2. Materials and methods 105
5.3. Results and discussion.. 110
5.4. Conclusions 116
5.5. Acknowledgments 118

VI MORPHOLOGICAL EVOLUTION OF A TRIBLOCK COPOLYMER AND CHEMICAL MANIPULATIONS THEREOF.. 119

6.1. Introduction 119
6.2. Materials and methods 122
6.3. Results and discussion.. 128
6.4. Conclusions 152
6.5. Acknowledgments 152

VII F3-PEPTIDE-CONJUGATED, DOXORUBICIN LOADED NANOPARTICLES AS COMPLEX THERANOSTICS IN THE TREATMENT OF PEDIATRIC BRAIN CANCERS 153

7.1. Introduction 153
7.2. Materials and methods 158
7.3. Results and discussion.. 167
7.4. Conclusions 179
7.5. Acknowledgments 179

VIII CONCLUSIONS 181

REFERENCES 187

VITA 206

LIST OF FIGURES

FIGURE Page

1.1 Schematic representation of the composition of multifunctional shell crosslinked knedel-like nanoparticles (SCKs) for drug delivery applications 4

1.2 Schematic representation of the interaction between doxorubicin (DOX) incorporated into SCKs constructed from poly(acrylic acid)-*b*-polystyrene (PAA-*b*-PS) 7

1.3 Schematic representation of the incorporation of PTX into SCKs and cell internalization of PTX-SCKs.................... 9

1.4 Schematic and chemical representation of a shell crosslinked nanoparticle assembled from poly(acrylic acid)-*b*-polystyrene loaded with silver carbene complexes in the core and silver cation in the shell.................... 10

1.5 Schematic representation of a shell crosslinked nanoparticle functionalized with FimH_A adhesin protein and confocal microscopy of the FimH_A-SCKs being internalized into bladder epithelial cells.................... 11

2.1 Preparation of P*t*BA macro-CTA, chain extension with styrene, and removal of *tert*-butyl protecting groups to produce PAA_m-*b*-PS_n polymers of various chain lengths.................... 32

2.2 Schematic representation of the supramolecular assembly of PAA_m-*b*-PS_n block copolymers into micelles and their subsequent crosslinking with EDDA to form SCKs.................... 35

2.3 Characterization of SCKs **12 - 15** by TEM (drop deposited on carbon-coated copper grids and stained negatively with phosphotungstic acid) of A) **12**, B) **13**, C) **14**, and D) **15** 36

2.4 Characterization of SCKs **12 - 15** by DLS**.** DLS histograms of intensity-averaged, volume-averaged, number-averaged hydrodynamic diameters : A) SCK **12**, B) SCK **13**, C) SCK **14**, and D) SCK **15** in nanopure water 37

FIGURE Page

2.5 A). Small angle neutron scattering (SANS) data of SCK **12 - 15**. Black solid lines present fitting curves of “smeared polydispersed core-shell sphere” model. B). Model fitting results for SANS profile of SCK **12** with "core-shell sphere" model, "smeared core-shell sphere" model, "polydispersed core-shell sphere" model and "smeared polydispersed core-shell sphere" model 39

2.6 Schematic representation of the loading of DOX into the core, core-shell interface and shell region of the SCKs while suspended in aqueous solution, and release of DOX from the SCK in pH 5.0 or pH 7.4 buffer at 37 °C 44

2.7 DOX release profiles of free DOX, micelles, and SCK**12**, SCK**13**, SCK**14** and SCK**15** at pH 7.4 or pH 5.0.. 45

2.8 Higuchi plots of DOX release profiles of SCK**12**, SCK**13**, SCK**14** and SCK**15** at pH 7.4 or pH 5.0 47

3.1 Co-assembly of PAA_{70}-*b*-PS_{555} block copolymers in DMF with paclitaxel in DMSO to construct 60 nm PTX-loaded micelles (PTX-micelle-60nm), followed by dialysis to remove the organic solvents. Crosslinking with the pyrazine chromophore crosslinker, using EDCI as the coupling agent followed by dialysis to remove free crosslinker and EDCI byproducts to obtain PTX-loaded SCKs (PTX-SCK-60nm) 67

3.2 Left column: TEM images (drop deposited on carbon-coated copper grids and stained negatively with 1% aqueous uranyl acetate) of A. SCK-60nm; C. PTX-SCK-60nm-20%; E. PTX-SCK-60nm-15%; G. PTX-SCK-60nm-10%; I. PTX-SCK-60nm-5%. Right column: DLS histograms (determinations were average values from ten measurements, with the standard deviations being calculated as the breadth of the distributions) of B. SCK-60nm; D. PTX-SCK-60nm-20%; F. PTX-SCK-60nm-15%; H. PTX-SCK-60nm-10%; J. PTX-SCK-60nm-5%................................... 69

3.3 Viability of KB cells incubated with A. SCK-60nm; B. Free PTX; C. PTX-SCK-60nm-20%; D. PTX-SCK-60nm-15%; E. PTX-SCK-60nm-10%; F. PTX-SCK-60nm-5%. The percentage cell viability was measured by WST-1 assay. Blue squares, 2 h; red diamonds, 72 h... 72

FIGURE Page

3.4 Illustration of the location of free PTX *vs*. PTX-SCK in a centrifugal filtering experiment using 50 kDa MWCO filter 73

3.5 Co-assembly of PAA-*b*-PS or PEGylated PAA-*b*-PS in DMF with PTX in DMSO to construct 20 nm PTX loaded micelles, followed by *in situ* crosslinking with the pyrazine chromophore crosslinker, using EDCI as the coupling agent. The final 20 nm PTX-loaded SCKs in aqueous solutions were obtained after performing dialysis to remove organic solvent, free crosslinker and EDCI by products........... 75

3.6 Left column: TEM images (drop-deposited on carbon-coated copper grids and stained negatively with 1% aqueous uranyl acetate) of A. SCK-20nm; C. PTX-SCK-20nm-5%; E. PEG-SCK-20nm; G. PTX-PEG-SCK-20nm-5%. Right column: DLS histograms (determinations were average values from ten measurements, with the standard deviations being calculated as the breadths of the distributions) of B. SCK-20nm; D. PTX-SCK-20nm-5%; F. PEG-SCK-20nm; H. PTX-PEG-SCK-20nm-5% 77

3.7 Viability of KB cells incubated with A. SCK-20nm; B. PEG-SCK-20nm; C. PTX-SCK-20nm-5%; D. PTX-PEG-SCK-20nm-5%. The percentage cell viability was measured by WST-1 assay. Blue squares, 2 h; red diamonds, 72 h... 79

3.8 Intracellular uptake of A. SCK-20nm; B. PEG-SCK-20nm; C. PTX-SCK-20nm-5%; D. PTX-PEG-SCK-20nm-5% in KB cells. Cells were incubated with a single concentration of each different type of SCK for 2 h. Cells were then fixed with 4% PFA, mounted with media containing DAPI, and subsequently imaged with Nikon A1 confocal microscope. Fragmented nuclei in cells were observed after incubation with PTX-SCK-20nm-5% for 2 h: E. DAPI staining; F. Transmission detector (TD) image; G. Acridine orange staining; H. Overlay of DAPI staining, TD, and acridine orange staining 80

4.1 Schematic representation of physical encapsulation of $AgNO_3$ or $AgCOOCH_3$ partitioned into the shell of the SCK, and silver carbene complex 10 (SCC10) being incorporated into the core of the SCK 94

FIGURE Page

4.2 TEM images (drop deposited on carbon-coated copper grids and stained negatively with 1% aqueous uranyl acetate) of: A. Empty SCK nanoparticles; B. $AgNO_3$-SCK; C. $AgCOOCH_3$-SCK, and D. SCC10-SCK 95

4.3 DLS histograms of intensity-averaged (first row), volume averaged (second row), and number averaged (third row) hydrodynamic diameters (determinations were average values from ten measurements, with the standard deviations being calculated as the breadth of the distributions) of: A. blank SCKs; B. $AgNO_3$-SCK; C $AgCOOCH_3$-SCK, and D. SCC10-SCK 96

4.4 STEM dark field images (drop deposited on carbon-coated copper grids with no stain) of A. $AgNO_3$-SCK; B. SCC10-SCK; and STEM bright field images (drop deposited on carbon-coated copper grids with no stain) of C. $AgNO_3$-SCK; D. SCC10-SCK 97

4.5 Wight loss diagram of mice inoculated with *P. aeruginosa* treated with sham, blank SCK, AgNO3-SCK, AgCOOCH3-SCK and SCC10-SCK treatment groups 99

4.6 Clinical score diagram of mice inoculated with *P. aeruginosa* treated with sham, blank SCK, AgNO3-SCK, AgCOOCH3-SCK and SCC10-SCK treatment groups 99

4.7 Percent survival rate diagram of mice inoculated with *P. aeruginosa* treated with sham, blank SCK, AgNO3-SCK, AgCOOCH3-SCK and SCC10-SCK treatment groups 100

5.1 Schematic and chemical representation of $FimH_A$-functionalized and FITC cadaverine-labeled SCK nanoparticles 104

5.2 A. Schematic representation of 5-FITC cadaverine labeling and $FimH_A$ conjugation to the shell of SCK nanoparticles *via* amidation chemistry; B. TEM and DLS characterization of 5-FITC cadaverine-tagged, $FimH_A$-conjugated SCK nanoparticles. Diameter (TEM) = 20 ± 3 nm, $D_{h(intensity)} = 80 \pm 30$ nm, $D_{h(volume)} = 50 \pm 20$ nm, $D_{h(number)} = 40 \pm 10$ nm.. 112

FIGURE Page

5.3 Functionalization of FimH_A onto SCK surfaces. Naked SCKs (A) and FimH_A-functionalized SCKs (B) viewed by immunogold transmission EM after incubation with rabbit anti-FimH_A antibody and gold-conjugated anti-rabbit IgG. Labeling of FimH_A-SCKs was significantly greater than that of naked SCKs; representative images are shown. Scale bars, 100 nm 113

5.4 Binding of FimH_A-SCK nanoparticles to cultured bladder epithelial cells. Monolayers of 5637 cells were treated with the indicated doses of 5-FITC cadaverine-tagged (green) SCKs, naked or conjugated with FimH_A, and with or without 2% mannose. Cells were liberated from the surface and stained circumferentially with AlexaFluor 594-conjugated wheat germ agglutinin (WGA; red). Scale bar (upper left panel), 20 µm 115

5.5 Epithelial cell internalization of FimH_A-SCKs. In this example of an internalized particle, the SCK of interest is viewed at the cross-hairs in the XY plane; orthogonal views (top and right of the panel) show the particle encircled by the red cell-surface stain (arrowheads). Scale bar, 20 µm 116

6.1 Schematic representation of self assembly of PEO_{45}-*b*-PNAS_{66}-*b*-PS_{30} to form both cylindrical nanostructure and multicompartment nanostructure: A. micellization in DMF to form cylindrical micelles; B. crosslinking with pyrazine crosslinker to form shell crosslinked cylindrical nanostructures (SCCN); C. SCCN after dialysis for 3 days; D. SCCN after 3 months storage at room temperature; E. cylindrical micelles after dialysis for 3 days; F. cylindrical micelles after 3 month storage at room temperature; G. micellization in DMSO to form multicompartment micelles (MCM); H. crosslinking with pyrazine crosslinker to form shell crosslinked multicompartment nanostructure (MCN); I. MCN after dialysis for 3 days; J. MCN after 3 months storage at room temperature. K. MCM disassembled into individual micelles upon dialysis; L. individual micelles disassembled from MCM are stable after 3 months storage at room temperature. 121

FIGURE Page

6.2 DLS histograms of intensity-averaged (first row), volume averaged (second row), and number averaged (third row) hydrodynamic diameters (determinations were average values from ten measurements, with the standard deviations being calculated as the breadth of the distributions) of PEO_{45}-*b*-$PNAS_{66}$-*b*-PS_{30} in DMF self assembled into cylindrical micelles upon addition of water at various water addition rate: A. 10 mL/h; B. 15 mL/h; C. 20 mL/h, and D. 30 mL/h. 129

6.3 TEM images (drop deposited on carbon-coated copper grids and stained negatively with 1% PTA) of PEO_{45}-*b*-$PNAS_{66}$-*b*-PS_{30} in DMF self assembled into cylindrical micelles upon addition of water at : A. 10 mL/h; B. 15 mL/h; C. 20 mL/h; and D. 30 mL/h. 130

6.4 TEM images (drop deposited on carbon-coated copper grids and stained negatively with 1% PTA) of the transition of PEO_{45}-*b*-$PNAS_{66}$-*b*-PS_{30} in DMF self assembled into spherical micelles to cylindrical micelles upon increased addition of water from: A. 10 wt%; B. 21 wt%; C. 32 wt%; to D. 41 wt% at a rate of 15 mL/h 132

6.5 DLS histograms of intensity-averaged (first row), volume averaged (second row), and number averaged (third row) hydrodynamic diameters (determinations were average values from ten measurements, with the standard deviations being calculated as the breadth of the distributions) of PEO_{45}-*b*-$PNAS_{66}$-*b*-PS_{30} shell crosslinked cylindrical nanoparticles (SCCN) dialyzed against A. nanopure water; B. pH 6.3 PBS; C. pH 7.4 PBS and D. pH 8.1 PBS.................................. 133

6.6 TEM images (drop deposited on carbon-coated copper grids and stained negatively with 1% PTA) of PEO_{45}-b-$PNAS_{66}$-b-PS_{30} cylindrical micelles dialyzed against A. nanopure water; B. pH 6.3 PBS; C. pH 7.2 PBS, and D. pH 8.0 PBS for 3 days................ 134

6.7 TEM images (drop deposited on carbon-coated copper grids and stained negatively with 1% PTA) of shell crosslinked cylindrical nanostructures (SCCN) dialyzed against A. nanopure water; B. pH 6.3 PBS; C. pH 7.2 PBS, and D. pH 8.0 PBS for 3 days. 137

FIGURE Page

6.8 TEM images (drop deposited on carbon-coated copper grids and stained negatively with 1% PTA) of cylindrical micelles dialyzed against A. nanopure water 6.3; B. pH 6.3 PBS; C. pH 7.2 PBS, and D. pH 8.0 PBS after 3 months of storage at room temperature. 138

6.9 TEM images (drop deposited on carbon-coated copper grids and stained negatively with 1% PTA) of shell crosslinked cylindrical nanostructures (SCCN) dialyzed against A. nanopure water; B. pH 6.3 PBS; C. pH 7.2 PBS, and D. pH 8.0 PBS after 3 months storage at room temperature 139

6.10 DLS histograms of intensity-averaged (first row), volume averaged (second row), and number averaged (third row) hydrodynamic diameters (determinations were average values from ten measurements, with the standard deviations being calculated as the breadth of the distributions) of PEO_{45}-*b*-$PNAS_{66}$-*b*-PS_{30} in DMSO self assembled.......... 141

6.11 TEM images (drop deposited on carbon-coated copper grids and stained negatively with 1% PTA) of PEO_{45}-*b*-$PNAS_{66}$-*b*-PS_{30} in DMSO self assembled into MCM upon addition of water at : A. 10 mL/h; B. 15 mL/h; C. 20 mL/h; and D. 30 mL/h. 142

6.12 TEM images (drop deposited on carbon-coated copper grids and stained negatively with 1% PTA) of the transition of PEO_{45}-*b*-$PNAS_{66}$-*b*-PS_{30} in DMSO self assembled into spherical micelles to MCMs upon increased addition of water from: A. 9 wt%; B. 19 wt%; C. 31 wt%; to D. 40 wt% at a rate of 15 mL/h 144

6.13 DLS histograms of intensity-averaged (first row), volume averaged (second row), and number averaged (third row) hydrodynamic diameters (determinations were average values from ten measurements, with the standard deviations being calculated as the breadth of the distributions) of PEO_{45}-*b*-$PNAS_{66}$-*b*-PS_{30} MCM dialyzed against A. nanopure water; B. pH 6.3 PBS; C. pH 7.4 PBS and D. pH 8.1 PBS. 146

FIGURE Page

6.14 TEM images (drop deposited on carbon-coated copper grids and stained negatively with 1% PTA) of MCMs retained structure integrity when dialyzed against A. nanopure water but disassembled into individual nanoparticles upon dialysis against B. pH 6.3 PBS; C. pH 7.2 PBS, and D. pH 8.0 PBS for 3 days.. 148

6.15 TEM images (drop deposited on carbon-coated copper grids and stained negatively with 1% PTA) of MCM dialyzed against A. nanopure water; B. pH 6.3 PBS; C. pH 7.2 PBS, and D. pH 8.0 PBS after 3 months of storage at room temperature................. 149

6.16 TEM images (drop deposited on carbon-coated copper grids and stained negatively with 1% PTA) of MCNs dialyzed against A. nanopure water; B. pH 6.3 PBS; C. pH 7.2 PBS, and D. pH 8.0 PBS for 3 days with retention to morphology.......................... 150

6.17 TEM images (drop deposited on carbon-coated copper grids and stained negatively with 1% PTA) of MCNs dialyzed against A. nanopure water; B. pH 6.3 PBS; C. pH 7.2 PBS, and D. pH 8.0 PBS after 3 months storage at room temperature..................... 151

7.1 Schematic representation of synthesis of DOTA containing PEGylated PAA_{52}-*b*-PS_{30} with activated ester-functionalized PEG, PAA_{45}-*g*-$(CONH\text{-lysine-DOTA-COOH})_3$-*g*-$(CONH\text{-}PEG_{3kDa}\text{-}NHCO\text{-}C_3H_6\text{-}SCOCH_3)_2$-*g*-$(CONH\text{-}PEG_{2kDa}\text{-}OMe)_2$-*b*-$PS_{30}$ 169

7.2 Schematic representation of incorporation of cascade blue dye with sulfo-NHS onto the polymer backbone segments within the shell of the SCKs, conjugation of maleimide-functionalized F3 peptide onto the thiol functionalized PEG graft termini to produce F3-CB-SCK **7**, followed by encapsulation of DOX into the nanoparticles through physical encapsulation to produce F3-CB-DOX-SCK **8**........................... 171

FIGURE Page

7.3 Upper row: A. TEM image (drop deposited on carbon-coated copper grids and stained negatively with 1% aqueous uranyl acetate) of SCK, diameter = 8 ± 3 nm; DLS histograms (determinations were average values from ten measurements, with the standard deviations being calculated as the breadth of the distributions) of B. SCK intensity average, 130 ± 60 nm; C. SCK volume average, 40 ± 20 nm; D. SCK number average 26 ± 6 nm; Lower row: E. TEM image of F3-CB-DOX-SCK, diameter = 7 ± 3 nm; DLS histograms of F. F3-CB-DOX-SCK intensity average, 100 ± 70 nm; G. F3-CB-DOX-SCK volume average, 30 ± 10 nm; H. F3-CB-DOX-SCK number average, 21 ± 4 nm 173

7.4 Cellular uptake of FITC labeled F3 peptide in primary normal human astrocytes (NHA) and U87MG glioma cells. Primary normal human astrocytes and U87MG glioma cells were both incubated with FITC-labeled F3 peptide (1µM) at 37 °C for 2 h before fixed with 4% PFA and then mounted for observation. As a control, U87MG glioma cells were pre-incubated with anti-human specific nucleolin antibody (10µg/ml) to block the binding. The nuclei were counterstained with DAPI 174

7.5 Live cell imaging of cellular uptake of untargeted DOX-loaded (DOX-SCK) *vs.* targeted DOX-loaded (F3-DOX-SCK) nanoparticles (at 1 µg/mL x 1 h) into U87MG glioma cells, 20 x magnifications. DOX molecules were shown by intrinsic red fluorescence within the treated cells 176

7.6 Enhanced tumor cell killing effects by F3-DOX-SCK nanoparticle *in vitro* compared with non-targeted SCKs. U87MG glioma cells were treated with naked SCK, DOX-SCK or F3-DOX-SCK for 3 days before assayed for their viability by MTT assay................................ 177

7.7 Enhanced tumor specific delivery of targeted nanoparticle in U87MG intracranial xenograft *in vivo* of targeted nanoparticles, F3-CB-DOX-SCK, compared with systemic distribution with non-targeted nanoparticles, CB-DOX-SCK, especially within the heart, kidney and liver 178

LIST OF TABLES

TABLE Page

2.1 Experimental and calculated dimensions of the SCKs, and quantified DOX loading values 40

2.2 DOX release rate, k ($h^{-½}$), obtained from fitting drug release experimental data to the Higuchi model 48

2.3 Difference factor (f_1) values of SCK**12**-SCK**15** against free DOX or against micelles as the references 50

2.4 Difference factor (f_1) values of SCK**12**-SCK**15** against each other as references 50

2.5 Similarity factor (f_2) values of SCK**12**-SCK**15** against free DOX or against micelles as the references 51

2.6 Similarity factor (f_2) values of SCK**12**-SCK**15** against each other as references 51

3.1 Summary of characterization data for 60 nm SCKs by TEM and DLS 68

3.2 Summary of various formulations of PTX-loaded SCKs (IC_{50} values were measured at both 2 h and 72 h incubation periods when incubated with KB cells *in vitro*) 71

3.3 Summary of characterization data for the 20 nm SCKs by TEM and DLS 76

3.4 Summary of various formulations of PTX-loaded SCKs (IC_{50} values were measured at both 2 h and 72 h incubation periods when incubated with KB cells *in vitro*) 78

4.1 Summary of characterization data for empty and silver-loaded SCK nanoparticles by TEM and DLS 95

6.1 Summary of characterization data for cylindrical micelles assembled from PEO_{45}-*b*-$PNAS_{66}$-*b*-PS_{30} in DMF by TEM and DLS 131

TABLE Page

6.2 Summary of characterization data for PEO_{45}-*b*-$PNAS_{66}$-*b*-PS_{30} cylindrical micelles dialyzed against nanopure water and PBS by TEM and DLS 135

6.3 Summary of characterization data for MCMs assembled from PEO_{45}-*b*-$PNAS_{66}$-*b*-PS_{30} in DMSO by TEM and DLS 143

6.4 Summary of characterization data for PEO_{45}-*b*-$PNAS_{66}$-*b*-PS_{30} MCMs dialyzed against nanopure water and PBS by TEM and DLS 147

CHAPTER I

INTRODUCTION

The medical application of nanotechnology, known as nanomedicine, concerns the use of precisely engineered materials at nanoscale for medical diagnosis and treatment. One of the dominating healthcare applications of nanomedicine that accounts for three-quarters of the research activity and market is drug delivery.[1] The development of nanoscopic objects that are able to improve the bioavailability and pharmacokinetics of therapeutics to achieve controlled drug delivery through modification of their fundamental properties such as solubility, blood circulation time, toxicity, diffusivity and immunogenicity is the prime focus of drug delivery.[2]

In the last two decades, we have witnessed an explosive expansion of nanoparticle-based therapeutics both in the market and clinical development for treatment of broad spectrum of diseases including cancer (Doxil® /Caelyx®, Myocet®), leukemia (Oncaspar®), viral infection (Abelcet®, AmBisome®) and hepatitis (Pegasys®, Epaxal®) *etc*.[2] The main route of administration for most nanoparticle-based therapeutics is through intravenous (i.v.) injection, other administration methods including subcutaneous (s.c.), intrathecal (i.t.), intravitreous (i.r.), intramuscular (i.m.) injection, and less invasive route such as oral, epidural, topical, and mucosal delivery

---

This dissertation follows the style of *Journal of the American Chemical Society*.

are also under rigorous investigations.[3] All of these routes require sophisticated design of the nanoparticles to be able to cross different biological barriers such as skin, blood, mucus, extracellular matrix before eventually delivering the payloads through the cellular and subcellular barriers.[3]

Nature has often provided the concepts and templates from which simple structures can be fabricated to provide excellent performances as hosts for packaging and releasing therapeutic guests.[4] For instance, viruses and lipoproteins are stealthy, naturally-occurring vehicles for targeted delivery of nucleic acids and cholesterol esters, respectively. Both viruses and lipoproteins feature architectural characteristics that would be favorable for a drug delivery system, such as: 1) nanoscopic dimensions to protect guest molecules having limited stability from their surroundings; 2) availability and accessibility of targeting moieties on the surface to achieve localized delivery; 3) robust and stealth structural integrity.[5-7] Although the synthetic and biological processes for tailoring of such natural vehicles have witnessed significant advance,[8-15] synthetic materials provide unique opportunities, including versatility of structure and composition, facile engineering, variation of parameters, control of stability *vs*. degradability, and avoidance of potential immunological effects.[16]

Polymer micelles, assembled from amphiphilic block copolymers, which mimic biological entities have been investigated for a number of potential applications that take advantage of their core-shell morphology and tunable surface chemistry.[5,17-22] The core-shell architecture enables the polymer micelle to incorporate hydrophobic drugs into the core domain that serves as a non-aqueous reservoir *via* either physical entrapment or covalent linkages, thereby increasing the solubility and stability of the hydrophobic drugs under physiological conditions. The shell domain, in turn, can protect the drug from its surroundings, modulating the pharmacokinetics and disposition of the carrier, and allowing manipulation over the surface chemistry.[23] However, micelles can only maintain their morphological integrities at concentrations above the critical micelle concentration (CMC) and are dynamic systems, potentially limiting their use as injectable drug carriers. Structural reorganization of the micellar structure will then result in dissociation of the therapeutic cargo and loss of sustained/controlled delivery. In addition, the polymeric assembly is subjected to change upon altering parameters in the surrounding environment, *e.g.*, ionic strength, pH, *etc*.[24-27]

To overcome the limitations that the CMC of micelles poses on intravenous-type drug carriers,[28-31] our research group and others have explored crosslinked micellar constructs, such as shell crosslinked knedel-like nanoparticles (SCKs), that combine the amphiphilic core-shell morphology of polymer micelles with stabilizing crosslinkers isolated throughout the peripheral shell layer. Due to the regioselective crosslinks in the peripheral shell region, these nanoscale assemblies can be diluted without disassembly, and have increased dimensional stability compared to their non-crosslinked micellar counterparts.[4,32-34] The core of the SCKs can retain its host capabilities, because the lack of crosslinks in the core region maintains chain mobility and access to the core volume, for sequestering of guests.[35-37] Moreover, just as in the case of macroscopic crosslinked networks originating from linear polymers, the readily adjustable shell crosslinking density allows for gating of the transport of those guests into and out of the core domain, while retaining the structural integrity of the SCK nanostructures (Figure 1.1). SCK nanoparticles resemble the naturally-occurring vehicles and are a versatile drug delivery system with features including: nanosize scale, core/shell architecture, covalent stabilization, stimuli responsiveness, packaging of therapeutic cargos, solubilization of hydrophobic payloads and selective cellular uptake when functionalized with targeting ligands.[38]

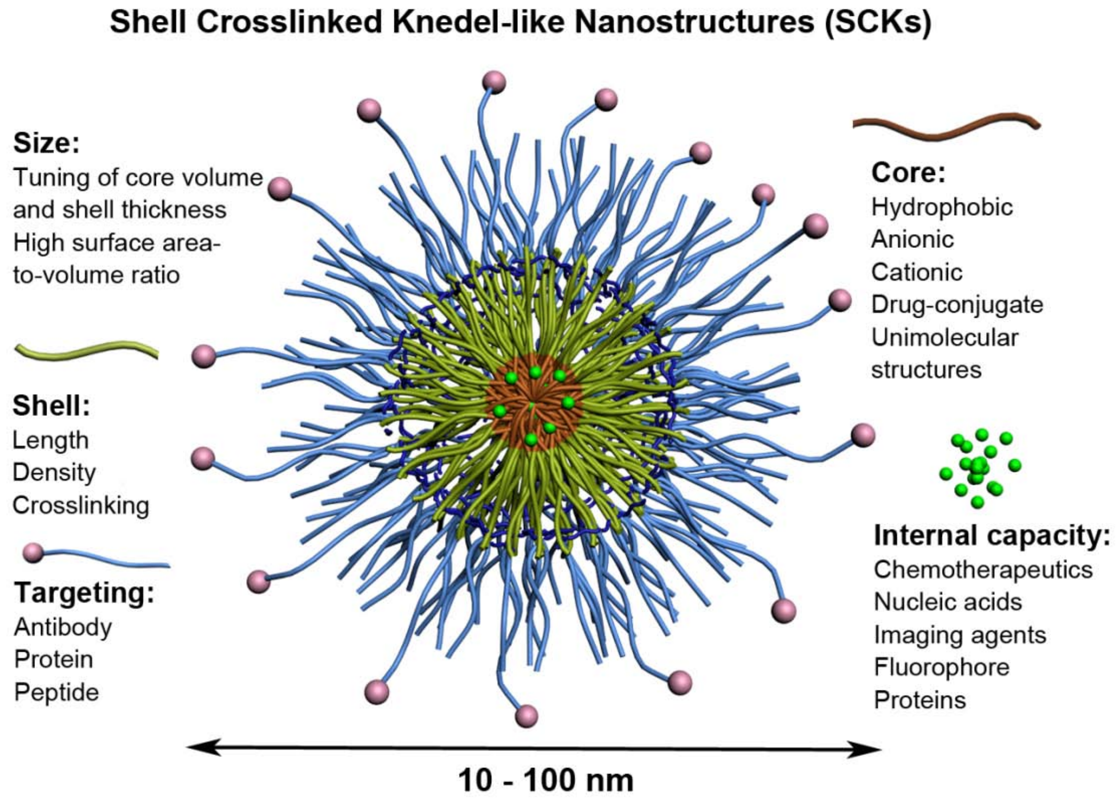

Figure 1.1. Schematic representation of the composition of multifunctional shell crosslinked knedel-like nanoparticles (SCKs) for drug delivery applications.

With the distinctively different dimensions, compositions and structures of the core and shell domains of SCKs, and an ability to modify each independently, probing the effects of each is of great interest. Advances in controlled radical polymerization have enabled the fabrication of these nanomaterials with precise control over size, shape, morphology, architecture, surface charge and functionalization. Facile tuning of these nanoscale dimensions arose from the ability to control the length of hydrophilic/hydrophobic units of the block copolymers that served as the building blocks for the nanoparticles. Probing the drug release effects of the particle dimensions on the nanoscale, may be accomplished through the synthesis of block copolymer precursors with different block lengths, thereby creating micelles with independently tuned core/shell sizes.

In Chapter II, in an effort to better understand the effects of the core and shell dimensions, and the parameters governing the loading and release of a chemotherapy small molecule drug, doxorubicin (DOX), in SCK nanoparticles, we have prepared SCKs with retention of the core and shell compositions, while varying the overall amphiphilic particle dimensions, including differentiation of the hydrophobic particle core size and hydrophilic, ionic shell thickness, independently (Figure 1.2).[39] Effects of composition were held constant, by employing SCKs constructed from a single type of amphiphilic diblock copolymer, poly(acrylic acid)-*b*-polystyrene (PAA-*b*-PS), having different relative block lengths and absolute chain lengths were synthesized *via* sequential reversible addition-fragmentation chain transfer (RAFT) polymerization reactions of *t*-butyl acrylate (*t*BA) and styrene, followed by removal of the *t*-butyl ester protecting groups. A series of four SCK nanoparticle samples, ranging in number-average hydrodynamic diameter from 14-30 nm, was prepared from four block copolymers having different relative block lengths and absolute degrees of polymerization. The ratios of acrylic acid to styrene block lengths ranged from 0.65 to 3.0, giving SCKs with ratios of shell to core volumes ranging from 0.44 to 2.1. The SCKs were capable of being loaded with 340-2200 DOX molecules per each particle, with larger numbers of DOX molecules packaged within the larger core SCKs. Their shell-to-core volume ratio showed impact on the rates and extents of release of DOX, with the volume occupied by the poly(acrylic acid) shell relative to the volume occupied by the polystyrene core correlating inversely with the diffusion-based release of DOX. Higher final extents of release and faster rates of release were observed for all DOX-loaded particle samples at pH 5.0 *vs*. pH 7.4, respectively, *ca*. 60% *vs*. 40% at 60 h, suggesting promise for enhanced delivery within tumors and cells. As the relative proportion of PAA shell to PS core volumes decreased, the rate and extent of release increased. Because these proportions are conveniently tuned by the nature of the block copolymer precursor, SCK nanoparticles offer enormous opportunity for the production of nanoscopic drug carriers with finely-tuned performance potential. These studies, therefore, point to future directions to craft sophisticated devices for controlled drug release.

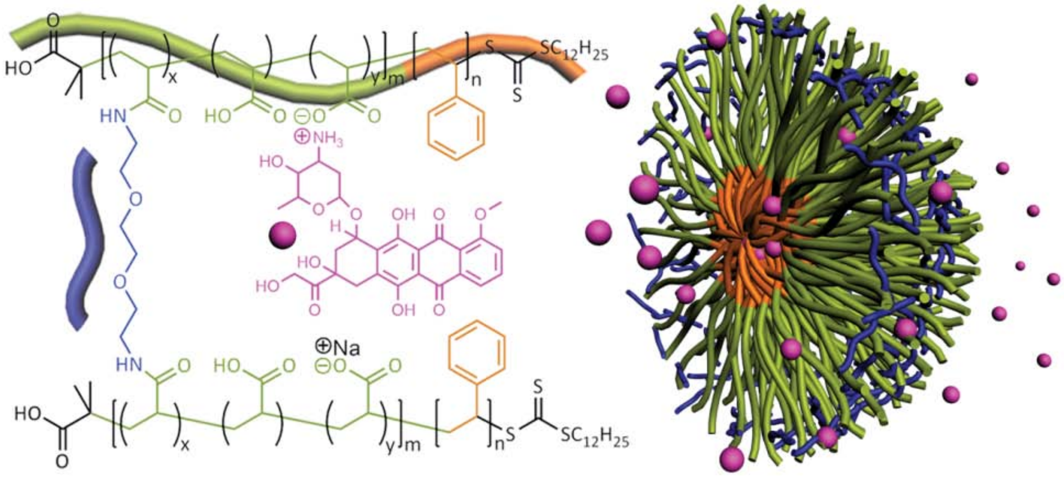

Figure 1.2. Schematic representation of the interaction between doxorubicin (DOX) incorporated into SCKs constructed from poly(acrylic acid)-*b*-polystyrene (PAA-*b*-PS).

The efficacy of nanoparticle-based drug delivery system is known to be limited by physiological barriers that are classified as external barriers (skin, mucus), *en route* barriers (blood, renal clearance, hepatic and splenic clearance, blood brain barriers and extracellular matrix), and cellular barriers (cellular uptake, endocytosis, cytoplasm and exocytosis).[3] Thus, it is crucial to control the size when designing nanoparticles for drug deliver applications because it can greatly influence the circulation time, clearance, selective tissue distribution and intracellular fate. Polymeric nanoparticles that are within the 20 to 100 nm range are large enough to avoid renal and lymphatic clearance and small enough to avoid opsonization, therefore, have the highest potential for *in vivo* applications. In Chapter III, towards the goal of an enhanced safety profile and increased efficacy, paclitaxel was encapsulated in amphiphilic, SCK nanoparticles (PTX-SCKs) as a novel drug delivery system (Figure 1.3). Paclitaxel-loaded SCK nanoparticles were synthesized from PAA-*b*-PS, in which PTX was encapsulated into the SCK nanoparticles through a co-assembly process at various concentration formulations. The *in vitro* cell killing ability was investigated on two different sizes of PTX-loaded SCKs, having core diameters of 20 ± 3 nm or 60 ± 5 nm and overall hydrodynamic diameters of 50 ± 15 nm or 120 ± 30 nm, respectively. Variable paclitaxel loading (5 to 20 wt% with respect to polymer weight) was prepared for their *in vitro* cytotoxicity evaluation. A dual purpose small molecule, pyrazine-based dye, served both as the crosslinker and fluorescent tag for visualization of cell internalization in KB cells by confocal fluorescence microscopy. Empty nanoparticles did not show any inherent cytotoxicity even at their highest concentration, whereas paclitaxel-loaded nanoparticles resulted in IC_{50} values that were better than free paclitaxel at 2 h incubation periods, and approximately equal to free paclitaxel at 72 h continuous incubation. Furthermore, the effects of PEGylation were evaluated for the smaller SCK samples.

PEGylation and the length and number of poly(ethylene oxide) (PEO) chains per nanoparticle have been shown to produce significant differences in blood circulation times and elimination in clearance organs for polymer nanoparticles.[40] Functionalization of the nanoparticle surfaces with PEO (2 kDa PEO, 5 PEO per block copolymer chain) did not affect the loading of paclitaxel or cell kill ability. Separation assays with high molecular weight cut-off filters confirmed that the paclitaxel was loaded within the nanoparticles and not free in solution. Thus, successful preparation of PTX-loaded, functional nanoparticles with varying sizes and surface characteristics were achieved, and all of which demonstrated cell killing abilities that were comparable to or better than free PTX.

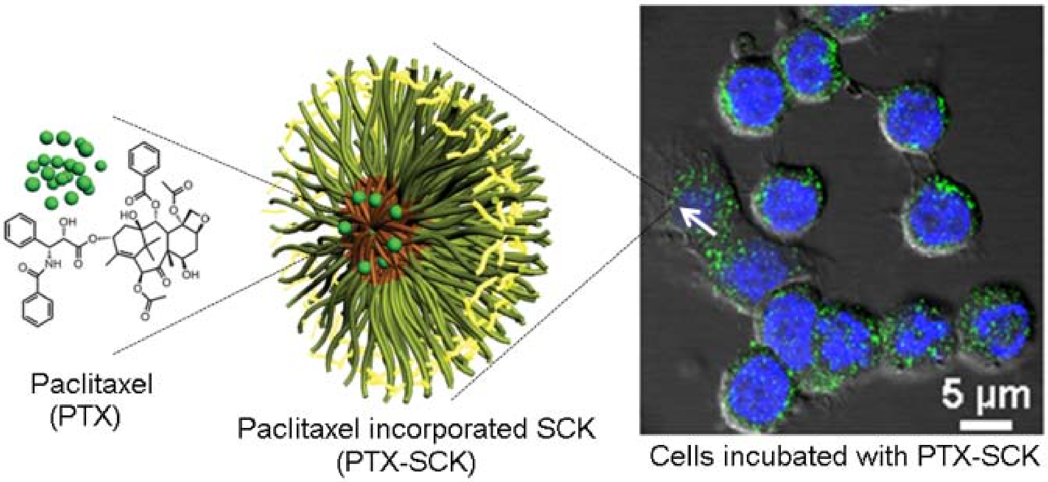

Figure 1.3. Schematic representation of the incorporation of PTX into SCKs and cell internalization of PTX-SCKs.

Apart from chemotherapy delivery, SCKs are also explored as antimicrobial therapeutics for the treatment of *Pseudomonas aeruginosa* caused lung infections associated with cystic fibrosis (CF). In Chapter IV, SCK constructed from self assembly of PAA-*b*-PS was able to encapsulate hydrophobic silver carbene complexes (SCC) into the hydrophobic polystyrene domain and complex silver cation to the acrylic acid residues on the shell of the nanoparticles (Figure 1.4). The incorporated silver concentration was determined by inductively coupled plasma mass spectrometry (ICP-MS) and the location of the silver specie are revealed by high resolution scanning transmission electron microscopy (STEM) coupled with energy dispersive X-ray spectroscopy (EDX). The therapeutic efficacy of the silver-loaded SCKs is investigated *in vivo* through nebulization treatment in *P. aeruginosa* infected mice.

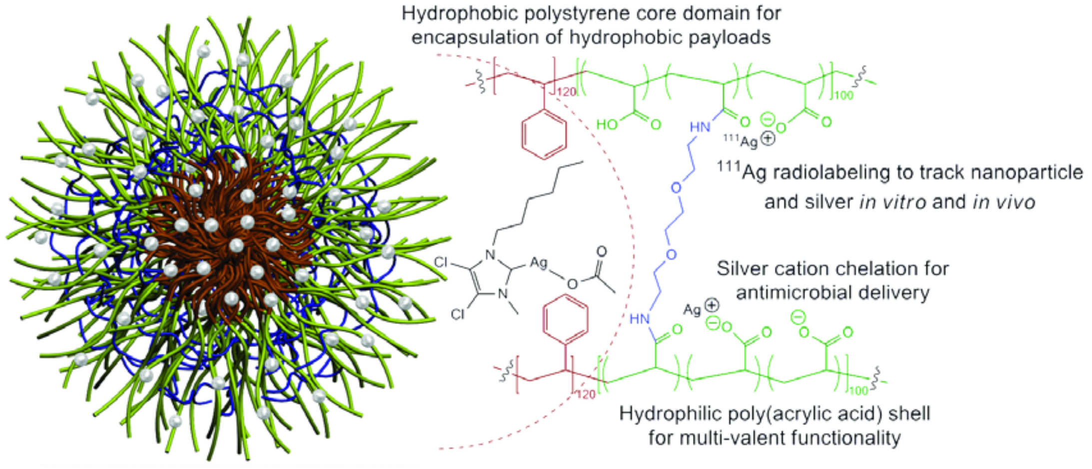

Figure 1.4. Schematic and chemical representation of a shell crosslinked nanoparticle assembled from poly(acrylic acid)-*b*-polystyrene loaded with silver carbene complexes in the core and silver cation in the shell.

SCKs as antimicrobial therapeutics can also be used as treatment of urinary tract infections (UTI) caused by uropathogenic strains of *Escherichia coli* (UPEC). UPEC is able to attach to superficial bladder epithelial cells, mediated by an adhesin protein, FimH$_A$. In Chapter V, we have developed nanoparticle carriers that bind and enter bladder epithelial cells to deliver antimicrobial agents directly to the niche occupied by these harbored bacteria by emulating the bacterial mode of invasion. In this study, we have designed SCKs that can be conjugated with FimH$_A$ for bladder epithelial cell binding and internalization, for the purpose of targeted delivery of various antimicrobial agents for the treatment and prevention of UTIs. The acrylic acid residues on the surfaces and throughout the shell layers of the SCKs were utilized for amidation with native lysines of FimH$_A$ to conjugate the adhesin and promote epithelial cell targeting and internalization, and with the amine terminus of the fluorescein-based dye, 5-((5-aminopentyl)thioureidyl)fluorescein (FITC cadaverine) to permit fluorescence microscopic imaging. By fluorescence microscopy the association of SCKs with the cell surfaces was shown to be dose dependent, FimH$_A$ specific, and inhibited by addition of mannose to the medium (Figure 1.5).

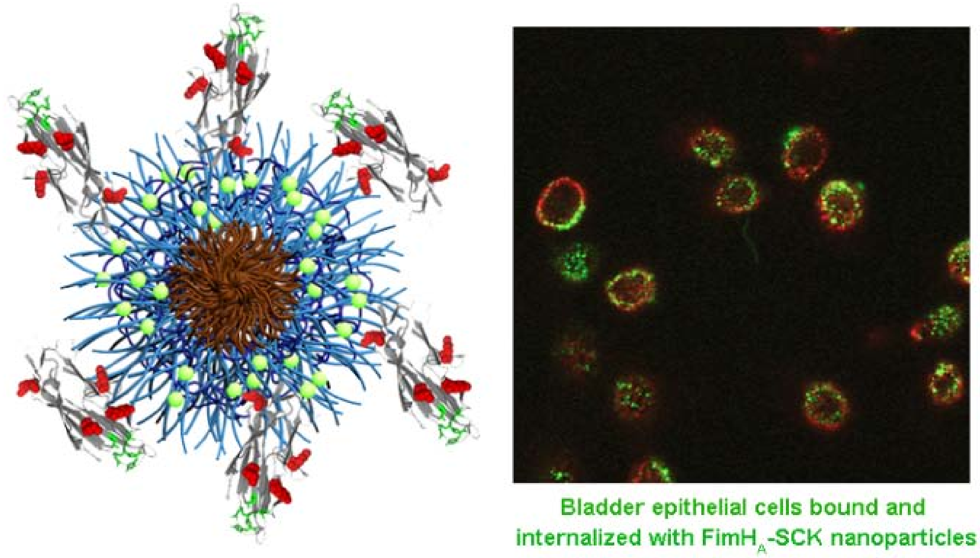

Figure 1.5. Schematic representation of a shell crosslinked nanoparticle functionalized with FimH$_A$ adhesin protein and confocal microscopy of the FimH$_A$-SCKs being internalized into bladder epithelial cells.

We have investigated parameters including size, surface chemistry, conjugation chemistry as well as different therapeutic cargos of spherical nanoparticles constructed from a simple diblock copolymer PAA-*b*-PS as drug delivery system. Chapter VI discusses the versatile morphologies to which a triblock copolymer can access. Building upon our understanding of drug gating properties, hydrophilic/hydrophobic drug encapsulation and release and bioconjugation, these complex nanoscale structures can further be utilized towards construction of next generation therapeutic material. The construction of both cylindrical and multicompartment nanostructure with a single type of linear triblock copolymer of PEO_{45}-*b*-$PNAS_{66}$-*b*-PS_{30} was achieved, and their assembly and disassembly processes were studied.

In Chapter VII, we have combined everything we have investigated in the previous chapters, including size, surface chemistry, conjugation of targeting ligands into an all-in-one system to produce the multifunctional SCK nanoparticles. Multifunctional SCKs were constructed from amphiphilic block copolymer to achieve coincident imaging and treatment of diseases through functionalization with polyethylene glycol (PEG) to inhibit surface protein adsorption, chromophores for imaging and tracking, and angiogenesis marker targeting ligands, F3 peptide, for active targeting and then finally loaded with DOX, to accomplish *in vivo* delivery of DOX for the treatment of brain cancer. The SCKs originated from the amphiphilic block copolymer, PAA-*b*-PS that were pre-functionalized with a total number of 5 PEGs: *ca.* two and a half 2-kDa methoxy-terminated PEG chains (PEG_{2k}) and two and a half 3-kDa mono-Boc-protected diamino PEGs (PEG_{3k}) per polymer chain, in order to extend the blood circulation time and introduce sites for surface conjugation of F3 targeting ligands. Removal of the Boc group allowed for PEG_{3k} chain ends to undergo amidation reactions with N-succinimidyl-S-acetylthiopropionate to introduce an acetyl-protected thiol at the end of the PEG_{3k} graft. Following self assembly of the block copolymer into micelles and subsequent crosslinking, the SCKs were further functionalized within the PAA shell layer with cascade blue immunofluorescence dye to allow for *ex vivo* visualization of the nanoparticles by antibody binding of histological tissue slices. The acetyl-protected thiol bearing SCKs were deprotected to reveal the thiol functionality and reacted with a maleimide-functionalized targeting ligand, F3 peptide. The cascade blue-labeled, F3 peptide-conjugated SCKs were then loaded with DOX through physical encapsulation and evaluated for their cytotoxicity against U87MG glioma cells *in vitro*. SCKs demonstrated IC_{50} values that were comparable to free DOX. Contrary to untargeted SCKs, which showed accumulation to perinuclear regions of U87MG glioma cells *in vitro* and systemic distribution throughout the heart, kidney and liver *in vivo*; F3 peptide-conjugated SCKs were able to achieve nuclear localization of the doxorubicin *in vitro* and enhanced uptake into U87MG intracranial xenografts *in vivo*.

In summary, the scope of this dissertation is focused on the design and development of polymeric nanoparticles for their application in biomedical and nanomedicine field. Fundamental parameters of the nanoparticles, including size, surface chemistry, chemical modification techniques and morphology evolution are investigated. It is anticipated that those fundamental studies will have great impact on the development of next generation nanomaterials in therapeutic delivery applications.

CHAPTER II

TUNING CORE *VS.* SHELL DIMENSIONS TO ADJUST THE PERFORMANCE OF NANOSCOPIC CONTAINERS FOR THE LOADING AND RELEASE OF DOXORUBICIN*

2.1. Introduction

Synthetic materials that are capable of sequestering, containing and releasing biologically-active agents have been of great interest for many years, as drugs and drug delivery systems. Inspiration for the designs of such materials comes from a variety of microparticles for, ideally, irreversible sequestration of bile acids or phosphates has led to the development of polymer drugs for lowering of serum cholesterol (e.g. WelChol®) or phosphate levels (e.g. Renagel®), respectively. Most often, however, synthetic materials are expected to retain their guests for a limited period of time and then allow for their release at controlled rates and under predetermined conditions. Such situations sources. For instance, the translation of polymeric ion-exchange resins into demand higher degrees of engineering complexity with respect to the synthetic material structure, composition, and morphology.

---

*Reprinted with permission from Lily Yun Lin, Nam S. Lee, Jiahua Zhu, Andreas M. Nyström, Darrin J. Pochan, Richard B. Dorshow and Karen L. Wooley, *J. Controlled Release*, **2011**, *152*, 37-48, Copyright 2012 Elsevier.

Nature has often provided the concepts and templates from which simple structures can be fabricated to provide sophisticated performances as hosts for packaging and releasing therapeutic guests.[4] For instance, viruses and lipoproteins are stealthy, naturally-occurring vehicles for targeted delivery of nucleic acids and cholesterol esters, respectively. Both viruses and lipoproteins feature architectural characteristics that would be favorable for a drug delivery system, such as: 1) nanoscopic dimensions to protect guest molecules having limited stability from their surroundings; 2) availability and accessibility of targeting moieties on the surface to achieve localized delivery; 3) robust and stealth structural integrity.[6,7,18] Although the synthetic and biological processes for tailoring of such natural vehicles have witnessed significant advance,[8-15] synthetic materials provide unique opportunities, including versatility of structure and composition, facile engineering, variation of parameters, control of stability *vs*. degradability, and avoidance of potential immunological effects.[16]

Polymer micelles, assembled from amphiphilic block copolymers, which mimic biological entities have been investigated for a number of potential applications that take advantage of their core-shell morphology and tunable surface chemistry.[5,17-22] The core-shell architecture enables the polymer micelle to incorporate hydrophobic drugs into the core domain that serves as a non-aqueous reservoir *via* either physical entrapment or covalent linkages, thereby increasing the solubility and stability of the hydrophobic drugs under physiological conditions. The shell domain, in turn, can protect the drug from its surroundings, modulating the pharmacokinetics and disposition of the carrier, and allowing manipulation over the surface chemistry.[23] However, micelles can only maintain their morphological integrities at concentrations above the critical micelle concentration (CMC) and are dynamic systems, potentially limiting their use as injectable drug carriers. Structural reorganization of the micellar structure will then result in dissociation of the therapeutic cargo and loss of sustained/controlled delivery. In addition, the polymeric assembly is subjected to change upon altering parameters in the surrounding environment, *e.g.*, ionic strength, pH, *etc*.[24-27] Such factors have been used as a trigger for controlled release in specific tissue, such as in acidic tumor environments.[41] Block copolymer micellar assemblies have also taken advantage of hydrolytically-degradable polymer segments to mediate their controlled release performances, such as those derived from lactide and/or glycolide, for which a rich literature describes extensive study of their physical, chemical and biological properties in their utilization as platforms for drug packaging and release.[42-49] Most recently, Park and co-workers reported successful preparation of monodisperse microparticles arising from biodegradable poly(lactic-*co*-glycolic acid) through a top-down hydrogel template strategy--a unique nanofabrication method that allowed for control over the dimensions of these microparticles. Through release studies of various drug molecules, including progesterone, felodipine, risperidone and paclitaxel, the authors investigated the impact of size and shape on the drug release kinetics.[50] Probing the drug release effects of the particle dimensions on the nanoscale, may be accomplished through the synthesis of block copolymer precursors with different block lengths, thereby creating micelles with independently tuned core/shell sizes.

To overcome the limitations that the CMC of micelles poses on intravenous-type drug carriers,[28-31] our research group and others have explored crosslinked micellar constructs, such as shell crosslinked knedel-like nanoparticles (SCKs), that combine the amphiphilic core-shell morphology of polymer micelles with stabilizing crosslinkers isolated throughout the peripheral shell layer. Due to the regioselective crosslinks in the peripheral shell region, these nanoscale assemblies can be diluted without disassembly, and have increased dimensional stability compared to their non-crosslinked micellar counterparts.[4,32-34] The core of the SCKs can retain its host capabilities, because the lack of crosslinks in the core region maintains chain mobility and access to the core volume, for sequestering of guests.[35-37] Moreover, just as in the case of macroscopic crosslinked networks originating from linear polymers,[51] the readily adjustable shell crosslinking density allows for gating of the transport of those guests into and out of the core domain, while retaining the structural integrity of the SCK nanostructures.[52] With the distinctively different dimensions, compositions and structures of the core and shell domains of SCKs, and an ability to modify each independently, probing the effects of each is of great interest.

In our recent work, we have investigated the effects of the chemical composition and thermal characteristics of the hydrophobic core polymer material for the loading and release of doxorubicin (DOX),[53] a widely used chemotherapy drug for first line treatment of metastatic breast cancer, as well as other therapeutic regimes. The two classes of SCKs used in our previous study were constructed from poly(acrylic acid)-based (PAA) amphiphilic diblock copolymers with either glassy amorphous polystyrene

(PS) block segment, possessing a high glass transition temperature (T_g), or semicrystalline poly(octadecyl acrylate-*co*-decyl acrylate) (P(ODA-*co*-DA)), possessing a low T_g and a crystalline melting temperature (T_m). The T_m of the P(ODA-*co*-DA) core domains could be tuned to be either below or above physiological temperature.[54] It was demonstrated that the SCKs containing core material with higher T_g and T_m values retained DOX to higher loading extents and resulted in slower release rates. However, the release profiles were similar, which suggested that the release behavior of these two classes of SCKs was governed predominantly by the core-shell morphology of these nanoparticles and was less dependent upon the core composition.[53] In this current study, we probed effects of the core and shell dimensions, independently, on the loading and release of small molecule guests. Effects of composition were held constant, by employing SCKs constructed from a single type of amphiphilic diblock copolymer, poly(acrylic acid)-*b*-polystyrene (PAA-*b*-PS), and using DOX as a model chemotherapeutic compound.

2.2. Materials and methods

2.2.1. Materials

All chemicals were purchased from Aldrich Chemical Co. (St. Louis, MO) and used without further purification unless otherwise noted. Slide-A-Lyzer dialysis cassettes (10 kDa molecular weight cut-off, MWCO) were purchased from Pierce Biotech. (Rockford, IL). Amicon® ultra centrifugal filter devices (30 kDa MWCO) were purchased from Millipore Corp. (Bedford, MA). The Supor 25 mm 0.1 μm

Spectra/Por Membrane tubes (MWCO 6-8 kDa), used for dialysis, were purchased from Spectrum Medical Industries Inc. Nanopure water (18 MΩ·cm) was acquired by means of a Milli-Q water filtration system, Millipore Corp. (Bedford, MA).

2.2.2. Instruments

^{1}H NMR and ^{13}C NMR spectra were collected on a Varian Mercury 300 spectrometer, using the residual solvent signal as internal standard. Infrared spectra were acquired on an IR Prestige 21 instrument from Shimadzu Corporation (Columbia, MD). UV-Vis spectra were collected at 37 °C in the region of 200 - 800 nm, using a Varian Cary 100 Bio UV-visible spectrophotometer. The molar extinction coefficient (ε) of doxorubicin ($\varepsilon = 13050\ M^{-1}cm^{-1}$ at 488 nm) was determined by a calibration curve in DMF/PBS, 4:1. The DOX concentrations in the nanoparticles were determined by UV-vis spectroscopy measured directly in the aqueous DOX-nanoparticle solution aliquots as a function of time.

Gel permeation chromatography was performed on a Waters Chromatography, Inc., 1515 isocratic HPLC pump equipped with an inline degasser, a model PD2020 dual-angle , light scattering detector (Precision Detectors, Inc.), a model 2414 differential refractometer (Waters, Inc.), and four PL$_{gel}$ polystyrene-*co*-divinylbenzene gel columns (Polymer Laboratories, Inc.) connected in series: 5 μm Guard (50 × 7.5 mm), 5 μm Mixed C (300 × 7.5 mm), 5 μm 10^4 (300 × 7.5 mm), and 5 μm 500 Å (300 × 7.5 mm) using the Breeze (version 3.30, Waters, Inc.) software. The instrument was operated at 35 °C with THF as eluent (flow rate set to 1.0 mL/min). Polymer solutions were prepared at a known concentration (*ca*. 3 mg/mL) and an injection volume of 200

μL was used. Data collection was performed with Precision Acquire 32 Acquisition program (Precision Detectors, Inc.) and analyses were carried out using Discovery32 software (Precision Detectors, Inc.) with a system calibration curve generated from plotting molecular weight as a function of retention time for a series of broad polydispersity poly(styrene) standards.

Glass transition temperatures (T_g) were measured by differential scanning calorimetry on a Mettler-Toledo DSC822® (Mettler-Toledo, Inc., Columbus, OH), with a heating rate of 10 °C/min. Measurements were analyzed using Mettler-Toledo Star^e v. 7.01 software. The T_g was taken as the midpoint of the inflection tangent, upon the third heating scan. Thermogravimetric analysis was performed under N_2 atmosphere using a Mettler-Toledo model TGA/SDTA851^e, with a heating rate of 5 °C/min. Measurements were analyzed using Mettler-Toledo Star^e v. 7.01 software.

Dynamic light scattering measurements were conducted with a Brookhaven Instruments, Co. (Holtsville, NY) DLS system equipped with a model BI-200SM goniometer, BI-9000AT digital correlator, and a model EMI-9865 photomultiplier, and a model Innova 300 Ar ion laser operated at 514.5 nm (Coherent Inc., Santa Clara, CA). Measurements were made at 25 ± 1 °C. Prior to analysis, solutions were filtered through a 0.45 μm Millex®-GV PVDF membrane filter (Millipore Corp., Medford, MA) to remove dust particles. Scattered light was collected at a fixed angle of 90 °. The digital correlator was operated with 522 ratio spaced channels, and initial delay of 5 μs, a final delay of 50 ms, and a duration of 8 minutes. A photomultiplier aperture of 400 μm was used, and the incident laser intensity was adjusted to obtain a photon counting of between, 200 and 300 kcps. The calculations of the particle size distributions and distribution averages were performed with the ISDA software package (Brookhaven Instruments Company), which employed single-exponential fitting, Cumulants analysis, and CONTIN particle size distribution analysis routines. All determinations were average values from ten measurements.

Transmission electron microscopy (TEM) bright-field imaging was conducted on a Hitachi H-7500 microscope, operating at 80 kV. The samples were prepared as follows: 4 μL of the dilute solution (with a polymer concentration of *ca.* 0.2 - 0.5 mg/mL) was deposited onto a carbon-coated copper grid, which was pre-treated with absolute ethanol to increase the surface hydrophilicity. After 5 min, the excess of the solution was quickly wicked away by a piece of filter paper. The samples were then negatively stained with 4 μL of 1 wt% phosphotungstic acid (PTA) aqueous solution. After 1 min, the excess PTA solution was quickly wicked away by a piece of filter paper and the samples were left to dry under ambient conditions overnight.

Small angle neutron scattering (SANS) experiments were performed on the 30m instrument (NG-3) at the NIST Center for Neutron Research (NCNR), National Institute of Standards and Technology (NIST). A series of fresh SCK samples was prepared in D_2O for the SANS studies. Each block copolymer as a powder (2 mg) was dissolved in DMF-d_7 (2 mL) and an equal amount of D_2O was added dropwise. Then the solution was dialyzed against D_2O for two days (which brought the volume up to *ca*. 8 mL). The micelle solutions were crosslinked with 2,2´-(ethylenedioxy)bis(ethylamine) (EDDA) crosslinker (dissolved in D_2O) and then the SCK nanoparticle solutions were dialyzed against D_2O. The final concentrations of the SCKs in D_2O were *ca*. 0.25 mg/mL. Samples were loaded in titanium sample cells with 30 mm diameter quartz windows at a 2 mm path distance. Monochromatic neutrons at $\lambda = 6$Å and a wavelength spread ($\Delta\lambda/\lambda$) of 0.14 were incident on the sample. The scattered neutrons were captured by a 64 cm × 64 cm 2D detector. Sample-to-detector distances were applied at 1.33, 4.50, and 13.17 m to cover a large scattering wavevector Q range ($0.004 < Q < 0.4$ Å^{-1}), defined by $Q = (4\pi/\lambda)\sin(\theta/2)$, where λ is the neutron wavelength and θ is the scattering angle. Sample data were corrected for background and empty cell scattering. The scattering length densities (Å^{-1}) used for PAA, PAA and EDDA, PS, and D_2O are 1.39e^{-6}, 5.82e^{-6}, 1.41e^{-6} and 6.31e^{-6}, respectively. Intensities were normalized to an absolute scale using main beam transmission measurements and were reduced according to published protocol.[55] The related densities were calculated to compare the differences between the corona of the four samples, and are unitless ratios.

2.2.3. Synthesis of block copolymers and preparation of nanoparticles

General procedure of preparation of poly(*tert*-butyl acrylate), P*t*BA, 2 - 3: A flame-dried 100-mL Schlenk flask equipped with a magnetic stir bar was charged with DDMAT (*S*-dodecyl-*S′*-(α,α′-dimethyl-α″-acetic acid) trithiocarbonate, **1**, 1 eq.), *t*-BA (70 - 200 eq.), azobisisobutyronitrile (AIBN) (0.05 eq.), and 2-butanone (10 - 20 mL). The flask was sealed with a rubber septum and allowed to stir for 10 min at room temperature to ensure homogeneous mixing. The reaction mixture was degassed by several freeze-pump-thaw cycles (> 3), after which the flask was allowed to return to room temperature and was allowed to stir for an additional 10 min. The flask was then immersed into a pre-heated oil bath at 60 °C to start the polymerization. The polymerization was monitored by analyzing aliquots collected at pre-determined times by ^{1}H-NMR spectroscopy. As the expected monomer conversion was reached, after *ca*. 3 - 6 h depending on desired block chain lengths, the polymerization was quenched by quick immersion of the reaction flask into liquid N_2 and opening to air. THF (20 mL) was added to the reaction flask and the polymer was purified by precipitation into 2 L of a methanol/ice mixture three times. The precipitants were collected and dried under vacuum overnight to afford **2** and **3** as a yellow powder. IR (KBr): 3000-2900, 1723, 1446, 1366, 1248, 1124, 843, 754 cm^{-1}. ^{1}H NMR ($CDCl_3$): δ 0.85 (t, J = 5 Hz, $C\boldsymbol{H}_3CH_2$-), 1.19 - 1.90 (br, -$CHC\boldsymbol{H}_2$- of the polymer backbone, alkyl chain of initiator, and $HOOCC(C\boldsymbol{H}_3)_2$-), 1.28 - 1.63 (br, $C\boldsymbol{H}_3C$), 2.17 - 2.41 (br, -$C\boldsymbol{H}CH_2$- of the polymer backbone), 3.22 - 3.36 (br, -$SCSC\boldsymbol{H}_2$-), 4.58 - 4.78 (br, -$CH_2C\boldsymbol{H}S$) ppm. ^{13}C NMR ($CDCl_3$): δ 28.1, 32.1 - 37.3, 40.1 - 42.6, 80.4 - 80.6, 172.3 - 174.1 ppm.

P*t*BA$_{52}$, 2: A total of 10.2 g (60% yield, 80% conversion) of the polymer was isolated. M_n^{NMR} = 7100 Da, $M_n^{GPC(RI)}$ = 7500 Da, PDI = 1.07, (T_g) = 50 °C, TGA in N_2: 230-245 °C, 40% mass loss; 245-450 °C, 55% mass loss.

P*t*BA$_{120}$, 3: A total of 12.6 g (70% yield, 67% conversion) of the polymer was isolated. M_n^{NMR} = 15700 Da, $M_n^{GPC(RI)}$ = 16700 Da, PDI = 1.04, (T_g) = 51 °C, TGA in N_2: 230-250 °C, 45% mass loss; 245-450 °C, 50% mass loss.

General procedure for preparation of poly(acrylic acid)-*b*-polystyrene (P*t*BA-*b*-PS) by chain extension of P*t*BA with styrene, **4** - **7**: To a flame-dried 50 mL Schlenk flask equipped with a magnetic stir bar, P*t*BA (1 eq.), styrene (200 - 400 eq. based on desired polymer chains), AIBN (0.05 eq.) and 1, 4-dioxane (5 - 10 mL) were added. The flask was sealed with a rubber septum and allowed to stir for 10 min. The reaction mixture was then degassed by several freeze-pump-thaw cycles (>3). After allowing the flask to return to room temperature, it was allowed to stir in a pre-heated oil bath at 60 °C to start the polymerization. The polymerization was monitored by analysis of aliquots taken at various times by ^{1}H NMR spectroscopy. The polymerization was quenched at *ca*. 10 - 70 h (depending on desired block chain lengths) by immersing the flask in liquid nitrogen and opening to air. The reaction mixture was dissolved in THF (5 mL) and precipitated into methanol/water (5:1) mixture twice to yield a fine yellow powdery product, **4** - **7**. The product was collected and dried under vacuum overnight. IR: 3100-2900, 1729, 1447, 1372, 1243, 1148, 849, 829, 760 cm^{-1}. ^{1}H NMR (CDCl$_3$): δ 0.83 (t, J = 5 Hz, C$\boldsymbol{H}_3$CH$_2$-), 1.20 - 1.80 (br, –CHC$\boldsymbol{H}_2$– of the polymer backbone, alkyl chain of initiator, and HOOCC(C$\boldsymbol{H}_3$)$_2$–), 1.30 - 1.61 (br, C$\boldsymbol{H}_3$C), 2.18 - 2.27 (br,–C$\boldsymbol{H}$CH$_2$– of the polymer backbone), 3.38 - 3.44 (br, –SCSC$\boldsymbol{H}_2$–), 5.22 - 5.68 (br, –CH$_2$C$\boldsymbol{H}$S), 6.65 - 7.21 (br, Ar–$\boldsymbol{H}$) ppm. ^{13}C NMR (CDCl$_3$): δ 28.2, 35.1 - 36.3, 39.5 - 41.6, 80.3, 127.9 - 128.9, 140.3, 170.2 - 173.4 ppm.

P*t*BA$_{52}$-*b*-PS$_{80}$, 4: M_n^{NMR} = 15,500 Da, $M_n^{GPC(RI)}$ = 14,300 Da, PDI = 1.2, $(T_g)_{PtBA}$ = 48 °C, $(T_g)_{PS}$ = 104 °C, TGA in N$_2$: 225-260 °C, 35% mass loss; 260-450 °C, 50% mass loss. 10% mass remaining above 450 °C. Compound **4** was prepared from **P*t*BA$_{52}$**, **2** (2.0 g, 0.3 mmol). The polymerization was carried out for 10 h before precipitation to afford the final product (0.50 g, 70% yield, 25% conversion).

P*t*BA$_{120}$-*b*-PS$_{100}$, 5: M$_n^{NMR}$ = 26,100 Da, M$_n^{GPC(RI)}$ = 22,500 Da, PDI = 1.1, $(T_g)_{PtBA}$ = 50 °C, $(T_g)_{PS}$ = 106 °C, TGA in N$_2$: 225-260 °C, 25% mass loss; 260-450 °C, 65% mass loss. 10% mass remaining above 450 °C. Compound **5** was prepared from **P*t*BA$_{120}$, 3** (1.01 g, 0.064 mmol). The polymerization was carried out for 18 h before precipitation to afford the final product (0.67 g, 80% yield, 50% conversion).

P*t*BA$_{52}$-*b*-PS$_{30}$, 6: M$_n^{NMR}$ = 10,200 Da, M$_n^{GPC(RI)}$ = 8,400 Da, PDI = 1.1, $(T_g)_{PtBA}$ = 48 °C, $(T_g)_{PS}$ = 105 °C, TGA in N$_2$: 230-255 °C, 30% mass loss; 255-450 °C, 60% mass loss. 10% mass remaining above 450 °C. Compound **6** was prepared from **P*t*BA$_{52}$, 2** (2.01 g, 0.13 mmol). The polymerization was carried out for 70 h before precipitation to afford the final product (2.5 g, 97% yield, 25% conversion).

P*t*BA$_{120}$-*b*-PS$_{40}$, 7: M$_n^{NMR}$ = 19,900 Da, M$_n^{GPC(RI)}$ = 17,200 Da, PDI = 1.2, $(T_g)_{PtBA}$ = 47 °C, $(T_g)_{PS}$ = 105 °C, TGA in N$_2$: 225-260 °C, 34% mass loss; 260-450 °C, 56% mass loss. 10% mass remaining above 450 °C. Compound **7** was prepared from **P*t*BA$_{120}$, 3** (2.5 g, 0.16 mmol). The polymerization was carried out for 15 h before precipitation to afford the final product (0.60 g, 85% yield, 10% conversion).

General procedure of preparation of PAA$_m$-*b*-PS$_n$, 8 - 11: A flame-dried 25 mL round bottom flask equipped with a magnetic stir bar was charged with P*t*BA-*b*-PS **5** (0.50 g - 1.50 g), and 15 mL of dichloromethane. Trifluoroacetic acid (TFA, 10 mL) was added to the stirring solution and the reaction was allowed to stir over night at room temperature, after which the solvent was removed under vacuum. The crude product was resuspended in 10 mL of THF and transferred to a pre-soaked dialysis tubing (MWCO *ca*. 6 - 8 kDa), and dialyzed against nanopure water for 4 days, to remove all of the impurities. The solution was then lyophilized to yield the resulting yellowish solid of PAA$_m$-*b*-PS$_n$, **8** - **11**. IR: 3700-2400, 1710, 1554, 1447, 1410, 1240, 1170, 1061, 1025, 798, 790 cm^{-1}. ^{1}H NMR (CDCl$_3$): δ 0.85 (t, J = 5 Hz, C***H***$_3$CH$_2$-), 1.36 - 2.46 (br,–CHC***H***$_2$– of the polymer backbone), 3.42 - 3.83 (br, –SCSC***H***$_2$–), 5.65 - 5.87 (br, –CH$_2$C***H***S), 6.65 - 7.21 (br, Ar–***H***) ppm, 11.3 - 13.8 (br, COO***H***). ^{13}C NMR (CDCl$_3$): δ 35.4 - 36.6, 42.5 - 45.6, 127.9 - 128.9, 140.1, 175.2 ppm.

PAA$_{52}$-*b*-PS$_{80}$, 8: M$_n^{NMR}$ = 12,500 Da, (T_g)$_{PAA}$ = 127 °C, (T_g)$_{PS}$ = 106 °C, TGA in N$_2$: 200-300 °C, 15% mass loss; 300-450 °C, 70% mass loss. 10% mass remaining above 450 °C. **8** was prepared from **P*t*BA$_{120}$-*b*-PS$_{100}$, 4** (0.63 g, 0.040 mmol). A total of 0.58 g of **8** was produced (85% yield).

PAA$_{120}$-*b*-PS$_{100}$, 9: M$_n^{NMR}$ = 19,500 Da, (T_g)$_{PAA}$ = 127 °C, (T_g)$_{PS}$ = 103 °C, TGA in N$_2$: 200-300 °C, 18% mass loss; 300-450 °C, 72% mass loss. **9** was prepared from **P*t*BA$_{120}$-*b*-PS$_{100}$, 5** (1.51 g, 0.048 mmol). A total of 1.07 g of **9** was produced (95% yield).

PAA$_{52}$-*b*-PS$_{30}$, 10: M$_n^{NMR}$ = 7,400 Da, (T_g)$_{PAA}$ = 130 °C, (T_g)$_{PS}$ = 101 °C, TGA in N$_2$: 200-290 °C, 17% mass loss; 290-450 °C, 74% mass loss. **10** was prepared from **P*t*BA$_{120}$-*b*-PS$_{100}$, 6** (1.49 g, 0.15 mmol). A total of 0.97 g of **10** was produced (89% yield).

PAA$_{120}$-*b*-PS$_{40}$, 11: M$_n^{NMR}$ = 13,200 Da, (T_g)$_{PAA}$ = 127 °C, (T_g)$_{PS}$ = 99 °C, TGA in N$_2$: 210-300 °C, 23% mass loss; 300-450 °C, 67% mass loss. **11** was prepared from **P*t*BA$_{120}$-*b*-PS$_{100}$, 7** (0.54 g, 0.025 mmol). A total of 0.44 g of **11** was produced (90% yield).

General procedure for micellization and crosslinking (50% crosslinked) of PAA-*b*-PS to form SCKs, 12 - 15: PAA-*b*-PS (*ca*. 50 mg) polymers were dissolved in DMF (50 mL) in a 250 mL round bottom flask and allowed to stir for 30 min at room temperature. To this solution, an equal volume of nanopure water was added dropwise *via* a syringe pump over a period of 3 h. The reaction mixture was allowed to stir for additional 24 h at room temperature and dialyzed against nanopure water for 4 days in a presoaked dialysis tubing (MWCO *ca*. 6 - 8 kDa) to afford a micelle solution with a final polymer concentration of *ca.* 0.25 mg/mL. To the micelle solution of PAA_m-*b*-PS_n was added a solution of EDDA in nanopure water (*ca*. 0.007 g/mL, 1.1 eq, nominal 50% crosslinking) dropwise *via* a syringe pump over a period of 2 h. To this solution, 1-[3´-(dimethylamino)propyl]-3-ethyl-carbodiimide methiodide (EDCI) in nanopure water (0.011 g/mL, 1.4 eq) was added dropwise *via* a syringe pump over 20 min and the resulting mixture was allowed to stir overnight before dialysis against nanopure water for 4 days in presoaked dialysis tubing (MWCO.*ca*. 6 - 8 kDa) to afford SCK solutions **12 – 15** with a final polymer concentration of *ca*. 0.25 mg/mL.

SCK of PAA_{52}-*b*-PS_{80}, 12: To a stock solution of PAA_{52}-*b*-PS_{80} aqueous micellar solution (~0.25 mg/mL, 30 mL) prepared from **8** (0.020 g, 1.6 μmol), was added a solution of EDDA in nanopure water (175 μL, 8.3 μmol, 1.1 eq., calculated based on 50% of number of poly(acrylic acid) units). The mixture was allowed to stir for 2 h at room temperature before a solution of EDCI in nanopure water (21 μL, 0.8 μmol, 1.4 eq.) was added. The reaction mixture was stirred for 24 h at room temperature and then transferred to a dialysis tube and dialyzed against nanopure water for 3 days. The resulting SCK solution had a concentration of 0.24 mg/mL.

SCK of PAA_{120}-*b*-PS_{100}, 13: To a stock solution of PAA_{120}-*b*-PS_{100} aqueous micellar solution (~0.25 mg/mL, 30 mL) prepared from **9** (0.02 g, 0.98 μmol), was added a solution of EDDA in nanopure water (256 μL, 0.01 mmol, 1.1 eq., calculated based on 50% of number of poly(acrylic acid) units). The mixture was allowed to stir for 2 h at room temperature before a solution of EDCI in nanopure water (14 μL, 0.5 μmol, 1.4 eq.) was added. The reaction mixture was stirred for 24 h at room temperature and then transferred to a dialysis tube and dialyzed against nanopure water for 3 days. The resulting SCK solution had a concentration of 0.24 mg/mL.

SCK of PAA_{52}-*b*-PS_{30}, 14: To a stock solution of PAA_{52}-*b*-PS_{30} aqueous micellar solution (~0.25 mg/mL, 30 mL) prepared from **10** (0.02 g, 2.6 μmol), was added a solution of EDDA in nanopure water (290 μL, 0.01 mmol, 1.1 eq., calculated based on 50% of number of poly(acrylic acid) units). The mixture was allowed to stir for 2 h at room temperature before a solution of EDCI in nanopure water (36 μL, 1.4 μmol, 1.4 eq.) was added. The reaction mixture was stirred for 24 h at room temperature and then transferred to a dialysis tube and dialyzed against nanopure water for 3 days. The resulting SCK solution had a concentration of 0.25 mg/mL.

SCK of PAA_{120}-*b*-PS_{40}, 15: To a stock solution of PAA_{120}-*b*-PS_{40} aqueous micellar solution (~0.25 mg/mL, 30 mL) prepared from **11** (0.02 mg, 1.5 μmol), was added a solution of EDDA in nanopure water (387 μL, 0.02 mmol, 1.1 eq., calculated based on 50% of number of poly(acrylic acid) units). The mixture was allowed to stir for 2 h at room temperature before a solution of EDCI in nanopure water (21 μL, 0.8 μmol, 1.4 eq.) was added. The reaction mixture was stirred for 24 h at room temperature and then transferred to a dialysis tube and dialyzed against nanopure water for 3 days. The resulting SCK solution had a concentration of 0.25 mg/mL.

2.2.4. DOX loading and release studies

General procedure for DOX loading experiments into PAA-*b*-PS SCK nanoparticles: To a vial containing a magnetic stir bar and SCK solution (10 mL, polymer concentration ~ 0.25 mg/mL), a solution of doxorubicin (2.273 mg/mL in DMF and 3 eq of triethylamine, 50 wt% with respect to the SCK) was added. The solution was shielded from light and stirred over night before being transferred to a centrifugal filter device (Amicon Ultra 4, 100 kDa MWCO, Millipore corp., Billerica MA, USA) and washed extensively with 5 mM pH 7.4 PBS at 37 °C to remove free DOX. The filtrate was analyzed by UV-Vis spectroscopy to confirm the removal of free DOX after several washing cycles. The DOX-nanoparticle solution was then reconstituted to a final volume of 5 mL with 5 mM pH 7.4 PBS buffer. The amount of incorporated DOX was determined by UV-Vis spectroscopy (488 nm, $\varepsilon = 13050\ M^{-1}cm^{-1}$ determined by a calibration curve in a 4:1 v/v mixture of DMF and DOX-SCK solution in PBS) .

DOX-SCK 16: Prepared from **12**. The final volume of the **DOX-SCK 16** was 9.99 mL with a DOX concentration of 0.054 mg/mL (22 wt%).

DOX-SCK 17: Prepared from **13**. The final volume of the **DOX-SCK 17** was 10.00 mL with a DOX concentration of 0.060 mg/mL (20 wt%).

DOX-SCK 18: Prepared from **14**. The final volume of the **DOX-SCK 18** was 10.01 mL with a DOX concentration of 0.043 mg/mL (16 wt%).

DOX-SCK 19: Prepared from **15**. The final volume of the **DOX-SCK 19** was 10.01 mL with a DOX concentration of 0.047 mg/mL (18 wt%).

General procedure for DOX release experiments: Each DOX-SCK solution was partitioned into two parts of 5 mL each and transferred to a presoaked dialysis cassette (Slide-A-Lyzer, 10 kDa MWCO, Pierce Biotechnology, Rockford IL). The cassette was allowed to stir in a beaker containing 4 L of 5 mM PBS at pH 7.4 and 37 °C for a period of 48 h. Another 5 mL of DOX-nanoparticle solution was also transferred to a presoaked dialysis cassette and allowed to stir in a beaker containing 4 L of 5 mM PBS at pH 5.0 and 37 °C for a period of 60 h. Samples (~1.5 mL) were removed from the cassette at 1, 2, 3, 4, 6, 9, 12, 18, 24, 30, 40, 50, and 60 h, and quickly analyzed by UV-Vis spectroscopy (488 nm) and injected back into the dialysis cassette.

2.3. Results and discussion

In our previous study, we investigated the effects of the core material within SCK nanoparticles (amorphous PS *vs.* semicrystalline P(DA-*co*-ODA)) on the loading and release of DOX. It was found that both of these two classes of SCKs were capable of sequestering sufficient amounts of DOX in the interior of the nanoparticle, due to the favorable ionic and hydrophobic interactions. For the PS core SCKs, a relatively higher loading capacity was observed, which could be attributed to π-π stacking interactions between the aromatic ring moieties of styrene and DOX molecules. In an effort to better understand the parameters governing the loading and release of guest molecules in SCK nanoparticles, we herein present a more comprehensive study on SCKs with retention of the core and shell compositions, PS and PAA, respectively, while varying the overall amphiphilic particle dimensions, including differentiation of the hydrophobic particle core size and hydrophilic, ionic shell thickness, independently.

The dimensions of block copolymer micelles are known to be controlled by the relative and overall volumes occupied by the hydrophilic and hydrophobic polymer chain segments, which are determined by their chain lengths and chemical compositions. A series of SCK nanoparticles was produced from covalent crosslinking of corresponding block copolymer micelles, and therefore, the dimensions of SCKs could be tuned by varying their block copolymer constituents. Block copolymers were designed to have predominantly hydrophilic or hydrophobic block segments, with sufficient structural differences, to provide measurable changes for the core diameter and/or shell thickness of the resulting nanostructures. These structural discrepancies could further affect the loading and release profiles for molecular cargo.

Four PAA-*b*-PS block copolymers having different relative block lengths and absolute chain lengths were synthesized *via* sequential reversible addition-fragmentation chain transfer (RAFT) polymerization reactions [56-65] of *t*-butyl acrylate (*t*BA) and styrene, followed by removal of the *t*-butyl ester protecting groups (Figure 2.1). Beginning from DDMAT, **1**, chain transfer agent, two P*t*BA macro-chain transfer agents (macro-CTAs), with number-averaged degrees of polymerization (DP_n) of 52 (**2**) and 120 (**3**) were prepared by RAFT polymerization of *t*BA. Chain extensions with styrene were then conducted to produce the P*t*BA-*b*-PS block copolymers with different DPs of styrene. In both polymerizations, AIBN was used as the initiator, and a relatively low reaction temperature (~ 60 - 70 °C) was employed to provide sufficient AIBN half-life for controlled polymerization. Complete removal of the *t*-butyl groups of P*t*BA-*b*-PS was achieved by TFA treatment and the structures of the resulting amphiphilic PAA-*b*-PS block copolymers were characterized by IR, ^{1}H NMR and ^{13}C NMR spectroscopies.

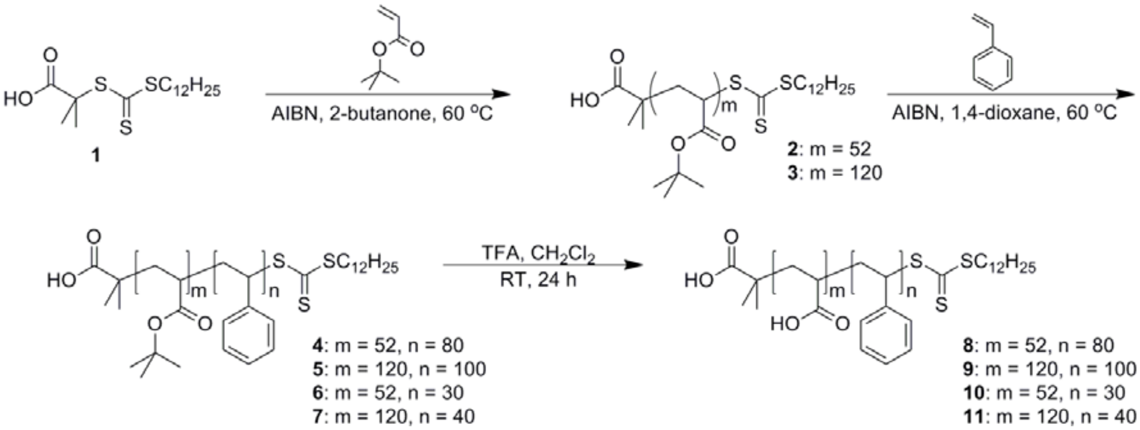

Figure 2.1. Preparation of P*t*BA macro-CTA, chain extension with styrene, and removal of the *tert*-butyl protecting groups to produce PAA$_m$-*b*-PS$_n$ polymers of various chain lengths.

The degrees of polymerization and well-defined structures for the polymers were confirmed by a combination of ^{1}H NMR spectroscopy and GPC. GPC analyses of the isolated polymers showed mono-modal molecular weight distributions with polydispersity indices (*PDI*) less than 1.3, indicating the controlled fashion during the polymerization process. Assuming full retention of the trithiocarbonate chain end, ^{1}H-NMR spectra of **2** and **3** allowed for determination of the degrees of polymerization of the *t*BA, by comparing the unique methyl terminus resonating at 0.83 ppm with the broad backbone proton signals from 1.2 to 2.4 ppm, which were in agreement with the GPC data. Maintenance of the trithiocarbonate chain end was further observed during growth of the P*t*BA-*b*-PS block copolymers. In addition, the number average molecular weights determined by GPC for P*t*BA-*b*-PS were in agreement with those calculated by ^{1}H NMR spectroscopy (the PAA-*b*-PS adsorbs onto the column packing material and, therefore, cannot be analyzed directly by GPC). The degrees of polymerization and the number average molecular weights of the P*t*BA-*b*-PS and PAA-*b*-PS block copolymers were calculated based on ^{1}H NMR spectroscopy, by comparing the backbone proton signals to those of the aromatic rings at 6.6 - 7.2 ppm.

The significant differences in composition between the PS and PAA segments were revealed by the thermal properties of these block polymers. Each PAA-*b*-PS block copolymer exhibited two glass transition temperatures, at *ca*. 100 and 127 °C, due to phase segregation of the two block segments in the bulk state. This amphiphilic, phase segregating property was relied upon for self assembly of the block copolymers into discrete nanoscale objects in solution.

The micelles and corresponding SCK nanoparticles were prepared from these four PAA_m-*b*-PS_n amphiphilic block copolymers, by following the conventional aqueous micellization methodology (Figure 2.2). Water (a selective solvent for the PAA block segment) was introduced to the DMF (a good solvent for both PAA and PS) solutions of block copolymers to form discrete spherical micelles. The PAA shell regions of these micelles were then crosslinked *via* amidation chemistry with 2,2´-(ethylenedioxy)bis(ethylamine) (EDDA), as a diamine crosslinker, in the presence of 1-[3´-(dimethylamino)propyl]-3-ethyl-carbodiimide methiodide (EDCI) to afford SCK nanoparticles (Figure 2.2). Under the protection of the crosslinked shell layer, the core domain is capable of serving as a nanoscopic host to encapsulate guest molecules. It was expected that the composition of both the core and shell domains could exert influence on the overall characteristics of the SCK nanoparticles, such as the size, shape, flexibility, loading capacity, and release kinetics and/or extents.

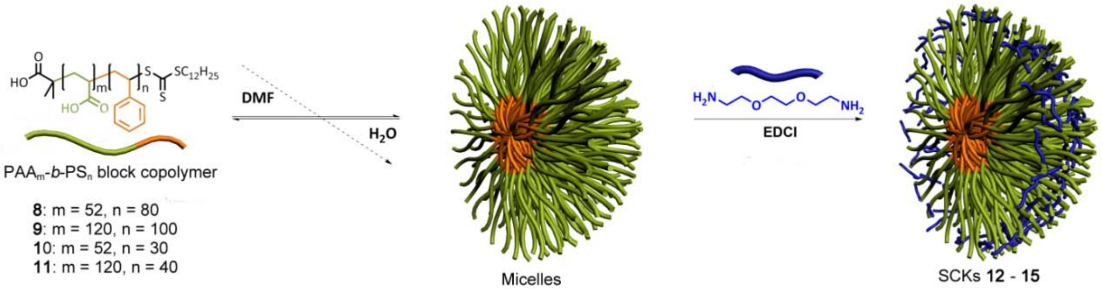

Figure 2.2. Schematic representation of the supramolecular assembly of PAA$_m$-*b*-PS$_n$ block copolymers into micelles and their subsequent crosslinking with EDDA to form SCKs.

The dimensions of the SCKs (**12-15**), were characterized by TEM (Figure 2.3) and DLS (Figure 2.4). The circularly-shaped images observed by TEM suggested that these nanoparticles were spherical with narrow size distributions. The SCKs prepared from the block copolymer precursors with higher PS block length (*i.e.*, DP$_{PS}$ = 80 and 100) formed particles with larger core sizes and aggregation numbers (Table 2.1). The size effect from larger PAA blocks was not distinguished by TEM, due to the difficulty in measuring accurately the entire particle diameter by the staining methods used in this study. However, the effect of the PAA degree of polymerization on the SCK shell thickness was confirmed by DLS measurements (Figure 2.4). As the DP$_n$ value of the PAA segments was increased from 52 (**12**) to 120 (**13**), *ca.* 25% increase of the hydrodynamic diameter of the resulting SCKs was observed, with no perceptible variation of the core domain size. For **14** and **15**, a similar trend was also observed. Based upon these data, the volumes occupied by the PS cores and PAA shells, the thicknesses of the PAA shells, and the core-shell interfacial areas were calculated (Table 2.1). The ratios of the volumes occupied by the PAA shells to those of the PS cores increased from SCK **12-15**, and they correlated directly with the proportions of acrylic acid-to-styrene block lengths for each of the block copolymer precursors. The core-shell interfacial areas per particle for **12** and **13** were larger than for **14** and **15**, but the core-shell interfacial areas for the total number of particles for all samples were approximately equivalent, since there were fewer total particles present in samples **12** and **13**.

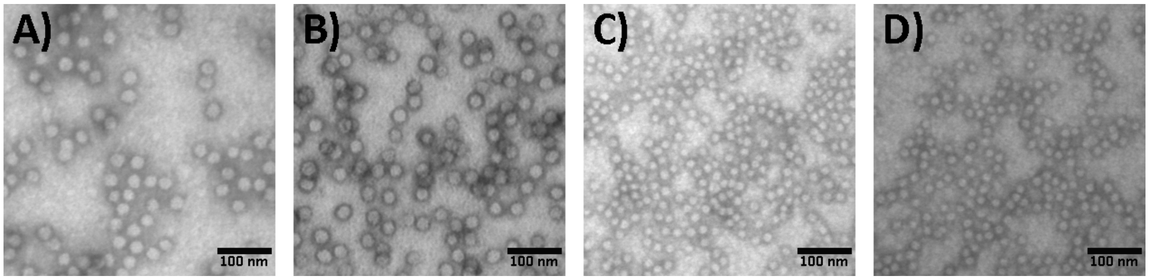

Figure 2.3. Characterization of SCKs **12 - 15** by TEM (drop deposited on carbon-coated copper grids and stained negatively with phosphotungstic acid) of A) **12**, B) **13**, C) **14**, and D) **15**.

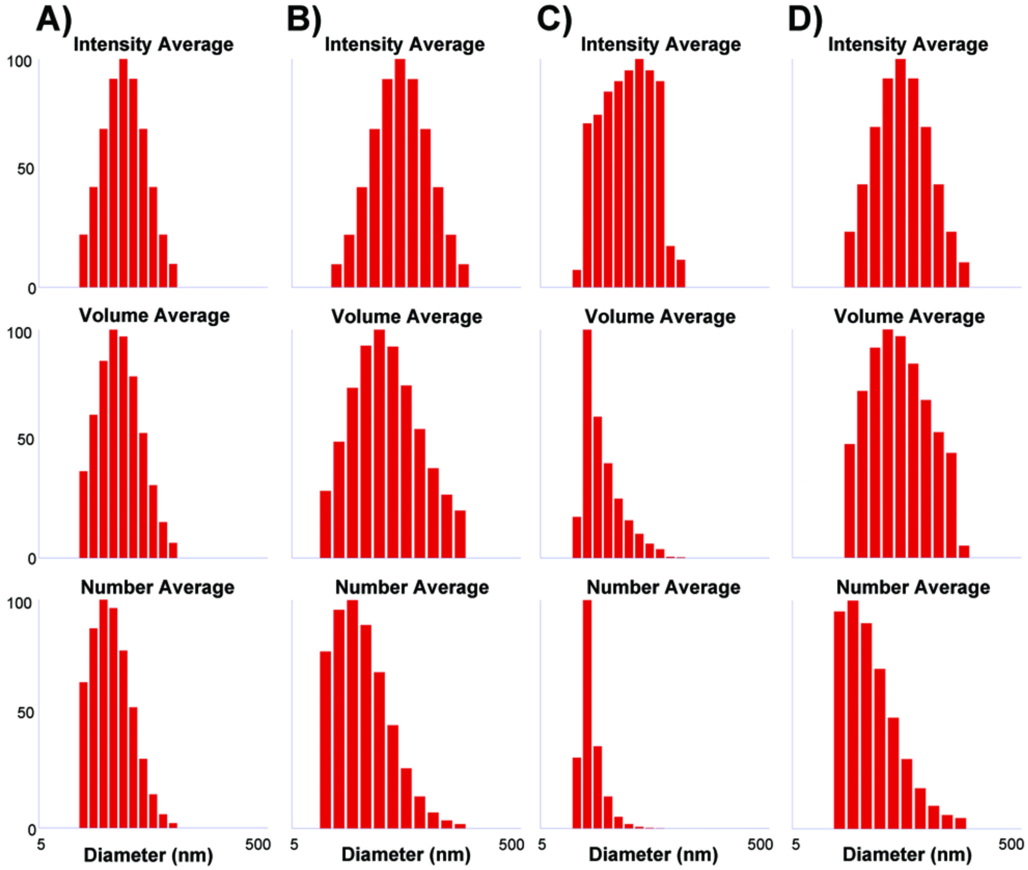

Figure 2.4. Characterization of SCKs **12 - 15** by DLS. DLS histograms of intensity-averaged, volume-averaged, number-averaged hydrodynamic diameters : A) SCK **12**, B) SCK **13**, C) SCK **14**, and D) SCK **15** in nanopure water.

SANS data of the SCKs in D2O solutions were fitted by a smeared polydispersity core-shell sphere (SPCSS) model (Figure 2.5). The SPCSS model, which involves a variety of core sizes due to polydispersity and smearing effects, gives the best fitting results. An example of different fitting model comparison for SCK 12 is shown in Figure 2.5B. For 13 and 14, scattering intensity increased in the low-Q region, indicating possible aggregation of micelles. However, all of the samples fit well by the SPCSS model to give the results of core sizes and shell thicknesses listed in Table 2.1. The overall particle dimensions from SANS were similar to the number-average hydrodynamic diameters as determined from DLS. However, the core sizes from SANS fitting were slightly smaller than the particle core diameters observed by TEM, which may be caused by slight distortion of the spherical particles upon adsorption onto the TEM grid. The added EDDA, which went into the corona through condensation with PAA, increased the scattering length density of the corona (from 1.39e-6 to 5.82e-6 Å-2). Assuming the hydrophobic polystyrene formed a homogeneously-dense core in aqueous solution, the densities of the corona for the four SCK nanoparticles were found to be inversely proportional to the corresponding lengths of the PAA block of the polymer precursors and it was observed that samples with longer PAA block segments had lower coronal densities.

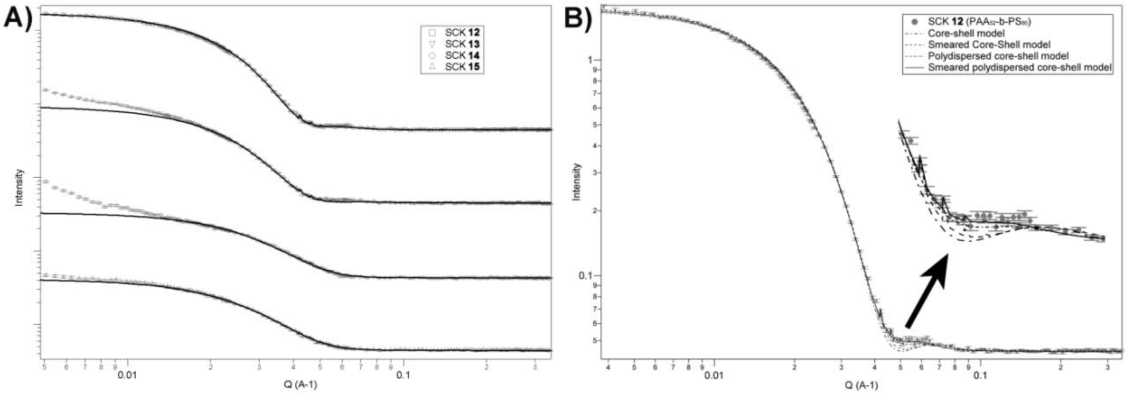

Figure 2.5. A). Small angle neutron scattering (SANS) data of SCK **12** - **15**. Black solid lines present fitting curves of “smeared polydispersed core-shell sphere” model. B). Model fitting results for SANS profile of SCK **12** with "core-shell sphere" model, "smeared core-shell sphere" model, "polydispersed core-shell sphere" model and "smeared polydispersed core-shell sphere" model.

Table 2.1. Experimental and calculated dimensions of the SCKs, and quantified DOX loading values.

SCK	**12**	**13**	**14**	**15**
Polymer precursors	PAA_{52}-*b*-PS_{80}	PAA_{120}-*b*-PS_{100}	PAA_{52}-*b*-PS_{30}	PAA_{120}-*b*-PS_{40}
D_{TEM} [nm]	19 ± 2	20 ± 2	11 ± 2	13 ± 2
V_{PS} [nm^3]	3600	4200	700	1200
Aggregation number	270	260	140	180
V_{PAA} [nm^3]	1600	3600	830	2500
$T_{shell, calc}$ [nm]	1.5	2.3	1.5	3.1
V_{PAA}/V_{PS}	**0.44**	**0.86**	**1.2**	**2.1**
$(D_h)_{Int}$ [nm]	88 ± 6	110 ± 16	81 ± 12	90 ± 12
$(D_h)_{Vol}$ [nm]	30 ± 3	43 ± 6	20 ± 6	35 ± 2
$(D_h)_{Num}$ [nm]	24 ± 2	30 ± 3	14 ± 3	18 ± 3
$SA_{core/particle}$ [nm^2]	1100	1300	380	530
Total # particles [x10^{14}, 10 mL solution volume]	4.4	3.0	14	6.1
$SA_{core/total}$ [x10^{17} nm^2, 10 mL solution volume]	5	4	5	3
$D_{core,SANS}$ [nm]	17.4	15.3	9.0	8.9
Core size polydispersity	0.13	0.11	0.20	0.33
D_{SANS} [nm]	24.4	25.1	17.4	17.3
$T_{shell, SANS}$ [nm]	3.5	4.9	4.7	4.2
Related density of shell	4.6	3.0	4.5	2.7
DOX per particle	1400	2200	340	860
DOX/V_{PAA}	**4.0**	**2.7**	**1.8**	**1.5**

Table 2.1. Continued

D_{TEM} = diameter by TEM

V_{ps} = volume of the PS core

Aggregation number calculated based on diameter by TEM using previously reported equation

V_{PAA} = volume of the PAA shell, calculated from the TEM core volume to obtain the block copolymer aggregation number, convert to the PAA mass from the total number of AA repeat units, and finally the volume occupied by PAA was determined using a PAA density of 1.05 g/mL

$T_{shell, calc}$ = thickness of the PAA shell in the solid state, estimated from the volume of PAA + volume of PS minus the radius of the PS core

D_h = intensity (Int), volume (Vol), number (Num) average diameters by DLS

$SA_{core/particle}$ = core-shell interfacial area per particle

$SA_{core/total}$ = core-shell interfacial area for total numbers of particles in 10 mL of aqueous solution

$D_{core,SANS}$ = core diameter from SANS

D_{SANS} = particle size from SANS

$T_{shell, SANS}$ = shell thickness from SANS

The encapsulation of DOX into SCK nanoparticles was carried out by incubating DOX solutions in DMF with SCKs in aqueous solutions (Figure 2.6). The organic solvent was used to swell the polystyrene core of the SCKs and provide sufficient DOX concentration to drive the diffusion-controlled loading/encapsulation process. This procedure for loading of DOX into pre-established SCKs was followed so that the dimensions of the SCKs could be accurately controlled and locked-in by the shell crosslinks, without potential complications that can occur for block copolymer assembly in the presence of additives. In addition, if the DOX had been present during the crosslinking reaction employed, carbodiimide-mediated amidation, side reactions between the amine functionality of DOX and the AA residues throughout the micellar shell domain could have occurred, covalently linking the drug to the nanostructure. After 24 h of incubation, the unincorporated DOX molecules were removed from the DOX-SCK system by centrifugation and extensive washing using a centrifugal-filtration membrane and 5 mM PBS (with 5 mM NaCl) at 37 °C. After the centrifugation filtration-based washing procedure, each SCK solution was reconstituted to its original concentration by the addition of PBS. The resulting DOX concentrations in the SCKs were calculated from the absorption of DOX at 488 nm. A *ca* 20 wt% loading capacity, relative to the mass of PAA-*b*-PS block copolymer precursors and independent of the SCK composition, was achieved for each SCK. This result indicated that the core size of the SCKs did not affect the overall loading capacity for the entire series of nanoparticle solutions. In fact, even for **14**, with the smallest core volume (700 nm^3), the encapsulated DOX could reach a concentration of ~ 75 µM, which was almost 400 times the SCK nanoparticle concentration. However, on a per particle basis, the larger PS cores gave higher numbers of the DOX molecules per particle. It is well-known that the micellar hydrophobic core domain can sequester DOX through hydrophobic and π-π stacking interactions. Meanwhile, other factors, such as electrostatic interactions and hydrogen bonding between DOX and the functionalities across the micellar shell domain, must also be taken into account for the overall loading capacity of the nanoscale vehicles.[31,66] Because the ratio of the number of DOX molecules loaded per particle to the volume of PAA per particle decreased as the volume of PAA per particle relative to volume of PS increased (Table 2.1), we hypothesize that the DOX preferentially resided at the core-shell interface and/or in the core domain. If the DOX molecules were localized in the shell layer, then these trends would have been increasing in parallel. The PAA shell layer was critical, however, to the diffusion of the DOX, as revealed by release kinetics studies.

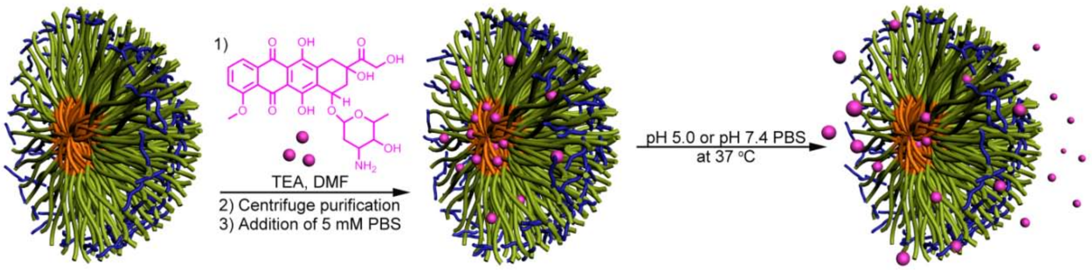

Figure 2.6. Schematic representation of the loading of DOX into the core, core-shell interface and shell region of the SCKs while suspended in aqueous solution, and release of DOX from the SCK in pH 5.0 or pH 7.4 buffer at 37 °C.

The DOX release profiles from the SCK nanoparticles were studied by monitoring the decrease in DOX concentration over time, in dialysis cassettes.[67] Based upon the chemical characteristics of DOX and PAA and similarities with literature studies,[66] we hypothesized that the release of DOX from the SCK nanoparticles would be faster and proceed to a greater extent at more acidic pH conditions, compared with the release rate at physiological pH 7.4. Promoted release was considered due to loss of electrostatic interactions between the amine functionality of DOX (pK_a of 8.25)[68] and the PAA shell regions of the nanoparticles upon protonation of acrylic acid groups at lower pH (pK_a of *ca*. 5).[66] At pH 7.4, DOX carries a positive charge that can form electrostatic interactions with the negatively-charged deprotonated PAA residues in the shell region of the nanoparticles, whereas at pH 5.0, a majority of the acrylic acid residues would be protonated and the loss of electrostatic interactions would trigger release of DOX. This hypothesis was supported by all four SCK nanoparticles, which exhibited *ca*. 40% release at pH 7.4 and 60% at pH 5.0 over 60 h (Figure 2.7). In addition, the final extents of release of DOX from the SCKs with smaller cores (**14** and

15) were lower compared with the SCKs with larger cores (**12** and **13**). These differences could be attributed to more frequent inter-particle exchange of the DOX molecules, enhanced by the higher numbers of **14** and **15** nanoparticles (2-3-fold increase, compared to **12** and **13**, respectively, Table 2.1). More importantly, however, is the ratios of the volume of PAA to the volume of PS, which increase from SCK **12-15**, in agreement with the relative extents of release, due to the need for the DOX to diffuse through and escape from the PAA shell to be observed as released from the dialysis cassette.

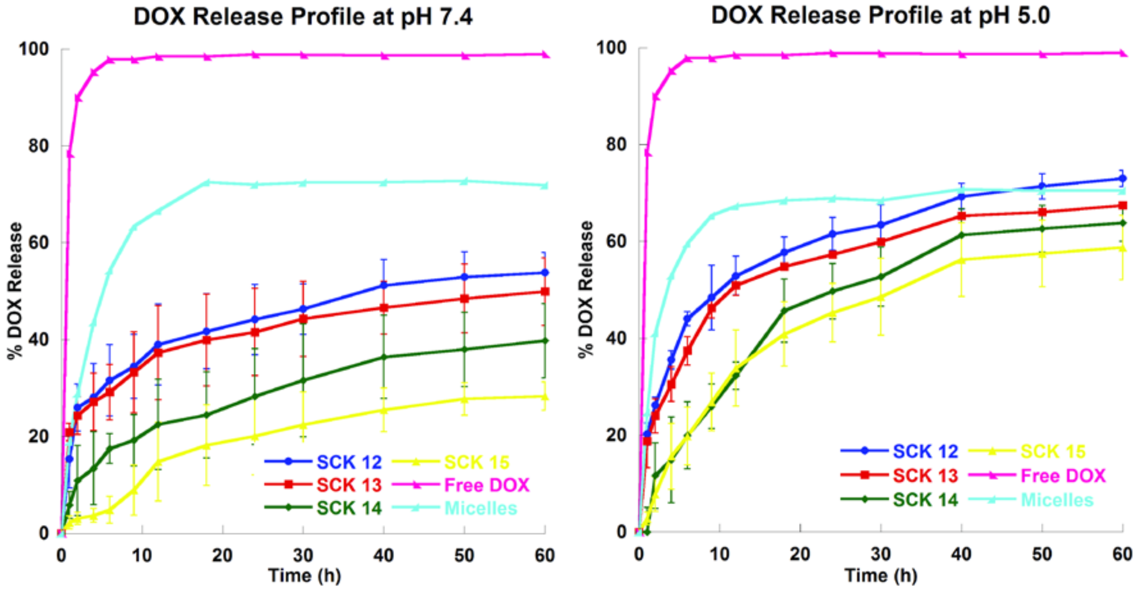

Figure 2.7. DOX release profiles of free DOX, micelles, and SCK**12**, SCK**13**, SCK**14** and SCK**15** at pH 7.4 or pH 5.0.

For a quantitative determination of the kinetics of DOX release, the experimental data were fit to an exponential relation for Fickian diffusion of a drug from spherical polymeric devices, the Higuchi equation:[69-71]

$$\frac{M_t}{M_\infty} = kt^{\frac{1}{2}}$$

where M_t/M_∞ is the proportion of drug released at a given time, k is the rate constant of drug release, and t is time. The proportion of DOX release plotted against the square root of release time was approximately linear for the first 50% of drug release (Figure 2.8), in agreement with the limitations of the Higuchi model. The rate constants, k, calculated from the Higuchi plots, indicated faster release kinetics for the first 50% of drug release at pH 5.0 compared with pH 7.4, for all four SCKs **12** - **15** (Table 2.2). Faster release at pH 5 indicates that the rate determining step for release involves exit through the shell and not from the core, suggesting that a portion of the DOX resides in the shell and/or at the core-shell interface, in addition to potentially being within the core of the particles.

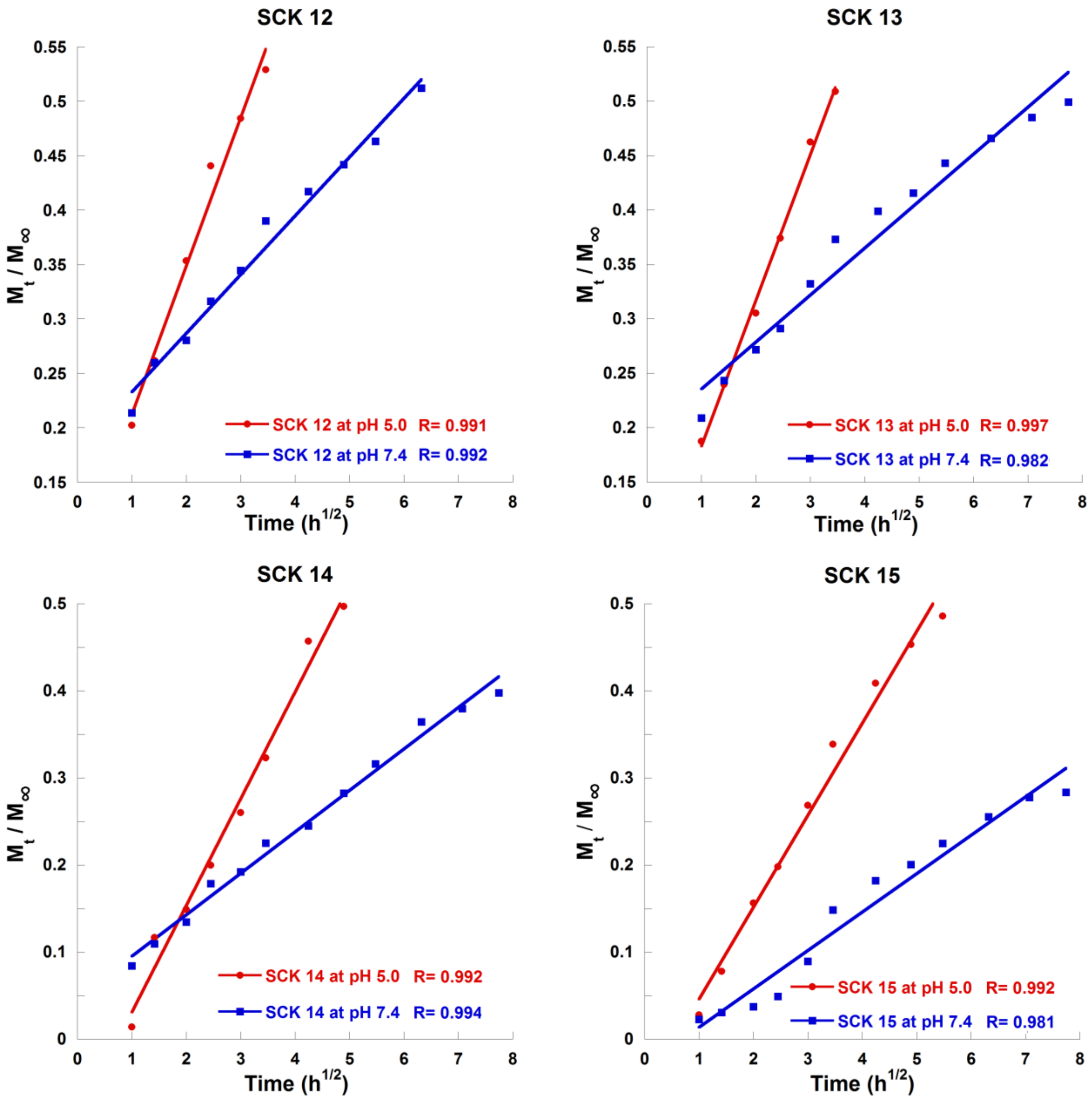

Figure 2.8. Higuchi plots of DOX release profiles of SCK**12**, SCK**13**, SCK**14** and SCK**15** at pH 7.4 or pH 5.0.

Table 2.2. DOX release rate, *k* ($h^{-½}$), obtained from fitting drug release experimental data to the Higuchi model.

		12	**13**	**14**	**15**	**Micelles**
		From Polymer Precursors				
		PAA_{52}-*b*-PS_{80}	PAA_{120}-*b*-PS_{100}	PAA_{52}-*b*-PS_{30}	PAA_{120}-*b*-PS_{40}	PAA_{120}-*b*-PS_{40}
pH 7.4	$k, h^{-½}$	0.0540	0.0431	0.0477	0.0441	0.245
pH 5.0	$k, h^{-½}$	0.136	0.134	0.124	0.106	0.278

As control experiments, we studied the release of free DOX from the dialysis cassette, which reached a complete release within 5 h, confirming that the measurements were not complicated by the dialysis cassette. We also found that a complete release of DOX was reached within 30 h from the polymer micelles, with a final extent of release of *ca*. 70% at both pH values (Figure 2.7 and Table 2.2). The faster release of DOX from the micelles (k = 0.245 or 0.278 $h^{-½}$ at pH 7.4 or pH 5.0, respectively) compared to the SCKs (k ranges from 0.0431 to 0.136 $h^{-½}$) suggests that crosslinking affects the release, which may be due to a combination of differences in compositions and polymer chain dynamics with the incorporation of crosslinkers.

To further quantitatively understand the differences and similarities in DOX release profiles, model-independent methods, which allow us to calculate f_1, the difference factor, and f_2, the similarity factor, were used:[72,73]

$$f_1 = \frac{\sum_{t=1}^{n} |R_t - T_t|}{\sum_{t}^{n} R_t} \times 100$$

where t is the sampling time, n is the number of samples, R_t is the dissolution value of the reference (measured as the percentage of DOX release for the reference) and T_t is the dissolution value of the sample of interest (measured as the percentage of DOX release from the sample). When the reference profile and the sample profile are identical, f_1 is equal to zero and, generally, the profiles are considered similar with f_1 values up to 15. The f_2 factor is a logarithmic transformation of the sum of squared error of difference between the reference and the sample of interest.

$$f_2 = 50 \times \log\left\{\left[1 + \frac{1}{n}\sum_{t=1}^{n}(R_t - T_t)^2\right]^{-0.5}\right\} \times 100$$

When the reference profile and the sample profile are identical, f_2 is equal to 100 and, generally, the profiles are considered similar when f_2 values are greater than 50. Both the difference factor f_1 and the similarity factor f_2 revealed that the SCK release profiles were significantly different from the free DOX and micelle release profiles (where all f_1 factors are greater than 15 and all f_2 factors are less than 50). There were similarities between SCK**12** and SCK**13** release profiles (f_1 factors ~ 7 and f_2 factors ~ 70), and SCK**14** and SCK**15** release profiles (f_1 factors ~ 11 and f_2 factors ~ 60). In addition, there are mathematical differences between the release profiles of SCKs with larger cores (SCK**12** and SCK**13**) *vs*. SCKs with smaller cores (SCK**14** and SCK**15**). Moreover, the greatest difference observed for **12** (fastest release) *vs*. **15** (slowest release) is in agreement with the observation that the ratio of the volume occupied by the PAA shell *vs*. that of the PS core is least for **12** and greatest for **15** (Table 2.3 – Table 2.6).

Table 2.3. Difference factor (f_1) values of SCK**12**-SCK**15** against free DOX or against micelles as the references.

Reference:	Free DOX			
Sample	SCK**12**	SCK**13**	SCK**14**	SCK**15**
pH 5.0	46	50	61	65
pH 7.4	60	62	75	84
Reference:	Micelles			
Sample	SCK**12**	SCK**12**	SCK**12**	SCK**12**
pH 5.0	16	16	16	16
pH 7.4	35	35	35	35

Table 2.4. Difference factor (f_1) values of SCK**12**-SCK**15** against each other as references.

Reference:	SCK**12**			SCK**13**		
Sample	SCK**13**	SCK**14**	SCK**15**	SCK**12**	SCK**14**	SCK**15**
pH 5.0	7	28	36	8	23	31
pH 7.4	8	39	60	8	35	57
Reference:	SCK**14**			SCK**15**		
Sample	SCK**12**	SCK**13**	SCK**15**	SCK**12**	SCK**13**	SCK**14**
pH 5.0	39	29	11	57	45	13
pH 7.4	64	54	34	150	134	52

Table 2.5. Similarity factor (f_2) values of SCK**12**-SCK**15** against free DOX or against micelles as the references.

Reference:	Free DOX			
Sample	SCK**12**	SCK**13**	SCK**14**	SCK**15**
pH 5.0	-8	-10	-14	-16
pH 7.4	-14	-15	-19	-21
Reference:	**Micelles**			
Sample	SCK**12**	SCK**12**	SCK**12**	SCK**12**
pH 5.0	27	19	5	2
pH 7.4	8	6	-4	-8

Table 2.6. Similarity factor (f_2) values of SCK**12**-SCK**15** against each other as references.

Reference:	SCK**12**			SCK**13**		
Sample	SCK**13**	SCK**14**	SCK**15**	SCK**12**	SCK**14**	SCK**15**
pH 5.0	70	41	36	70	46	41
pH 7.4	75	42	32	75	45	35
Reference:	SCK**14**			SCK**15**		
Sample	SCK**12**	SCK**13**	SCK**15**	SCK**12**	SCK**13**	SCK**14**
pH 5.0	41	46	67	37	41	67
pH 7.4	42	45	54	32	35	54

2.4. Conclusions

In this study, SCK nanoparticles were designed to have various relative and absolute core and shell dimensions to mediate the packaging and release of DOX as a model chemotherapeutic system. Variation over the nanoparticle dimensions was achieved through controlling of the block copolymer precursor chain lengths, to afford a series of well-defined and rigorously characterized nanoscopic vessels for drug molecule loading and release studies. The amphiphilic core-shell morphology of the SCK nanostructures provided opportunities for tuning of the drug loading capacities and rates of release; increasing core diameters and core-shell interfacial surface areas were important for increased guest packaging capacity and decreasing proportions of shell-to-core volume was the critical parameter for increased kinetics of release. The electrostatic complexation of DOX and the PAA shell showed predominant effects on the rates of release, giving accelerated release at acidic pH *vs.* under physiological pH conditions, which may lead to enhanced selectivity of delivery in cancer therapy. Moreover, the amphiphilic core-shell morphology of the SCKs provided opportunities for tuning of the relative contributions of hydrophobic and/or π-π interactions with the core domain and electrostatic interactions with the shell layer to give significant impact on the extents of release of DOX. The variety of contributing factors, of chemical composition, dimensions of the core and shell domains, and total particle concentrations, made direct determination of the effects of each parameter complicated, although the greatest correlation appeared to be the ratio of the volume of the shell *vs*. the volume of the core. As the relative proportion of PAA shell to PS core volumes decreased, the rate and extent of release increased. Because these proportions are conveniently tuned by the nature of the block copolymer precursor, SCK nanoparticles offer enormous opportunity for the production of nanoscopic drug carriers with finely-tuned performance potential. These studies, therefore, point to future directions to craft sophisticated devices for controlled drug release.

2.5. Acknowledgments

Financial support from Covidien is gratefully acknowledged. K. L. Wooley serves as a consultant to Covidien. This work was also supported in part by the National Heart Lung and Blood Institute of the National Institutes of Health as a Program of Excellence in Nanotechnology (HHSN268201000046C), by the National Science Foundation (DMR-0906815 and DMR-1032267), and by the Welch Foundation through the W. T. Doherty-Welch Chair in Chemistry, Grant No. A-0001. Assistant Professor fellowship from the Knut and Alice Wallenberg Foundation (to A. M. N), as well as financial support from Åke Wibergs foundation, Karolinska Insitutet, The Swedish Medical Nanoscience Center and from the Swedish Research Council 2009-3259, are also gratefully acknowledged. The authors thank Department of Otolaryngology, Washington University School of Medicine for the access to TEM facility and Center for Neutron Research at National Institute of Standards and Technology for the access to SANS facility.

CHAPTER III

PACLITAXEL-LOADED SCK NANOPARTICLES: AN INVESTIGATION OF LOADING CAPACITY AND CELL KILLING ABILITIES *IN VITRO*

3.1. Introduction

Paclitaxel (PTX) is a chemotherapeutic agent that has been used to treat a variety of cancers including, primary epithelial ovarian, colon, non-small cell lung and metastatic breast cancers. Its mechanism of action is through stabilization of microtubules which promotes polymerization of tubulin, causing cell death by disrupting the dynamics necessary for cell division.[74] Due to its high hydrophobicity and poor solubility in aqueous solutions, PTX is normally formulated with high percentages of additives such as Cremophor® EL (polyethoxylated castor oil), which can cause high incidences of adverse effects including hypersensitivity reactions,[75] neurotoxicity, nyelosuppression and allergic reactions. To avoid the toxicities associated with Cremophor® EL, a biologically interactive, nanometer-sized albumin-bound PTX particle (Abraxane®) has been developed (hydrodynamic diameter of *ca*. 110 nm), which uses the unique properties of albumin, a natural carrier of lipophilic molecules in humans.[76] PEO groups have been serving as the synthetic analogue to impart stealthiness *in vivo* and have been used in conjunction with hydrophobic blocks such as poly(D,L-lactic acid),[77] oligo(cholic acid),[78,79] poly(ε-caprolactone),[80,81] polycarbonates bearing pH-[82,83] or thermally-responsive[84] pendant groups or crosslinkable polyaspartamide groups. For example, NK105 micellar formulation, constructed from block copolymers of polyethylene oxide (PEO) and polyaspartate, can physically encapsulate up to 23 wt% of PTX, and is currently being investigated in phase II clinical trials.[85,86] Micelle constructed from diblock copolymers of polyethylene glycol and poly(D,L-lactic acid) for delivery of PTX is approved in Korea (Genexol®-PM) for cancer treatment and is in phase IV clinical trials in the USA as a safer alternative to Cremophor® EL and ethanol in Taxol.[77,87,88] Combinatorial delivery of PTX and siRNA has also been reported by utilizing cationic micelles self assembled from triblock copolymer poly(dimethylaminoethyl methacrylate)-*b*-poly(ε-caprolactone)-*b*-poly(dimethylaminoethyl methacrylate), which undergoes co-assembly and complexation processes with the payloads (6.8 wt% drug, hydrodynamic diameters ranging from 60 to 130 nm and zeta potential ranging from +30 to +36 mV).[89] Chemical modifications of the PTX molecule have also been achieved to covalently link the drug molecule onto the nanostructure vehicle.[18,89]

Amphiphilic block copolymer micelle structures, which mimic biological entities, have been investigated for drug delivery applications that take advantage of their core-shell morphology and tunable surface chemistry.[5,18,90] Our group and others have explored crosslinked micellar constructs, such as shell crosslinked knedel-like nanoparticles (SCKs) that combine the amphiphilic core-shell morphology of polymer micelles with stabilizing and release mediating crosslinkers isolated throughout the peripheral shell layer.[39,91] Towards the goal of an enhanced safety profile and increased efficacy, in this current study, paclitaxel has been encapsulated in amphiphilic, SCK nanoparticles (PTX-SCKs) as a novel drug delivery system. Paclitaxel-loaded SCK nanoparticles were synthesized from an amphiphilic diblock copolymer, poly (acrylic acid)-*b*-polystyrene (PAA-*b*-PS), in which PTX was encapsulated into the SCK nanoparticles through a co-assembly process at various concentration formulations. The *in vitro* cell killing ability was investigated on two different sizes of PTX-loaded SCKs, having core diameters of 20 ± 3 nm or 60 ± 5 nm and overall hydrodynamic diameters of 50 ± 15 nm or 120 ± 30 nm, respectively. Furthermore, the effects of PEGylation were evaluated for the smaller SCK samples. A dual purpose small molecule, pyrazine-based dye, served both as the crosslinker and fluorescent tag for visualization of cell internalization in KB cells by confocal fluorescence microscopy. Separation assays with high molecular weight cut-off filters confirmed that the paclitaxel was loaded within the nanoparticles and not free in solution.

3.2. Materials and methods

3.2.1. Materials

All chemicals were purchased from Aldrich Chemical Co. (St. Louis, MO) and used without further purification unless otherwise noted. Paclitaxel (PTX) was purchased from Cedarburg Hauser (Denver, CO). The Supor 25 mm 0.1 μm Spectra/Por Membrane tubes (MWCO 6-8 kDa), used for dialysis, were purchased from Spectrum Medical Industries Inc. Nanopure water (18 MΩ•cm) was acquired by means of a Milli-Q water filtration system, Millipore Corp. (Bedford, MA). Biology molecular grade water was purchased from Fisher Scientific (Pittsburg, PA).

3.2.2 Instruments

Ultraviolet-visible spectroscopy (UV-vis) absorption measurements were made using a UV-2550 system (Shimadzu Corp., Japan) using PMMA cuvettes. Spectra were analyzed with UV-Probe v. 2.33 software. Dynamic light scattering (DLS) measurements were conducted using Delsa Nano C from Beckman Coulter, Inc. (Fullerton, CA) equipped with a laser diode operating at 658 nm. Size measurements were made in nanopure water. Scattered light was detected at 15° angle and analyzed using a log correlator over 70 accumulations for a 0.5 mL of sample in a glass size cell (0.9 mL capacity). The photomultiplier aperture and the attenuator were automatically adjusted to obtain a photon counting rate of ca. 10 kcps. The calculation of the particle size distribution and distribution averages was performed using CONTIN particle size distribution analysis routines using Delsa Nano 2.31 software. The peak average of histograms from intensity, volume and number distributions out of 100 accumulations were reported as the average diameter of the particles, with the standard deviations being calculated as the breadth of the distributions. Transmission electron microscopy (TEM) bright-field imaging was conducted on a JOEL 1200 microscope, operating at 100 kV. The samples were prepared as follows: 4 µL of the dilute solution (with a polymer concentration of ca. 0.2 - 0.5 mg/mL) was deposited onto a carbon-coated copper grid, which was glow charged to increase the surface hydrophilicity. After 5 min, the excess of the solution was quickly wicked away by a piece of filter paper. The samples were then negatively stained with 4 µL of 1 wt% uranyl acetate aqueous solution. After 1 min, the excess uranyl acetate solution was quickly wicked away by a piece of filter paper and the samples were left to dry under ambient conditions overnight.

Paclitaxel levels were determined by (high performance liquid chromatography) HPLC analysis using two HPLC instruments. The first one is an Agilent 1200 HPLC with a (diode array detectors) DAD set to 230 nm in isocratic mode. A Kinetex XB-C18 column (2.1 x 100 mm, 2.6 µM, 100 Å) employed a buffer system of 55% water and 45% acetonitrile with both buffers modified with 0.05% trifluoroacetic acid (TFA) to minimize Paclitaxel degradation on the column. The flow rate is at 0.25 mL/min with run time of 15 min. The second one is a Shimadzu Prominence HPLC with RID-10A refractive index detector set to 227 nm in isocratic mode. The column is a Waters xBridge CB column (4.6 x 150 mm, 5 µM, 100 Å) with a eluent system composed of 55% 20 mM ammonium acetate buffer and 45% acetonitrile. The flow rate is at 1 mL/min with run time of 20 min. Both HPLC methods employed an external calibration of Paclitaxel (>99% purity) between 1-200 ng/µL. Paclitaxel level was also confirmed by Agilent liquid chromatography mass spectrometry (LC/MS) with a triple quadrapole mass spectrometer. The LC condition is same as the Agilent HPLC condition. PTX concentration was determined by measuring and fragmenting the sodiated molecular ion at 876.3 m/z and monitoring a key fragment ion for quantification at 308 m/z at the appropriate retention time.

3.2.3. Experiment procedures

General procedure for co-assembly of paclitaxel and PAA_{70}-*b*-PS_{555} into micelles (PTX-micelles): PAA_{70}-*b*-PS_{555} (*ca.* 10 mg) polymers were dissolved in DMF (10 mL) in a 100 mL round bottom flask and allowed to stir for 20 min at room temperature. Paclitaxel in DMSO (1.14 mg/mL) was added to the solution and allowed to stir for additional 10 min at room temperature. To this solution, an equal volume of nanopure water was added dropwise *via* a syringe pump over a period of 1 h. The reaction mixture was allowed to stir for additional 24 h at room temperature and dialyzed against nanopure water for 3 days in a presoaked dialysis tubing (MWCO *ca.* 6 - 8 kDa) to afford a micelle solution with a final polymer concentration of *ca.* 0.25 mg/mL.

60 nm micelles loaded with 20% PTX (PTX-micelle-60nm-20%): The PTX-micelle-60nm-20% solution had a final polymer concentration of 0.233 mg/mL, with PTX concentration of 0.0465 mg/mL.

60 nm micelles loaded with 15% PTX (PTX-micelle-60nm-15%): The PTX-micelle-60nm-15% solution had a final polymer concentration of 0.247 mg/mL, with PTX concentration of 0.0370 mg/mL.

60 nm micelles loaded with 10% PTX (PTX-micelle-60nm-10%): The PTX-micelle-60nm-10% solution had a final polymer concentration of 0.253 mg/mL, with PTX concentration of 0.0253 mg/mL.

60 nm micelles loaded with 5% PTX (PTX-micelle-60nm-5%): The PTX-micelle-60nm-5% solution had a final polymer concentration of 0.260 mg/mL, with PTX concentration of 0.0123 mg/mL.

General procedure for crosslinking the paclitaxel loaded nanoparticle micelles with the crosslinker to afford SCKs (PTX-SCK): To the micelle solution of paclitaxel loaded PAA_{70}-*b*-PS_{555} micelles was added a solution of fluorescent crosslinker in nanopure water (1.1 eq, nominal 20% crosslinking) dropwise *via* a syringe pump over a period of 2 h. To this solution, 1-[3´-(dimethylamino)propyl]-3-ethyl-carbodiimide methiodide (EDCI) in nanopure water (1.4 eq) was added dropwise *via* a syringe pump over 10 min and the resulting mixture was allowed to stir overnight before dialysis against nanopure water for 4 days in a presoaked dialysis tubing (MWCO.*ca.* 6 - 8 kDa) to afford SCK solutions with a final polymer concentration of *ca.* 0.25 mg/mL. The crosslinking density was measured by UV-vis spectroscopy to be about 7 - 10%.

60 nm SCKs loaded with 20% PTX (PTX-SCK-60nm-20%): The PTX-SCK-60nm-20% solution had a final polymer concentration of 0.233 mg/mL, with PTX concentration of 0.0465 mg/mL, and crosslinker concentration of 0.0825 mM at 7% of crosslinking density. Diameter = 63 ± 17 nm, D_h(intensity) = 230 ± 110 nm, D_h(volume) = 150 ± 60 nm, D_h(number) = 110 ± 30 nm.

60 nm SCKs loaded with 15% PTX (PTX-SCK-60nm-15%): The PTX-SCK-60nm-15% solution had a final polymer concentration of 0.247 mg/mL, with PTX concentration of 0.0370 mg/mL, and crosslinker concentration of 0.0748 mM at 8% of crosslinking density. Diameter = 57 ± 16 nm, D_h(intensity) = 240 ± 100 nm, D_h(volume) = 140 ± 60 nm, D_h(number) = 110 ± 30 nm.

60 nm SCKs loaded with 10% PTX (PTX-SCK-60nm-10%): The PTX-SCK-60nm-10% solution had a final polymer concentration of 0.253 mg/mL, PTX concentration of 0.0253 mg/mL, and crosslinker concentration of 0.0874 mM at 9% of crosslinking density. Diameter = 59 ± 12 nm, D_h(intensity) = 230 ± 90 nm, D_h(volume) = 140 ± 60 nm, D_h(number) = 110 ± 30 nm.

60 nm SCKs loaded with 5% PTX (PTX-SCK-60nm-20%): The PTX-SCK-60nm-5% solution had a final polymer concentration of 0.260 mg/mL, PTX concentration of 0.0123 mg/mL, and crosslinker concentration of 0.0698 mM at 6% of crosslinking density. Diameter = 65 ± 14 nm, D_h(intensity) = 220 ± 90 nm, D_h(volume) = 150 ± 60 nm, D_h(number) = 120 ± 30 nm.

General procedure for assembly of PAA_{120}-*b*-PS_{100} into micelles and *in situ* crosslinking: PAA_{120}-*b*-PS_{100} (*ca.* 10 mg) polymers were dissolved in DMF (10 mL) in a 100 mL round bottom flask and allowed to stir for 20 min at room temperature. Paclitaxel in DMSO (1.14 mg/mL) was added to the solution and allowed to stir for additional 10 min at room temperature. To this solution, an equal volume of nanopure water was added dropwise *via* a syringe pump over a period of 1 h. The reaction mixture was allowed to stir for additional 24 h at room temperature. A solution of fluorescent crosslinker in nanopure water (1.1 eq, nominal 20% crosslinking) was added dropwise *via* a syringe pump over a period of 2 h. To this solution, 1-[3´-(dimethylamino)propyl]-3-ethyl-carbodiimide methiodide (EDCI) in nanopure water (1.4 eq) was added dropwise *via* a syringe pump over 10 min and the resulting mixture was allowed to stir overnight before dialysis against nanopure water for 4 days in a presoaked dialysis tubing (MWCO.*ca.* 6 - 8 kDa) to afford SCK solutions with a final polymer concentration of *ca.* 0.25 mg/mL. The crosslinking density was measured by UV-vis spectroscopy to be about 7 - 10%.

20 nm SCKs loaded with 5% PTX (PTX-SCK-20nm-5%): The PTX-SCK-20nm-5% solution had a final polymer concentration of 0.279 mg/mL, PTX concentration of 0.0135 mg/mL, and crosslinker concentration of 0.0799 mM at 8% of crosslinking density. Diameter = 24 ± 3 nm, D_h(intensity) = 120 ± 60 nm, D_h(volume) = 60 ± 30 nm, D_h(number) = 49 ± 13 nm.

20 nm PEGylated SCKs loaded with 5% PTX (PTX-PEG-SCK-20nm-5%): The PTX-PEG-SCK-20nm-5% solution had a final polymer concentration of 0.222 mg/mL, PTX concentration of 0.0111 mg/mL, and crosslinker concentration of 0.0563 mM at 5% of crosslinking density. Diameter = 21 ± 6 nm, D_h(intensity) = 400 ± 379 nm, D_h(volume) = 70 ± 50 nm, D_h(number) = 49 ± 15 nm.

3.2.3.4 General procedure for assembly of PAA_m-*b*-PS_n into micelles: PAA_m-*b*-PS_n (*ca.* 10 mg) polymers were dissolved in DMF (10 mL) in a 100 mL round bottom flask and allowed to stir for 20 min at room temperature. To this solution, an equal volume of nanopure water was added dropwise *via* a syringe pump over a period of 1 h. The reaction mixture was allowed to stir for additional 24 h at room temperature and dialyzed against nanopure water for 3 days in a presoaked dialysis tubing (MWCO *ca.* 6 - 8 kDa) to afford a micelle solution with a final polymer concentration of *ca*. 0.25 mg/mL.

60 nm micelles (Micelle-60nm): The Micelle-60nm solution had a final polymer concentration of 0.267 mg/mL.

20 nm micelles (Micelle-20nm): The Micelle-20nm solution had a final polymer concentration of 0.269 mg/mL.

20 nm PEGylated micelles (PEG-micelle-20nm): The PEG-micelle-20nm solution had a final polymer concentration of 0.260 mg/mL.

General procedure for crosslinking the paclitaxel loaded nanoparticle micelles with the fluorescent crosslinker to afford SCKs (PTX-SCK): To the micelle solution of paclitaxel loaded PAA_m-*b*-PS_n micelles was added a solution of MP-3142 in nanopure water (1.1 eq, nominal 20% crosslinking) dropwise *via* a syringe pump over a period of 2 h. To this solution, 1-[3´-(dimethylamino)propyl]-3-ethyl-carbodiimide methiodide (EDCI) in nanopure water (1.4 eq) was added dropwise *via* a syringe pump over 10 min and the resulting mixture was allowed to stir overnight before dialysis against nanopure water for 4 days in a presoaked dialysis tubing (MWCO.ca. 6 - 8 kDa) to afford SCK solutions with a final polymer concentration of *ca.* 0.25 mg/mL. The crosslinking density was measured by UV-vis spectroscopy to be about 7 - 10%.

60 nm SCKs (SCK-60nm): The SCK-60nm solution had a final polymer concentration of 0.267 mg/mL, and MP-3142 concentration of 0.0783 mM at 7% of crosslinking density. Diameter = 55 ± 15 nm, D_h(intensity) = 244 ± 105 nm, D_h(volume) = 151 ± 58 nm, D_h(number) = 116 ± 30 nm.

20 nm SCKs (SCK-20nm): The SCK-20nm solution had a final polymer concentration of XX 0.269 mg/mL, and MP-3142 concentration of 0.0723 mM at 7% of crosslinking density. Diameter = 23 ± 3 nm, D_h(intensity) = 110 ± 50 nm, D_h(volume) = 70 ± 30 nm, D_h(number) = 56 ± 15 nm.

20 nm PEGylated SCKs (PEG-SCK-20nm): The PEG-SCK-20nm solution had a final polymer concentration of 0.260 mg/mL, and MP-3142 concentration of 0.0564 mM at 5% of crosslinking density. Diameter = 25 ± 5 nm, D_h(intensity) = 320 ± 280 nm, D_h(volume) = 70 ± 50 nm, D_h(number) = 48 ± 14 nm.

Cell viability studies: All the SCKs and free paclitaxel were tested in KB cells. KB cells (ATCC, Mansas, VA) were maintained in monolayer cultures in folate free RPMI (Life Technologies, Carlsbad, CA) supplemented with 10% fetal bovine serum (FBS) and penicillin/streptomycin antibiotics. For screening purposes, 2,500 cells in 100 μL of complete RPMI were plated in a 96 well plate (Corning, Lowell, MA) in triplicates and were then incubated for 24 h in a humidified CO_2 cell culture incubator maintained at 37 °C. Serial dilutions of SCKs and paclitaxel were prepared in PBS and added to cells in a volume of 10 μL. The cells were either incubated for a short period of 2 h or for continuous incubation of 72 h. After 2 h incubation the media was replaced with 110 μL of fresh complete RPMI. Cell viability was assessed by using a colorimetric WST-1 cell proliferation kit (Roche, Indianapolis, Indiana). Cell viability was calculated as a percentage of the control cells treated with no drugs. The percent cell viability assay values were then plotted in Graph Pad Prism (GraphPad Software Inc, La Jolla, CA) and IC_{50} values were obtained using non-linear regression four parameters curve fit. Cell studies were performed in triplicates and each experiment was performed twice.

Confocal microscopy: KB cell internalization of SCKs was investigated using Nikon A1 confocal microscope. KB cells were plated in an eight well chamber Labtek II glass slide system (Nalgene Nunc, Denmark) at a density of 35,000 cells per well. The slides were incubated overnight in a humidified CO_2 incubator at 37 °C. Cells were then incubated with SCKs for 2 h followed by extensive washing with PBS. The cells were fixed with 4% formaldehyde for 20 min at room temperature, then mounted with ProGold Antifade mounting media containing DAPI (Life Technologies, Carlsbad, CA) and visualized with Nikon A1 confocal microscope (Nikon Instruments, Melville, NY). The pyrazine crosslinkers of the SCKs were excited with 488 nm laser and emission was collected with a Texas Red filter (595 nm - 630 nm). The images were collected with a 60X oil immersion objective.

3.3. Results and discussion

The PTX-loaded SCK nanoparticles were prepared from previously reported PAA-*b*-PS amphiphilic block copolymers,[39] through a co-assembly process that allowed the particle formation in the presence of the drug molecule to incorporate the highly water insoluble PTX into the hydrophobic core of initial block copolymer micelles, and then further stabilization of the nanostructures by covalent crosslinking using a pyrazine-based dye serving both as the crosslinker and a chromophore. The crosslinking chromophore[92] has been investigated previously as a pH-reporting[93-95] and as a guest-gating moiety.[91] Water (a selective solvent for the PAA block segment) was introduced to a DMF (a good solvent for both PAA and PS) solution of the block copolymer homogeneously mixed with PTX dissolved in DMSO, dropwise *via* a syringe pump to form discrete spherical micelles loaded with PTX. The PAA shell regions of these micelles were then crosslinked *via* amidation chemistry with the pyrazine diamine crosslinker, in the presence of 1-[3′-(dimethylamino)propyl]-3-ethylcarbodiimide methiodide (EDCI) to afford PTX-loaded SCK nanoparticles.

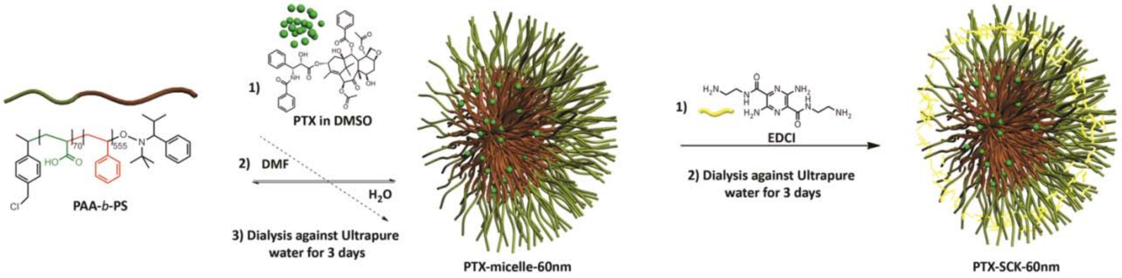

Figure 3.1. Co-assembly of PAA_{70}-*b*-PS_{555} block copolymers in DMF with paclitaxel in DMSO to construct 60 nm PTX-loaded micelles (PTX-micelle-60nm), followed by dialysis to remove the organic solvents. Crosslinking with the pyrazine chromophore crosslinker, using EDCI as the coupling agent followed by dialysis to remove free crosslinker and EDCI byproducts to obtain PTX-loaded SCKs (PTX-SCK-60nm). .

To achieve high PTX incorporation, nanoparticles with a relatively large polystyrene core diameter, 60 nm, were used to accommodate the hydrophobic PTX (Figure 3.1). The 60 nm nanoparticles were constructed from an amphiphilic block copolymer with a low hydrophilic/hydrophobic ratio, provided by a long polystyrene chain, PAA_{70}-*b*-PS_{555}. Initially, a post-assembly loading method was attempted, where PTX dissolved in DMSO was added into aqueous solutions of pre-established SCK nanoparticles, but precipitation was observed after one hour. Therefore, a co-assembly loading method was adapted, where water was introduced into a homogeneous solution of PTX dissolved in DMSO and the block copolymer precursor dissolved in DMF to induce self-assembled micelle formation, followed by extensive dialysis to remove the organic solvents. Crosslinking with the chromophoric diamino pyrazine-based crosslinker then afforded the corresponding SCKs, and extensive dialysis was performed again to remove the free crosslinkers and EDCI byproducts. By varying the feed ratio of

PTX concentration, four different PTX-loaded SCK formulations with targeted theoretical loading percentages of *ca*. 5, 10, 15 and 20 wt% were prepared.

The dimensions of the SCKs, with and without PTX, were characterized by transmission electron microscopy (TEM) and dynamic light scattering (DLS) (Table 3.1). From TEM micrographs, the nanoparticles were observed to have a circular shape, suggesting a spherical morphology with core diameters of *ca*. 60 ± 15 nm for both empty SCKs and PTX-loaded SCKs. Their number-average hydrodynamic diameters, characterized by DLS, were also similar across loading percentages with narrow size distributions of *ca*. 120 ± 30 nm (Figure 3.2).

Table 3.1. Summary of characterization data for 60 nm SCKs by TEM and DLS.

	Diameter by TEM (nm)	D_h (intensity) (nm)	D_h (volume) (nm)	D_h (number) (nm)
SCK-60nm	55 ± 15	240 ± 110	150 ± 60	120 ± 30
PTX-SCK-60nm-20%	63 ± 17	230 ± 100	140 ± 60	110 ± 30
PTX-SCK-60nm-15%	57 ± 16	240 ± 100	140 ± 60	110 ± 30
PTX-SCK-60nm-10%	59 ± 12	230 ± 90	140 ± 60	110 ± 30
PTX-SCK-60nm-5%	65 ± 14	220 ± 90	150 ± 60	120 ± 30

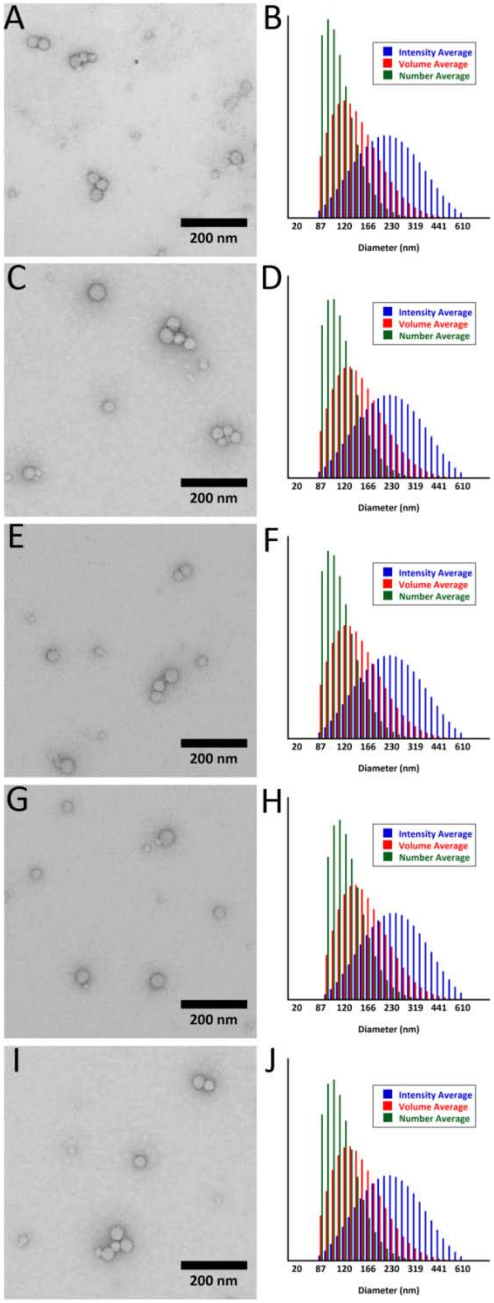

Figure 3.2. Left column: TEM images (drop deposited on carbon-coated copper grids and stained negatively with 1% aqueous uranyl acetate) of A. SCK-60nm; C. PTX-SCK-60nm-20%; E. PTX-SCK-60nm-15%; G. PTX-SCK-60nm-10%; I. PTX-SCK-60nm-5%. Right column: DLS histograms (determinations were average values from ten measurements, with the standard deviations being calculated as the breadth of the distributions) of B. SCK-60nm; D. PTX-SCK-60nm-20%; F. PTX-SCK-60nm-15%; H. PTX-SCK-60nm-10%; J. PTX-SCK-60nm-5%.

All PTX-loaded 60 nm formulations showed excellent cell killing abilities that were comparable to free PTX cell killing effect when incubated with KB cells for 2 h and also continued incubation for 72 h, whereas empty nanoparticles did not show any cytotoxicity even at high concentrations (Table 3.2). At various loading amounts that were attempted, the recovered PTX concentration analyzed by high performance liquid chromatography (HPLC) was *ca.* 50% of the targeted amount. We hypothesized that during the long dialysis processes after the micelle assembly and crosslinking procedures, portions of PTX were gradually diffused from the nanoparticles resulting in the lowered final recovered concentration. However, even at 50% of the targeted concentration, the PTX-loaded 60 nm SCKs were able to exhibit excellent cell killing, due to the localization of high PTX concentration within each nanoparticle and the slow release from each nanoparticle (Figure 3.3). The PTX-loaded SCKs with the lowest targeted PTX concentration (PTX-SCK-60nm-5%) showed the best cell killing ability among all other samples, and achieved an 0.028 μM IC_{50} value, which was approximately half of that of free PTX (0.046 μM) at 2 h incubation periods.

Table 3.2. Summary of various formulations of PTX-loaded SCKs (IC$_{50}$ values were measured at both 2 h and 72 h incubation periods when incubated with KB cells *in vitro*).

	Polymer conc. (mg/mL)	Attempted PTX conc. (µg/mL)	Actual PTX conc. (µg/mL)	Actual wt %	% yield	IC$_{50}$ at 2 h (µM)	IC$_{50}$ at 72 h (µM)
SCK-60nm	0.267	-	-	-	-	-	-
Free PTX	-	-	-		-	0.046 ± 0.001	0.003 ± 0.002
PTX-SCK-60nm-20%	0.233	46.5	21.7	8.5	47	0.043 ± 0.010	0.011 ± 0.001
PTX-SCK-60nm-15%	0.247	37.0	19.5	7.3	53	0.050 ± 0.011	0.012 ± 0.001
PTX-SCK-60nm-10%	0.253	25.3	15.7	5.8	62	0.040 ± 0.007	0.009 ± 0.001
PTX-SCK-60nm-5%	0.260	12.3	7.6	2.8	61	0.028 ± 0.003	0.006 ± 0.001

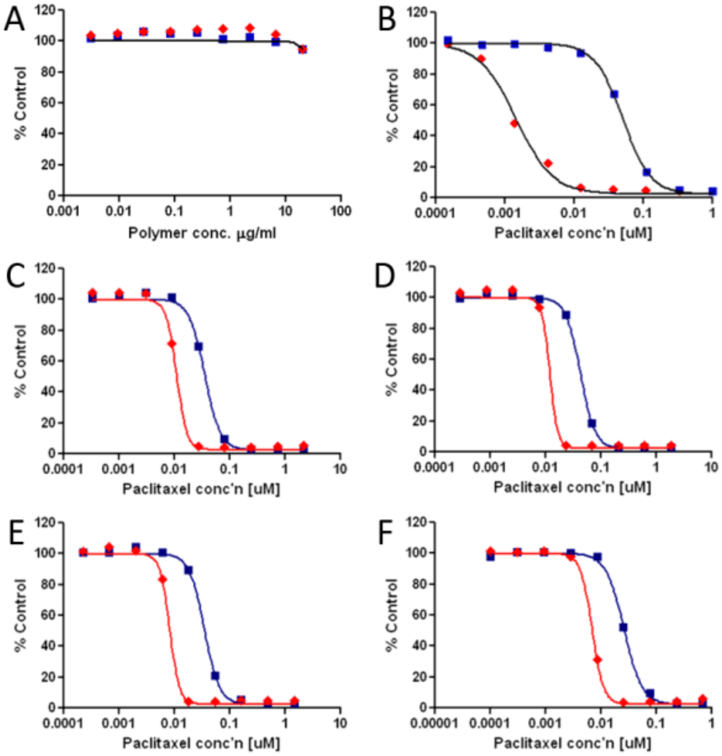

Figure 3.3. Viability of KB cells incubated with A. SCK-60nm; B. Free PTX; C. PTX-SCK-60nm-20%; D. PTX-SCK-60nm-15%; E. PTX-SCK-60nm-10%; F. PTX-SCK-60nm-5%. The percentage cell viability was measured by WST-1 assay. Blue squares, 2 h; red diamonds, 72 h.

The actual concentration of the PTX incorporated into the SCKs was only 50% of the attempted concentration, but analytical filtration experiments indicated that the cell killing was a result of the encapsulated PTX, instead of free PTX. Both free PTX solution and PTX-SCK solution were passed through a centrifugal filtering device with a molecular weight cut-off (MWCO) of 50 kDa, the residues on the filter and the filtrate were analyzed by HPLC and liquid chromatography mass spectrometry (LC/MS), with both analyses giving similar results (Figure 3.4). In the free PTX solution, there was no PTX detected on the filter, but rather 100% PTX was detected in the filtrate. However, once the PTX was encapsulated into SCK nanoparticles, when passing through the filtering device, no PTX was observed in the filtrate. Subsequently, the PTX was readily released from the PTX-SCK nanoparticles when exposed to the presence of organic solvent during the chromatography step of the methods. This simple analytical experiment indicated that the cell killing was due to PTX-SCK, not free PTX.

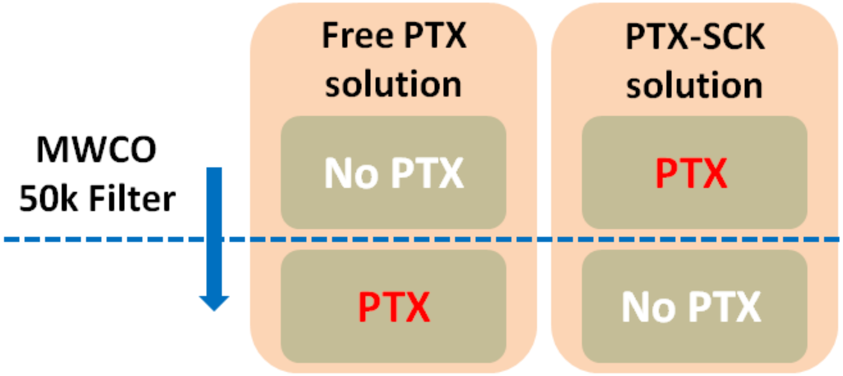

Figure 3.4. Illustration of the location of free PTX *vs*. PTX-SCK in a centrifugal filtering experiment using 50 kDa MWCO filter.

Since size and surface characteristics of the nanoparticles play important roles in passive targeting delivery methods through the EPR effect, we also wanted to investigate whether particle size and surface PEGylation had effects on the cell killing abilities. Therefore, a block copolymer, PAA_{120}-*b*-PS_{100}, with a relatively short hydrophobic segment was used to construct nanoparticles of 20 nm in diameter. The 20 nm SCK nanoparticles were also functionalized with polyethylene oxide (PEO), by grafting a PEO unit onto the backbone of the polymer precursor through amidation chemistry with the coupling agent EDCI, to be used as a precursor to self assemble into PEGylated nanoparticles (Figure 3.5) to ultimately improve the *in vivo* biodistribution. As previously reported,[96] covalent attachment of PEO onto the block copolymer precursor was performed before self assembly, as opposed to onto a final nanoparticle, which allowed for control over the conjugation chemistry as well as determination of the extent of PEO chains that were actually covalently linked onto the final nanoparticle structures. Because the 5 wt%-loaded 60 nm SCKs gave optimum cell killing, the theoretical PTX loading in the non-PEGylated and PEGylated 20 nm SCKs was kept constant at 5 wt%. To minimize loss of PTX during the original extensive dialysis process both after micellization and crosslinking, *in situ* crosslinking was performed after the self assembly process, and dialysis was only performed once altogether after crosslinking. The dialysis period was also shortened to one day, instead of three days, but with frequent water change to facilitate removal of the organic solvent, free crosslinker, and EDCI byproduct.

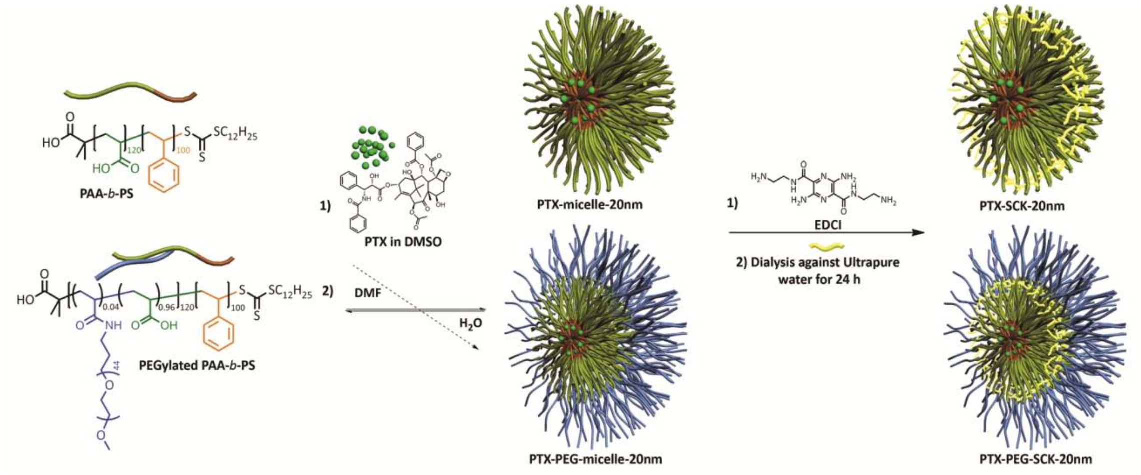

Figure 3.5. Co-assembly of PAA-*b*-PS or PEGylated PAA-*b*-PS in DMF with PTX in DMSO to construct 20 nm PTX loaded micelles, followed by *in situ* crosslinking with the pyrazine chromophore crosslinker, using EDCI as the coupling agent. The final 20 nm PTX-loaded SCKs in aqueous solutions were obtained after performing dialysis to remove organic solvent, free crosslinker and EDCI by products.

The dimensions of both PTX-loaded SCKs and PTX-loaded PEGylated SCKs were characterized by TEM and DLS (Table 3.3). As a comparison, non-PEGylated and PEGylated SCKs without PTX were also characterized. The well-defined circularly-shaped images observed by TEM suggested that the empty SCKs were spherical with a narrow size distribution of 23 ± 3 nm (Figure 3.6). PTX-loaded SCKs were also spherical with a comparable size distribution of 24 ± 3 nm, indicating that the PTX incorporation did not affect the size or the shape of the SCKs. However, the TEM micrographs of the PEGylated SCKs showed distinct differences in morphology than the non-PEGylated SCKs. From the micrographs, the PEGylated SCKs appeared to be more ill defined in shape with thick corona and rough edges, presumably due to the interactions of the hydrophilic PEO chains with the stain and the grids. The dry-state core diameters of PEGylated SCKs were about the same as non-PEGylated SCKs, as measured by TEM, but the effect of the PEGylation on the SCK hydrodynamic diameter was more prominent, as confirmed by DLS measurements. The intensity-average hydrodynamic diameters of the PEGylated SCKs were more than twice the diameters of non-PEGylated SCKs (*ca.* 300 nm *vs*. 120 nm). However, the number-average hydrodynamic diameters of the SCKs were determined to be 50 ± 15 nm by DLS, regardless of PTX incorporation and PEGylation.

Table 3.3. Summary of characterization data for the 20 nm SCKs by TEM and DLS.

	Diameter by TEM (nm)	D_h (intensity) (nm)	D_h (volume) (nm)	D_h (number) (nm)
SCK-20nm	23 ± 3	110 ± 50	70 ± 30	56 ± 15
PTX-SCK-20nm-5%	24 ± 3	120 ± 60	60 ± 30	49 ± 13
PEG-SCK-20nm	25 ± 5	320 ± 280	70 ± 40	48 ± 14
PEG-PTX-SCK-20nm-5%	21 ± 6	400 ± 380	70 ± 50	49 ± 15

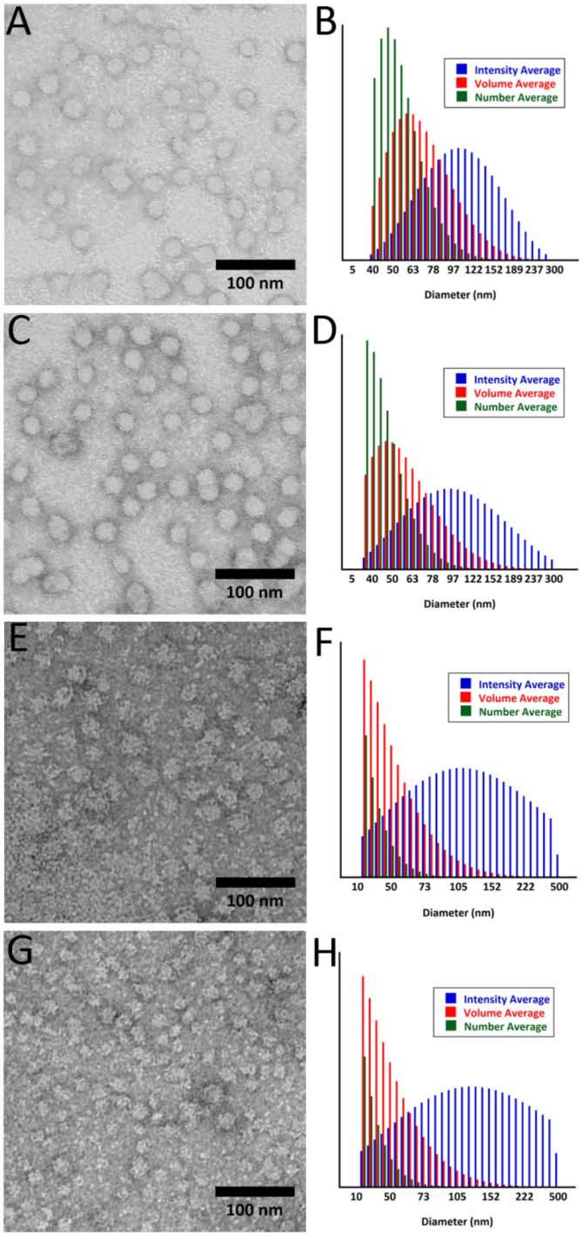

Figure 3.6. Left column: TEM images (drop-deposited on carbon-coated copper grids and stained negatively with 1% aqueous uranyl acetate) of A. SCK-20nm; C. PTX-SCK-20nm-5%; E. PEG-SCK-20nm; G. PTX-PEG-SCK-20nm-5%. Right column: DLS histograms (determinations were average values from ten measurements, with the standard deviations being calculated as the breadths of the distributions) of B. SCK-20nm; D. PTX-SCK-20nm-5%; F. PEG-SCK-20nm; H. PTX-PEG-SCK-20nm-5%.

All PTX-loaded 20 nm formulations showed excellent cell killing abilities that were comparable to free PTX cell killing effect when incubated with KB cells for 2 h and also continued incubation for 72 h (Table 3.4, Figure 3.7). Similar to empty 60 nm SCKs without PTX, empty 20 nm SCKs showed no cytotoxicity even at high concentrations. PEGylation did not appear to affect the cell killing abilities of PTX-loaded SCK samples as evident from IC_{50} values that were comparable to those of non PEGylated PTX-loaded SCKs and free PTX. PEGylation also did not affect the cell internalization ability of the SCKs, as demonstrated by confocal fluorescence microscopy (Figure 3.8A-D). PEGylated and non-PEGylated nanoparticles internalized into KB cells within 2 h and those loaded with PTX released their payload, resulting in cytotoxicity, as evident from the fragmented nuclei present (Figure 3.8E-F).

Table 3.4. Summary of various formulations of PTX-loaded SCKs (IC_{50} values were measured at both 2 h and 72 h incubation periods when incubated with KB cells *in vitro*).

	Attempted PTX conc. (µg/mL)	Actual PTX conc. (µg/mL)	Actual wt %	% yield	IC_{50} at 2 h (µM)	IC_{50} at 72 h (µM)
SCK-20nm	-		-		-	-
PTX-SCK-20nm-5%	13.5	12.4	4.3	92	0.021 ± 0.013	0.004 ± 0.002
PEG-SCK-20nm	-		-		-	-
PEG-PTX-SCK-20nm-5%	11.1	11.0	4.7	100	0.055 ± 0.015	0.009 ± 0.007

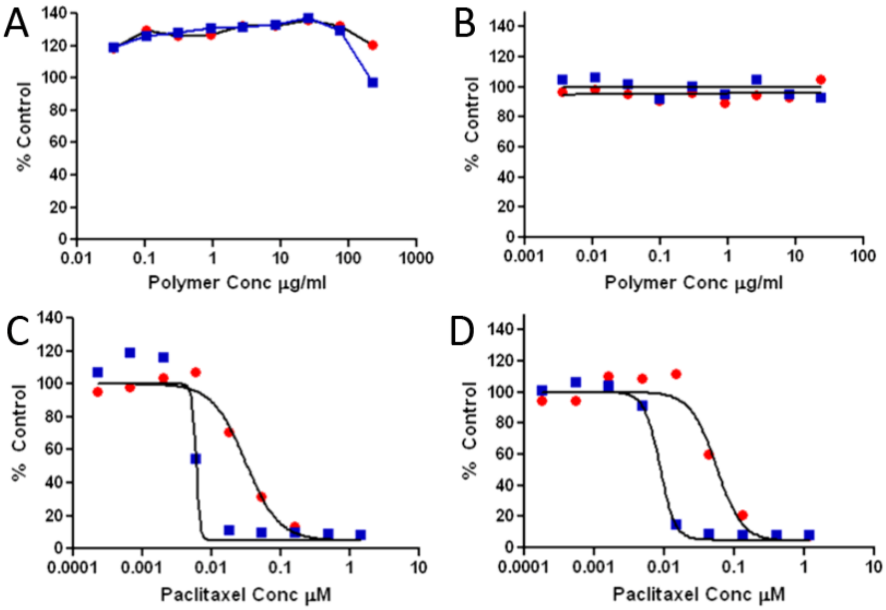

Figure 3.7. Viability of KB cells incubated with A. SCK-20nm; B. PEG-SCK-20nm; C. PTX-SCK-20nm-5%; D. PTX-PEG-SCK-20nm-5%. The percentage cell viability was measured by WST-1 assay. Red dots, 2 h; blue squares, 72 h.

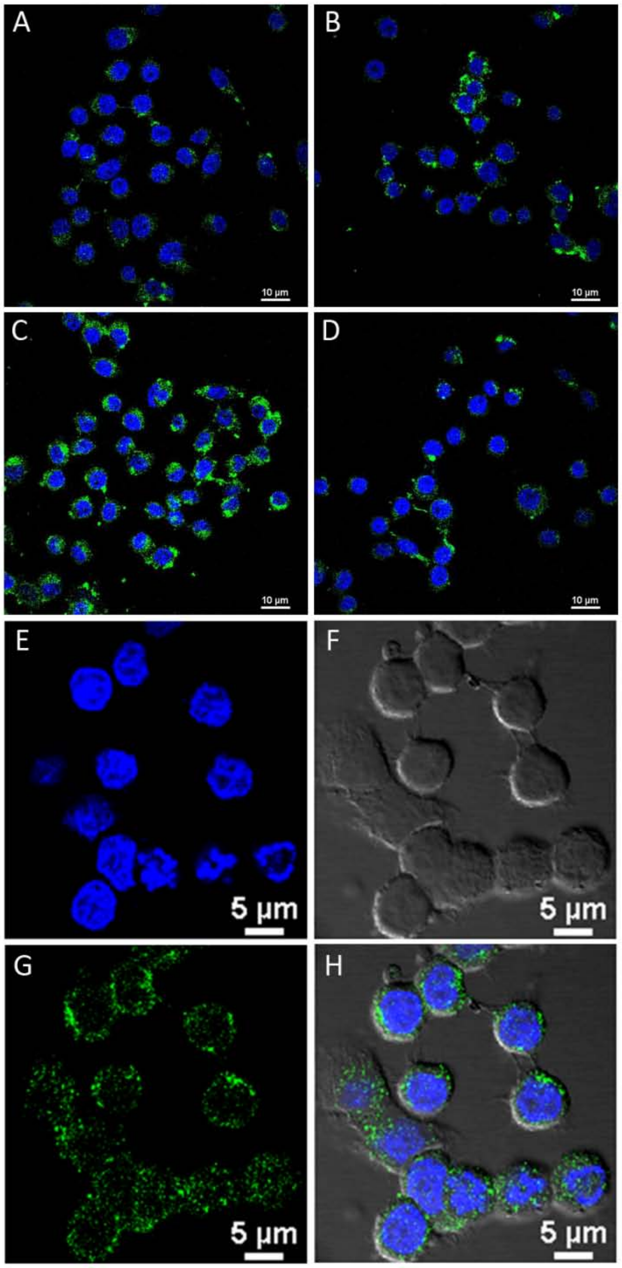

Figure 3.8. Intracellular uptake of A. SCK-20nm; B. PEG-SCK-20nm; C. PTX-SCK-20nm-5%; D. PTX-PEG-SCK-20nm-5% in KB cells. Cells were incubated with a single concentration of each different type of SCK for 2 h. Cells were then fixed with 4% PFA, mounted with media containing DAPI, and subsequently imaged with Nikon A1 confocal microscope. Fragmented nuclei in cells were observed after incubation with PTX-SCK-20nm-5% for 2 h: E. DAPI staining; F. Transmission detector (TD) image; G. Acridine orange staining; H. Overlay of DAPI staining, TD, and acridine orange staining.

3.4. Conclusions

The main route of delivery for many simple, yet effective, formulations of PTX, such as Abraxane®, is through a leaky vasculature found in cancerous cells, a phenomenon known as the enhanced permeation and retention (EPR) effect.[97] Although the EPR effect may provide some selectivity, to further reduce the overall toxicity of the drug-nanoparticle formulation, a combination with active targeting is favored over passive targeting alone. Therefore, functional sub-100 nm platforms with a core shell morphology are highly desired for encapsulation of hydrophobic drug molecules within the core and covalent attachment of targeting ligands on the surface for combined passive and active modes of targeting, thereby maximizing the therapeutic efficacy upon delivery. For instance, half-antibody functionalized lipid-polymer hybrid nanoparticles (*ca*. 100 nm) loaded with PTX have been reported for targeted drug delivery to carcinoembryonic antigen presenting pancreatic cancer cells.[98] Herein, we have reported a successful preparation of PTX-loaded, functional nanoparticles with varying sizes and surface characteristics, all of which demonstrated cell killing abilities that were comparable to or better than free PTX. The size variations in nanoparticles did not result in any significant differentiation in IC_{50} in KB cells. However, we expect the size differences will have an effect on accumulation and micro distribution in solid tumors as suggested by Cabral *et al*.[99,100] The nanoparticles had tunable hydrodynamic diameters as well as core/shell dimensions. Facile tuning of these nanoscale dimensions arose from the ability to control the length of hydrophilic/hydrophobic units of the block copolymers that served as the building blocks for the nanoparticles. The hydrophilic

PAA block was used to covalently attach PEO units. Conjugation of targeting ligands onto the remaining PEO termini or to the PAA chains is expected to further enhance the ability of the overall nanoparticle system to actively target for increased potency.[101,102] In addition to the incorporation of targeting ligands, future studies will include *in vivo* evaluations of the PEGylated PTX-loaded SCKs and utilization of degradable core units for bioclearance of the nanoparticle upon delivery.

3.5. Acknowledgments

Financial support from Covidien is gratefully acknowledged. K. L. Wooley serves as a consultant to Covidien. This work was also supported by the Welch Foundation through the W. T. Doherty-Welch Chair in Chemistry, Grant No. A-0001.

CHAPTER IV

SYNTHESIS, CHARACTERIZATION, AND *IN VIVO* EFFICACY EVALUATION OF SHELL CROSSLINKED NANOPARTICLE FORMULATIONS CARRYING SILVER ANTIMICROBIALS AS ANTI-PSEUDOMONAL THERAPEUTICS

4.1. Introduction

Cystic fibrosis (CF), a diseases that affects about 70,000 humans worldwide, results from mutations in both alleles of the cystic fibrosis transmembrane conductance regulator (CFTR) gene,[103] and is the most common life-shortening genetic disease among Caucasians.[104] This disease affects multiple organs including the lungs and upper respiratory tract, the gastrointestinal tract, pancreas, liver, sweat glands, and genitourinary tract. Compared with a biphasic mucus layer in the normal airway, CF airway is covered with a viscous mucus layer caused by either mucus secretion, mucus reabsorption or both.[103] Consequently, the bacteria can easily colonize and persist in the airway and form biofilms. A variety of opportunistic pathogens including *Pseudomonas aeruginosa* (*P. aeruginosa*), *Staphylococcus aureus* (SA), and *Burkholderia cepacia* complex (BCC) cause chronic pulmonary infections and subsequent intense persistent inflammation, which is a major cause of the morbidity and mortality in these patients.[103]

The current paradigm for the treatment of chronically infected CF patients consists of frequent high-dose administration of intravenous antibiotics such as aminoglycosides and β-lactams.[105] While antibiotic, chemotherapy and chemoprophylaxis have reduced the morbidity and early mortality of CF patients from infections, the intrinsic ability of these pathogens to develop resistance against many commonly used antibiotics rendering this microbe to be highly problematic. The ability of the organisms to form biofilm prevents their complete eradication even with aggressive therapy. In the case of *P. aeruginosa*, the phenotypic variants with an enhanced capacity for biofilm formation are also highly antibiotic-resistant compared with the parent strains.[106] *P. aeruginosa* develops antibiotic resistance through multiple mechanisms including mutations in single genes and up-regulation of efflux pumps, making these infections extremely difficult to treat.[107,108] Similarly, the proportion of CF patients colonized with methicillin-resistant *Staphylococcus aureus* (MRSA) continues to escalate.[109,110] Colonization with BCC organisms poses a life-threatening problem, as they are inherently antibiotic resistant.[111] Furthermore, the frequent administration of intravenous high dose antibiotics necessary to achieve a clinically relevant serum concentration of the drug can potentially result in severe side effects. Therefore, to combat the problems associated with toxicity and antimicrobial resistance, there is a great need for finding new modalities of treatment.[112]

Silver, one of the oldest antimicrobial agents, has a historical significance. Humans have known and used silver for its natural antimicrobial properties for thousands of years. Hippocrates had noted that silver possessed beneficial healing and anti-disease properties around 400 BC. Today, silver's antimicrobial property is utilized extensively: silver compounds are used as antimicrobial agents for the treatment of wounds and burns in topical cream containing 1% silver sulfadiazine,[113,114] as coatings when impregnated into polymers for catheters and endotracheal tubes,[115] and as disinfectants.[116,117] In addition to its broad-spectrum activity against microorganisms, the relatively few reported accounts of silver resistance despite its widespread and continuous use make silver-based antimicrobials very attractive. Silver has been demonstrated to be effective against bacteria, including *P. aeruginosa*, *Staphylococcus aureus,* and *Escherichia coli* (*E. coli*) as well as fungal pathogens.[118] The mechanisms of action are incompletely understood, but might include poisoning of the respiratory electron transport chain, inhibition of DNA replication, and/or direct or indirect damage to cell envelopes.[119] Furthermore, the active component of silver-based antimicrobials, Ag^+, exhibits low toxicity to human tissues.[113,120,121] Therefore, there has been a recent resurgence in the development of silver-based systems in order to harness the advantages of silver for therapeutic delivery and anti-fouling purpose. For instance, Sen and coworkers have reported poly (4-vinyl-N-hexylpyridinium bromide) cationic polymer/silver bromide nanoparticle composites that demonstrated potent long-lasting antibacterial activity.[122] Tiller, Mecking and coworkers have developed nanoscaled hybrids of silver nanoparticles and amphiphilic hyperbranched macromolecules composed of polyethyleneimine, which exhibited antimicrobial properties when applied as surface coatings.[123]

Our research group in collaboration with Youngs *et al.* have synthesized and characterized a series of N-heterocyclic silver carbene complexes (SCCs).[124-127] This new class of silver-based antimicrobials with improved stability to light and aqueous solutions has been found to be active against a wide variety of Gram-positive and Gramnegative pathogens including antibiotic-resistant *P. aeruginosa*, MRSA, and BCC species isolated from the lungs of CF patients as well as biosafety level 3 (BSL3) organisms.[124-127] These compounds can be easily nebulized, providing a means to directly administer these antimicrobials to the lung *via* an inhalational route, a method that has been previously explored and proven effective due to localized delivery at the site of infection.[128] A major advantage of the nebulization method is the ability to achieve therapeutic outcomes with lower antibiotic dosages, which results in diminished systemic absorption and decreased systemic toxicity. However, due to the relatively small size of these molecules, the challenge of rapid clearance from the lungs following administration can still be expected.[128] Instead of relying on the administration of several inhaled dosages to maintain effective therapeutic concentration above the minimum inhibitory concentration (MIC) of the bacteria within the lung, a strategy that poses potential patient compliance problems, we have sought to investigate the use of inhaled nanoparticles loaded with SCCs. For example, Cannon and Youngs *et al*. have previously reported on the antimicrobial efficacy of SCC10 encapsulated within L-tyrosine polyphosphate (LTP) nanoparticles both *in vitro* and *in vivo.*[129] These nanoparticles are capable of providing a sustained release of their therapeutic payload directly at the site of infection following their administration thereby promising improved therapeutic efficacy.[129,130]

Thus, we have developed multifunctional, polymeric nanoparticles that are optimized for encapsulation and delivery of silver and/or SCC. Through localization of the payloads onto the target site, these nanoconstructs serve as theranostics to treat lung infections in cycstic fibrosis patients with increased therapeutic efficacy,. Amphiphilic, shell crosslinked knedel-like nanoparticles (SCKs) are used as a novel drug delivery system for the packaging and delivery of silver antimicrobial agents. These SCK nanoparticles were synthesized from an amphiphilic diblock copolymer, poly(acrylic acid)-*b*-polystyrene (PAA-*b*-PS), in which hydrophobic SCCs were encapsulated into the hydrophobic polystyrene of the SCK nanoparticles and silver cation was being complexed to the acrylic acid presented on the shell of the nanoparticles. Previous *in vitro* studies of the silver-loaded SCKs have demonstrated good MIC in both *E.coli* UTI89 strain and *P. aeruginosa* PAM57-15 strain.[131] Herein, we have investigated the therapeutic efficacy of these silver-loaded SCKs *in vivo* through nebulization treatment in *P. aeruginosa* infected mice, and demonstrated excellent efficacy towards rescuing mice from bacterial infection in the lung.

4.2. Materials and methods

4.2.1. Materials

All chemicals were purchased from Sigma-Aldrich Chemical Co. (St. Louis, MO) and used without further purification unless otherwise indicated. SCC10 and SCK (20% crosslinked, 0.274 mg/mL, prepared from PAA_{120}-*b*-PS_{40}) were synthesized as previously reported.[39] Amicon® ultra centrifugal filter devices (100 kDa MWCO) were purchased from Millipore Corp. (Bedford, MA). Nanopure water (18 MΩ·cm) was acquired by means of a Milli-Q water filtration system (Millipore Corp., Bedford, MA).

4.2.2. Instruments

Ultraviolet-visible spectroscopy (UV-vis) absorption measurements were made using a UV-2550 system (Shimadzu Corp., Japan) with PMMA cuvettes. Inductively coupled plasma-mass spectrometry (ICP-MS) was performed on a Perkin Elmer SCIEX ICP Mass Spectrometer ELAN DRC II, equipped with high speed quadrupole, Dynamic Reaction Cell™ (DRC) and Axial Field™ Technology (AFT) to completely eliminate polyatomic interferences, using 1% HNO_3 as the matrix and indium as the internal standard. Dynamic light scattering (DLS) measurements were conducted using Delsa Nano C from Beckman Coulter, Inc. (Fullerton, CA) equipped with a laser diode operating at 658 nm. Size measurements were made in nanopure water. Scattered light was detected at 15° angle and analyzed using a log correlator over 70 accumulations for a 0.5 mL of sample in a glass size cell (0.9 mL capacity). The photomultiplier aperture and the attenuator were automatically adjusted to obtain a photon counting rate of *ca*. 10 kcps. The calculation of the particle size distribution and distribution averages was performed using CONTIN particle size distribution analysis routines using Delsa Nano 2.31 software. The peak average of histograms from intensity, volume and number distributions out of 100 accumulations was reported as the average diameter of the particles, with the standard deviations being calculated as the breadth of the distributions.

Transmission electron microscopy (TEM) bright-field imaging was conducted on a FEI Tecnai G2 F20 FE-TEM, operating at a voltage of 200 kV. The samples were prepared as follows: 4 μL of the dilute solution (with a polymer concentration of *ca.* 0.2 - 0.5 mg/mL) was deposited onto a carbon-coated copper grid, which was pre-treated with plasma to increase the surface hydrophilicity. After 5 min, the excess of the solution was quickly wicked away by a piece of filter paper. The samples were then negatively stained with 4 μL of 1 wt% uranyl acetate aqueous solution. After 1 min, the excess PTA solution was quickly wicked away by a piece of filter paper and the samples were left to dry under ambient conditions overnight. High resolution scanning transmission electron (STEM) microscopy was conducted on a FEI Tecnai G2 F20 FE-TEM coupled with energy dispersive x-ray (EDX), operating at a voltage of 200 kV. The samples were prepared as follows: 4 μL of the dilute solution (with a polymer concentration of *ca.* 0.2 - 0.5 mg/mL) was deposited onto a carbon-coated copper grid, which was pre-treated with plasma to increase the surface hydrophilicity. After 5 min, the excess of the solution was quickly wicked away by a piece of filter paper and the samples were left to dry under ambient conditions overnight.

4.2.3. Experiment procedures

Preparation of silver nitrate-loaded SCK ($AgNO_3$-SCK): A solution of $AgNO_3$ (5.4 mg/mL in nanopure water, 1.18 mL) was added to the SCK solution (15 mL, polymer concentration: 0.274 mg/mL) and the solution was shielded from light and allowed to stir overnight at room temperature. The solution was transferred to a centrifugal filter device (100 kDa MWCO), and washed with nanopure water (> 3 cycles) to remove free silver and other small molecules. Sodium chloride was added to the filtrate until no precipitation was observed to confirm the removal of free silver ion. The resulting $AgNO_3$-SCK was then reconstituted to a final volume of 15.31 mL and silver loading concentration was measured by ICP-MS to be 78 ppm.

Preparation of silver acetate-loaded SCK ($AgCOOCH_3$-SCK): A solution of $AgCOOCH_3$ (3.5 mg/mL in nanopure water, 1.82 mL) was added to the SCK solution (15 mL, polymer concentration: 0.274 mg/mL) and the solution was shielded from light and allowed to stir overnight at room temperature. The solution was transferred to a centrifugal filter device (100 kDa MWCO), and washed with nanopure water (> 3 cycles) to remove free silver and other small molecules. Sodium chloride was added to the filtrate until no precipitation was observed to confirm the removal of free silver ion. The resulting $AgCOOCH_3$-SCK was then reconstituted to a final volume of 15.45 mL and silver loading concentration was measured by ICP-MS to be 123 ppm.

Preparation of SCC10-loaded SCK (SCC10-SCK): A solution of SCC10 (6.3 mg/mL in chloroform 651 μL) was added to the SCK solution (15 mL, polymer concentration: 0.274 mg/mL) and the solution was shielded from light and allowed to stir overnight at room temperature. The solution was transferred to a centrifugal filter device (100 kDa MWCO), and washed with nanopure water (> 3 cycles) to remove free silver and other small molecules. The removal of free silver carbene moieties were confirmed by UV-vis spectroscopy. The resulting SCC10-SCK was then reconstituted to a final volume of 15.63 mL and silver loading concentration was measured by ICP-MS to be 38 ppm.

4.2.4. In vivo experiments

Mice: Male C57BL/6J mice (Jackson Laboratories, Bar Harbor, ME) at 6 - 8 weeks of age were used for these studies that were approved by the University of Texas Southwestern Medical Center IACUC committee. Animals were housed in a barrier facility under pathogen-free conditions until they were inoculated with bacteria.

Drugs and delivery: SCC10-SCK, $AgNO_3$-SCK, $AgCOOCH_3$-SCK, SCC10-$AgNO_3$ SCK, and blank SCK nanoparticle formulations were always suspended in sterile nanopure water free of Cl- ions to avoid the precipitation of AgCl. The nanoparticle formulations were delivered *via* an Aeroneb Lab apparatus (Aerogen Inc., Galway, Ireland) connected to a multi-dosing animal chamber. The Aerogen nebulizer was based on micropump technology that produced fine particles (1-5 µm) in a low velocity aerosol [Geller]. A square Plexiglas box with inner dimensions of 8 x 8 x 4.5 inches served as the multi-dosing chamber. The nebulizer was mounted in the center of the lid.

Infection model and treatment protocol: A clinical isolate of *P. aeruginosa* designated PAM57-15 was provided by Dr. Thomas Ferkol (Washington University, St. Louis, MO). This isolate was a mucoid strain obtained from a patient with cystic fibrosis and has been extensively studied in animal models [van Heeckeren]. The bacteria were streaked from glycerol-frozen stocks onto tryptic soy agar (TSA) plates and incubated overnight at 37 °C. Cells from the fresh plate were suspended in Luria broth (LB, 10 mL) to an OD_{650} of 0.2 and grown at 37 °C in a shaking incubator at 200 rpm to an OD_{650} of 0.4, which corresponded to 3.15×10^8 CFU/mL as determined by serial dilution and plating onto TSA plates. The first infection model experiment was performed to evaluate and compare the efficacy of the core only silver loaded SCK nanoparticles (SCC10-SCK) and the shell only silver loaded SCK nanoparticles ($AgNO_3$-SCK and $AgCOOCH_3$- SCK). Mice were anesthetized using 0.05 ml of intraperitoneally administered ketamine/xylazine cocktail (120 mg/kg ketamine and 16 mg/kg xylazine). Following anesthesia, 75 μL of PAM57-15 inoculum in LB broth was delivered to each mouse intranasally (1.0×10^6 CFU per mouse). Subsequently, the mice were weighed, ear-tagged, and randomly assigned to one of the treatment groups. The treatment groups comprised of sham treatment (90:10 v/v water:phosphate buffer), blank SCK, SCC10-SCK, $AgNO_3$-SCK, and $AgCOOCH_3$- SCK with 5 mice per group. One hour after inoculation with *P. aeruginosa*, the animals were exposed to a single dose of their respective treatments (15 mL administered over 30 minutes). To allow nose-only delivery of drug, animals were placed in CH-247 tubes (CH Technologies, Westwood, NJ). Five animals, each housed in individual tubes, were placed into a multi-dosing chamber at a time. Once the concentration throughout the dosing chamber equilibrated as indicated by diffusion of the mist cloud, the tail movements of the animals were used as an indicator of their status. Mice were weighed and scored daily and observed for a total of 72 h after inoculation for survival.

4.3. Results and discussion

The silver-loaded SCK nanoparticles were constructed from aqueous self assembly of previously reported PAA_{120}-*b*-PS_{40} amphiphilic block copolymers into micelles, followed by covalent crosslinking throughout the shell region to afford discrete, robust shell crosslinked nanostructures. The hydrophobic polystyrene core domain is capable of sequestering hydrophobic molecules, and the hydrophilic poly(acrylic acid) shell allowed for multi-valent functionalization such as crosslinking, complexation with small cationic molecules, or conjugation with chromophores or radiolabels for visualization *in vitro* or tracking *in vivo*. Two procedures were then followed for either shell complexation of silver cation from $AgNO_3$ or $AgCOOCH_3$, or core loading of SCC into the SCKs (Figure 4.1). Silver cation was incorporated into the hydrophilic PAA shell region ($AgNO_3$-SCK, $AgCOOCH_3$-SCK) by addition of $AgNO_3$ or $AgCOOCH_3$ in water into the aqueous SCK solution, followed by stirring overnight to afford a homogeneous solution. SCC10 (silver carbene complex 10, 1-hexyl-3-methyl-4,5-dichloro-imidazole-2-ylidene silver (I) acetate, which undergoes decomposition in the presence of saline solution to release active Ag^+) was encapsulated into the hydrophobic polystyrene core domain and/or the core-shell interface (SCC10-SCK) through addition of SCC10 in chloroform into the aqueous SCK solution, followed by stirring overnight and evaporation of the organic solvent at room temperature overnight. In all three cases, free silver was removed using a centrifugal filter device (100 kDa MWCO). Sodium chloride was added to the filtrate of $AgNO_3$-SCK, $AgCOOCH_3$-SCK until no precipitation was observed to confirm the removal of free silver cation. For

SCC10-SCK, UV-visible spectroscopy was used to confirm removal of free SCC. The resulting silver-loaded SCKs were characterized and their antimicrobial activities were evaluated *in vivo*.

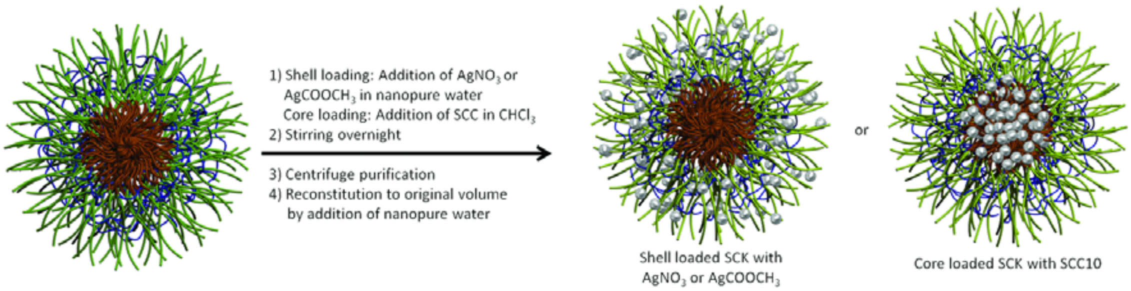

Figure 4.1. Schematic representation of physical encapsulation of $AgNO_3$ or $AgCOOCH_3$ partitioned into the shell of the SCK, and silver carbene complex 10 (SCC10) being incorporated into the core of the SCK.

The dimensions of all silver-loaded SCKs were characterized by transmission electron microscopy (TEM) and dynamic light scattering (DLS) (Table 4.1). As a comparison, empty SCKs without silver were also characterized. The well-defined circularly shaped images observed by TEM suggested that the empty SCKs were spherical with a narrow size distribution of 14 ± 3 nm (Figure 4.2). Silver-loaded SCKs were also spherical with a comparable size distribution of *ca.* 14 ± 3 nm, indicating that the silver incorporation did not affect the size or the shape of the SCKs. Their hydrodynamic diameters, characterized by DLS, were similar across loading methods with narrow number average size distributions of *ca.* 30 ± 8 nm (Figure 4.3).

Table 4.1. Summary of characterization data for empty and silver-loaded SCK nanoparticles by TEM and DLS.

	Diameter by TEM (nm)	D_h (intensity) (nm)	D_h (volume) (nm)	D_h (number) (nm)
Empty SCK	14 ± 3	180 ± 110	50 ± 30	30 ± 8
$AgNO_3$-SCK	14 ± 2	140 ± 90	35 ± 20	24 ± 6
$AgCOOCH_3$-SCK	13 ± 3	150 ± 120	40 ± 20	25 ± 7
SCC10-SCK	15 ± 4	150 ± 120	40 ± 25	28 ± 8

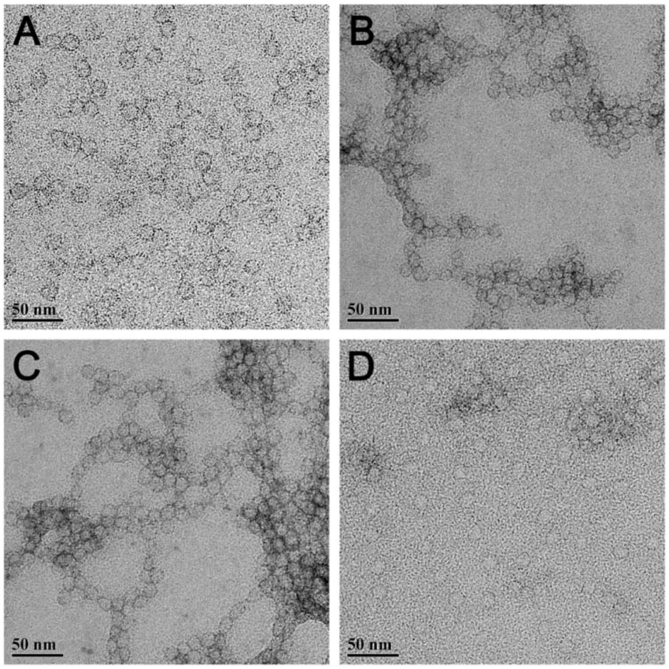

Figure 4.2. TEM images (drop deposited on carbon-coated copper grids and stained negatively with 1% aqueous uranyl acetate) of: A. Empty SCK nanoparticles; B. $AgNO_3$-SCK; C. $AgCOOCH_3$-SCK, and D. SCC10-SCK.

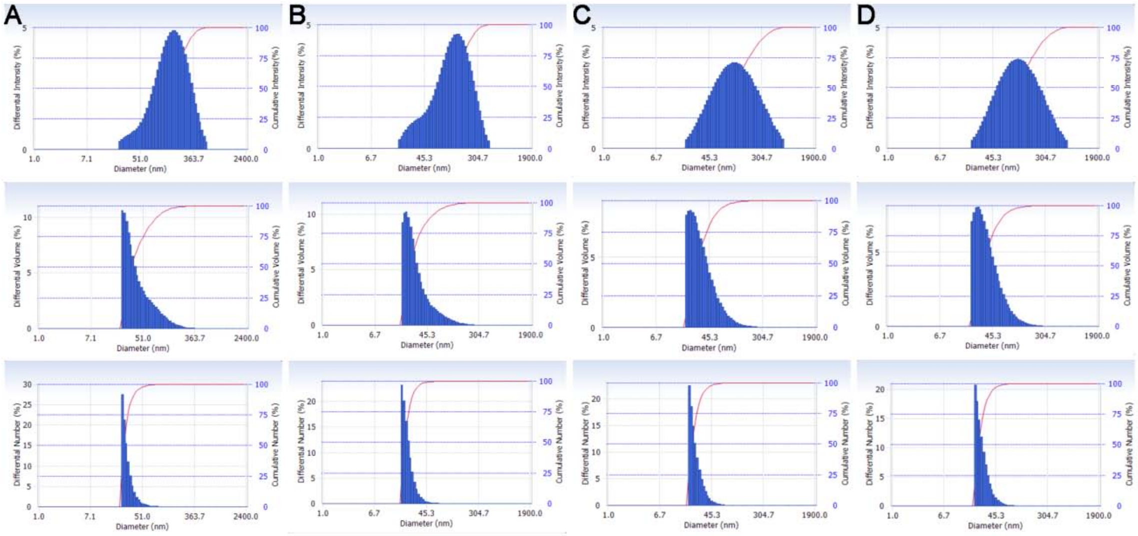

Figure 4.3. DLS histograms of intensity-averaged (first row), volume-averaged (second row), and number-averaged (third row) hydrodynamic diameters (determinations were average values from ten measurements, with the standard deviations being calculated as the breadth of the distributions) of: A. blank SCKs; B. $AgNO_3$-SCK; C $AgCOOCH_3$-SCK, and D. SCC10-SCK.

To understand better where the silver species resided, we performed both dark and bright field scanning transmission electron microscopy (STEM) on unstained $AgNO_3$-SCK and SCC10-SCK. Typically in dark field STEM images, the contrast in unstained samples is especially enhanced when heavy metals like silver are present. The dark field STEM image of $AgNO_3$-SCK (Figure 4.4) showed that the shell of the nanoparticle was more illuminated compared with the core of the nanoparticle due to the silver cation in the shell, strongly supporting our hypothesis that the silver cation from the $AgNO_3$ was more likely to complex with the poly(acrylic acid) residue throughout the shell of the nanoparticles. In the case of SCC10-SCK, the SCC10 was hydrophobic and was more likely to be localized into the core of the nanoparticles and thus core of the nanoparticles was illuminated as demonstrated by STEM images (Figure 4.4). The bright field STEM images also showed the incorporation of the silver species into the nanoparticles.

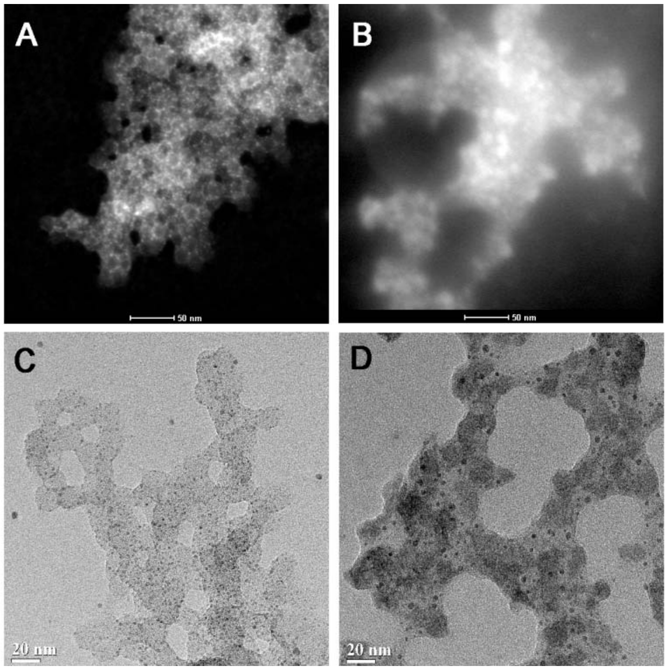

Figure 4.4. STEM dark field images (drop deposited on carbon-coated copper grids with no stain) of A. $AgNO_3$-SCK; B. SCC10-SCK; and STEM bright field images (drop deposited on carbon-coated copper grids with no stain) of C. $AgNO_3$-SCK; D. SCC10-SCK.

Prelimilnary *in vivo* evaulation of the antimicrobial effects of silver-loaded SCK nanoparticles was conducted (in the laboratory of Prof. Carolyn Cannon at University of Texas Southwestern Medical Center, Dallas) to compare the efficacy of the shell only loaded nanoparticles (SCC10-SCK) to the core only loaded nanoparticles ($AgNO_3$-SCK and $AgCOOCH_3$-SCK) using the *P. aeruginosa* murine infection model. Survival rates, weight loss and clinical scores of the animals were monitored and used as quantifiable parameters in the efficacy studies. Blank SCKs and water are used as control treatment groups apart from $AgNO_3$-SCK, $AgCOOCH_3$-SCK, and SCC10-SCK treatment groups. The animals were first inoculized intranasally with *P. aeruginosa* M57-15 strain, and a single dose of nebulized treatment were delivered in a nose-only fashion one-hour post inoculation. The corresponding total dose of silver ions delivered for the SCC10-SCK, $AgNO_3$-SCK, and $AgCOOCH_3$ SCK was 0.57 mg, 1.1 mg, and 1.84 mg Ag^+, respectively. All animal groups lost weight following inoculation and nebulization treatments. However, by 48 hours, the animal group treated with SCC10-SCK had started to show signs of weight gaining for those that had survived (Figure 4.5).

Clinical scores were used to moniter the well being of the mice. Each animal's activity, appearance and posture were recorded every day, with low scores indicating healthy animals (*i.e.* daily movement with smooth fur and normal posture), and high scores indicating sick or moribund mouse (*i.e.* no movement with ruffled fur and prostrate posture) (Figure 4.6). All other treatment group have shown increasingly high average clinical scores, only the clinical score in the SCC-SCK treatment has decreased at 24 h meaning the treatment was effective and the mice were recovering.

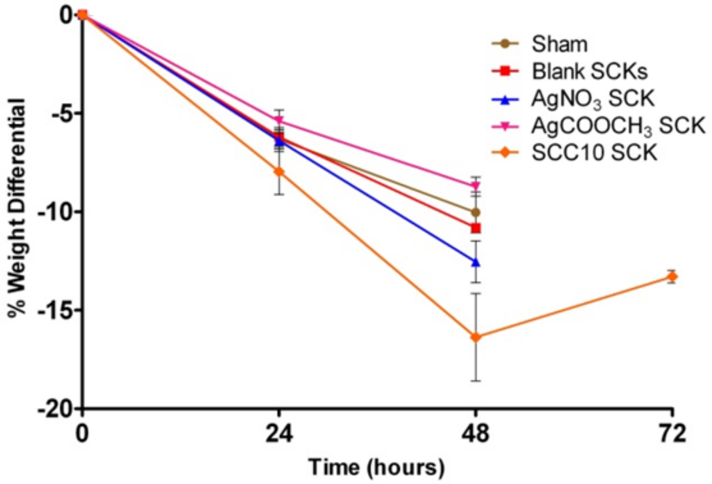

Figure 4.5. Wight loss diagram of mice inoculated with *P. aeruginosa* treated with sham, blank SCK, $AgNO_3$-SCK, $AgCOOCH_3$-SCK and SCC10-SCK treatment groups.

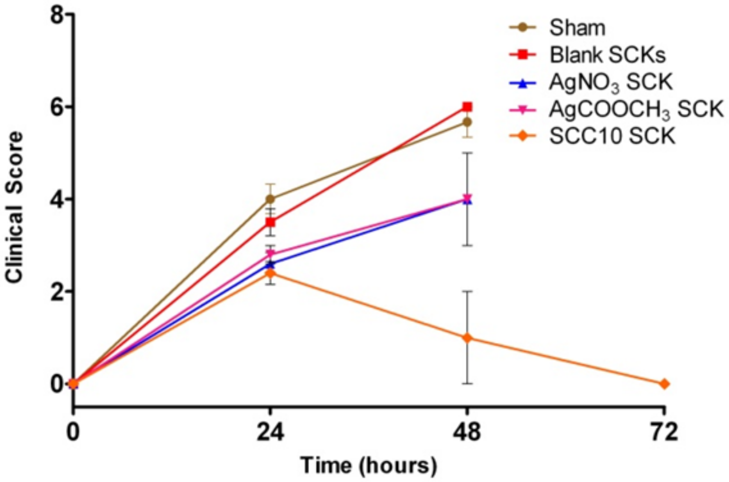

Figure 4.6. Clinical score diagram of mice inoculated with *P. aeruginosa* treated with sham, blank SCK, $AgNO_3$-SCK, $AgCOOCH_3$-SCK and SCC10-SCK treatment groups.

The survival rate was another indication that the SCC10-SCK treatment group had better therapeutic effect than all the other treatment groups. One hundred percent fatality was observed in all other treatment groups except the group treated with SCC10-SCK at approximately 48 hours post-inoculation. Treatment group with SCC10-SCK resulted in a 40% survival advantage (Figure 4.7). The high therapeutic efficacy of SCC10-SCK was unexpected considering the dosage of Ag^+ ions delivered with the $AgNO_3$-SCK and $AgCOOCH_3$-SCK formulations were approximately two- and three-fold higher compared with the Ag^+ dose delivered by SCC10-SCK.

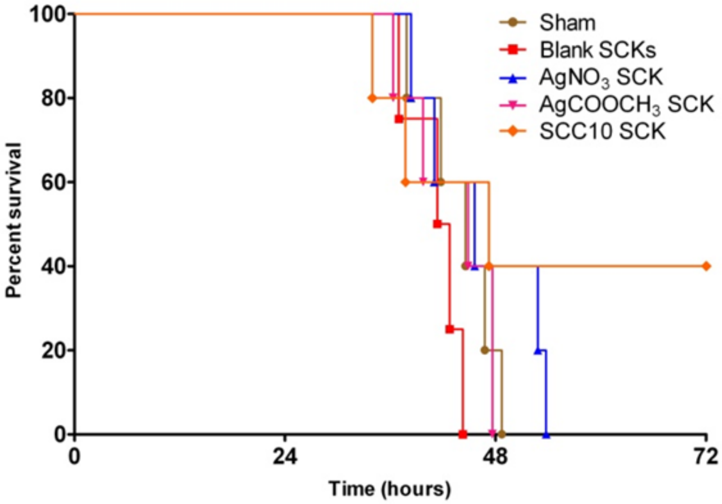

Figure 4.7. Percent survival rate diagram of mice inoculated with *P. aeruginosa* treated with sham, blank SCK, AgNO3-SCK, AgCOOCH3-SCK and SCC10-SCK treatment groups.

4.4. Conclusions

In this study, we have demonstrated that both novel silver carbene complex and silver cation could be encapsulated into multifunctional polymeric nanoparticles. Thses silver-loaded SCKs were able to achieve high therapeutic efficacy *in vivo* with localization of the antimicrobials through nebulization treatment of *P. aeruginosa* inoculated mice. High resolution revealed that SCC and silver cation are partitioned into the core or the shell of the nanoparticles, respectively. However, even at much lower silver concentration, SCC incorporated SCKs were able to demonstrate better therapeutic efficacy than silver cation incorporated SCKs, perhaps due to the slow release of the SCC from the core over a longer period of time.

4.5. Acknowledgements

This material is based upon work supported by the National Heart, Lung and Blood Institute of the National Institutes of Health as a Program of Excellence in Nanotechnology (HHSN268201000046C). This work was also supported by the Welch Foundation through the W. T. Doherty-Welch Chair in Chemistry, Grant No. A-0001

CHAPTER V

SYNTHETIC POLYMER NANOPARTICLES CONJUGATED WITH FIMH$_A$ FROM *E. COLI* PILI TO EMULATE THE BACTERIAL MODE OF EPITHELIAL INTERNALIZATION*

5.1. Introduction

Urinary tract infections (UTI) account annually for approximately 7 million office visits, and 100,000 hospitalizations, and are among the most common bacterial infections in the United States.[132] Almost half of all women will experience an episode of UTI during their lifetime, and 1 in 3 women will require antimicrobial treatment by the age of 24.[133] Although females are more susceptible to UTI than are males, many subpopulations that are also at increased risk include infants and the elderly, as well as patients with diabetes, spinal cord injuries and urologic abnormalities, resulting in economic costs associated with UTI of $2 billion annually, even more than a decade ago.[134,135]

Uropathogenic strains of *Escherichia coli* (UPEC) are the predominant cause of community-onset and healthcare-associated UTI.[136,137] Consequently, understanding the

---

*Reprinted with permission from Lily Yun Lin, Kristin M. Tiemann, Yali Li, Jerome S. Pinkner, Jennifer N. Walker, Scott J. Hultgren, David A. Hunstad and Karen L. Wooley, *J. Am. Soc. Chem.*, **2012**, *134*, 3938-3940. Copyright 2012 American Chemical Society.

compositional and pathogenetic details of UPEC is important for the development of therapeutic systems. UPEC's ability to attach to superficial epithelial cells of the bladder is mediated by heteropolymeric surface fibers called type 1 pili. Type 1 pili consist of a thick pilus rod composed of a helical polymer of the major subunit FimA; plus a thin, flexible tip fibrillum comprised of the adapter FimF, fibrillar subunit FimG and tip adhesin FimH.[138] The terminal, adhesive domain of FimH (denoted FimH_A) allows the pathogen to bind mannose moieties decorating the centers of the 16-nm uroplakin complexes found on the luminal surface of bladder epithelial cells.[139-141] Earlier work has shown that type 1 pili are necessary and sufficient to mediate internalization of UPEC into bladder epithelial cells,[142] and this activity is conferred by the mannose binding pocket within the FimH adhesin domain.[143,144] Internalized bacteria can replicate within the epithelial cell cytoplasm to form biofilm-like communities,[145] and later establish a quiescent reservoir within bladder epithelium that avoids immune detection and might later re-emerge to cause recurrent UTI.[144,145]

Our primary interest is to develop nanoparticle carriers that bind and enter bladder epithelial cells to deliver antimicrobial agents directly to the niche occupied by these harbored bacteria. In this study, therefore, we have designed multifunctional shell-crosslinked knedel-like nanoparticles (SCKs) that can be conjugated with FimH_A for bladder epithelial cell binding and internalization, for the purpose of targeted delivery of various antimicrobial agents for the treatment and prevention of UTIs. The SCKs were constructed from aqueous assembly of poly(acrylic acid)-*block*-polystyrene block copolymers, (PAA-*b*-PS) into micelles, followed by covalent crosslinking throughout the shell region to afford discrete, robust shell crosslinked nanostructures. The amphiphilic core-shell morphology provides opportunities to partition the various functions of therapeutic packaging,[39,131] cell targeting, and imaging within different regions of the nanoparticle framework.[146] In this study, the residual reactive acrylic acid residues on the surfaces and throughout the shell layers of the SCKs were utilized for amidation with native lysines of $\mathrm{FimH_A}$ to conjugate the adhesin and promote epithelial cell targeting and internalization, and with the amine terminus of the fluorescein-based dye, 5-((5-aminopentyl)thioureidyl)fluorescein (FITC cadaverine) to permit fluorescence microscopic imaging (Figure 5.1).

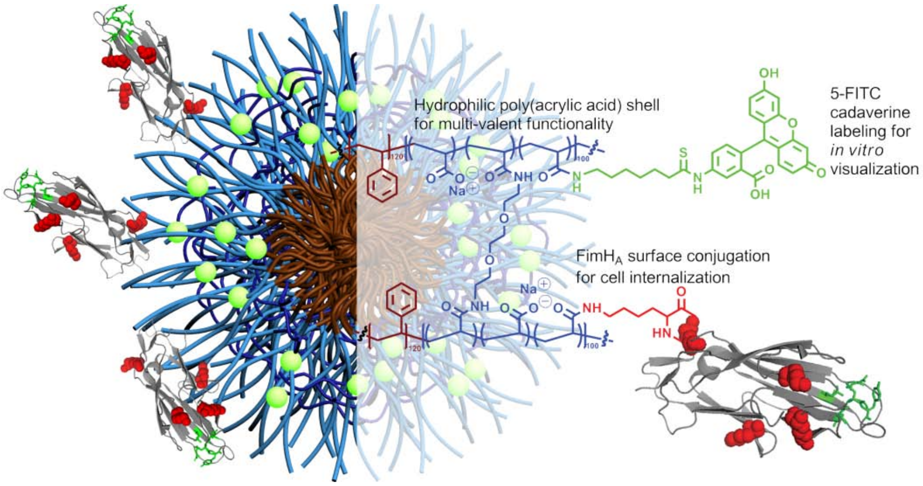

Figure 5.1. Schematic and chemical representation of $\mathrm{FimH_A}$-functionalized and FITC cadaverine-labeled SCK nanoparticles.

5.2. Materials and methods

5.2.1. Materials

All reagents were purchased from Sigma-Aldrich (St. Louis, MO) and used as received unless otherwise indicated. PAA_{120}-*b*-PS_{100} (Mn^{NMR} = 19,500 Da, PDI = 1.1, from $PtBA_{120}$-*b*-PS_{100} precursor) polymer precursor was synthesized as previously reported. 5-((5-aminopentyl)thioureidyl)fluorescein, dihydrobromide salt (5-FITC cadaverine) (Invitrogen, Carlsbad, CA) and sulfonated *N*-hydroxysuccinimide (Sulfo-NHS) (Thermo Scientific, Waltham, MA) were used as received. Spectra/Por membrane tubes purchased from Spectrum Laboratory Inc. (Rancho Dominguez, CA) were used for dialysis. Amicon® ultra centrifugal filter devices (100 kDa MWCO) were purchased from Millipore (Bedford, MA). Nanopure water (18 MΩ•cm) was acquired by means of a Milli-Q water filtration system (Millipore, Billerica, MA).

5.2.2. Instruments

UV-Vis spectra were collected at 37 °C in the region of 200 - 800 nm, using a Varian Cary 100 Bio UV-visible spectrophotometer. Dynamic light scattering measurements were conducted with a Brookhaven Instruments (Holtsville, NY) DLS system equipped with a model BI-200SM goniometer, BI-9000AT digital correlator, a model EMI-9865 photomultiplier, and an Innova 300 Argon laser operated at 514.5 nm (Coherent Inc., Santa Clara, CA). Measurements were made at 25 ± 1 °C. Prior to analysis, solutions were filtered through a 0.45 μm Millex®-GV PVDF membrane filter (Millipore, Medford, MA) to remove dust particles. Scattered light was collected at a fixed angle of 90°. The digital correlator was operated with 522 ratio spaced channels, and initial delay of 5 μs, a final delay of 50 ms, and a duration of 8 min. A photomultiplier aperture of 400 μm was used, and incident laser intensity was adjusted to obtain photon counting between 200 and 300 kcps. Calculations of particle size distributions and distribution averages were performed with the ISDA software package (Brookhaven Instruments), which employed single-exponential fitting, Cumulants analysis, and CONTIN particle size distribution analysis routines. All determinations were average values from ten measurements, with the standard deviations being calculated as the breadth of the distributions. Transmission electron microscopy (TEM) bright-field imaging was conducted on a Hitachi H-7500 microscope, operating at 80 kV. Immunogold EM samples were viewed on a JEOL 1200EX II microscope (JEOL USA, Peabody, MA). Fluorescent and confocal images were collected with an LSM510 fluorescent confocal microscope (Carl Zeiss Inc., Thornwood, NY).

5.2.3. Experiment procedures

General procedure for the preparation of the micelles and SCKs: PAA_{120}-*b*-PS_{100} block copolymer precursor (*ca*. 50 mg) was dissolved in THF (50 mL) in a 250-mL round bottom flask and allowed to stir for 30 min at room temperature. To this solution, an equal volume of nanopure water was added dropwise *via* a syringe pump over a period of 3 h. The reaction mixture was allowed to stir for an additional 24 h at room temperature and dialyzed against nanopure water for 4 d in presoaked dialysis tubing (MWCO *ca*. 6 - 8 kDa) to afford a micelle solution with a final polymer concentration of *ca*. 0.25 mg/mL. To the micelle solution of PAA_{120}-*b*-PS_{100} was added a solution of 2,2′-(ethylenedioxy)bis(ethylamine) (EDDA) in nanopure water (*ca*. 15 mg/mL, 1.1 eq, nominal 20% crosslinking) dropwise. To this solution, 1-[3'-(dimethylamino)propyl]-3-ethylcarbodiimide methiodide (EDCI) in nanopure water (*ca*. 14 mg/mL, 1.4 eq) was added dropwise *via* a syringe pump over 20 min, and the resulting mixture was allowed to stir overnight before dialysis against nanopure water for 4 d in presoaked dialysis tubing (MWCO.*ca*. 6 - 8 kDa) to afford SCK solutions with a final polymer concentration of *ca*. 0.25 mg/mL. Samples for TEM were prepared as follows: 4 μL of the SCK solution (with a polymer concentration of *ca.* 0.25 mg/mL) was deposited onto a carbon-coated copper grid, which was pre-treated with absolute ethanol to increase the surface hydrophilicity. After 5 min, the excess of the solution was quickly wicked away by a piece of filter paper. The samples were then negatively stained with 4 μL of 1 wt% phosphotungstic acid (PTA) aqueous solution. After 1 min, the excess PTA solution was quickly wicked away by a piece of filter paper and the samples were left to dry under ambient conditions overnight. Diameter (TEM) = 18 ± 2 nm, $D_{h(intensity)}$ = 100 ± 30 nm, $D_{h(volume)}$ = 70 ± 20 nm, $D_{h(number)}$ = 40 ± 10 nm.

Preparation of 5-FITC cadaverine-labeled SCKs: A solution of EDCI in nanopure water (1.8 mg, 18 mg/mL, 30 eq., 6 μmol) was added dropwise over five minutes to a solution of SCK in nanopure water (15 mL, 0.25 mg/mL polymer concentration). The reaction mixture was stirred for 30 min at room temperature. To this solution, a solution of 5-FITC cadaverine in nanopure water (0.6 mg, 1.8 mg/mL, 1.1 μmol) was added dropwise over 2 min. The reaction was allowed to proceed for 24 h at room temperature before being transferred to presoaked dialysis tubing (MWCO *ca*. 6 - 8 kDa), then dialyzed against nanopure water for 4 d to remove unconjugated chromophores and other impurities, yielding a 5-FITC cadaverine-labeled SCK solution with a final concentration of *ca.* 0.21 mg/mL.

Conjugation of FimH$_A$ to 5-FITC cadaverine-labeled SCKs: A solution of 5-FITC cadaverine-labeled SCKs (3 mL, 0.21 mg/mL polymer concentration) was cooled to 4 °C while the pH of the solution was adjusted to *ca.* 5 - 6 with the dropwise addition of 0.1 N acetic acid. Sulfo-NHS (*ca.* 1 mg, 12 mg/mL, 4.4 µmol, 1.2 eq.) and EDCI (*ca.* 1.3 mg, 13 mg/mL, 4.4 µmol, 1.2 eq.) were added to the SCK solution and the reaction mixture was allowed to stir at 4 °C for another 30 minutes. The solution pH was then adjusted to 7 - 8 with dropwise addition of saturated sodium phosphate followed by addition of FimH$_A$ in phosphate buffer saline (PBS) (optimal results obtained with 2.0 mL, 0.65 mg/mL, 0.080 µmol). The reaction was allowed to proceed at 4 °C and slowly warmed to room temperature over 24 h. Unconjugated FimH$_A$ and other impurities were removed by extensive washing using a centrifugal filtration device (MWCO 100 kDa) with PBS (pH 7.4, 5 mM), and the final volume was reconstituted to 5 mL with PBS to give a FimH$_A$-conjugated, 5-FITC cadaverine-labeled SCK solution (final polymer concentration *ca.* 0.13 mg/mL, 5-FITC cadaverine concentration 0.033 mg/mL, *ca.* 5 dyes per particle; calculated by UV-vis spectroscopy using the extinction coefficient of 5-FITC cadaverine at pH 7, $\varepsilon = 82000 \pm 6000$ L/mol·cm). Diameter (TEM) = 20 ± 3 nm, $D_{h(intensity)} = 80 \pm 30$ nm, $D_{h(volume)} = 50 \pm 20$ nm, $D_{h(number)} = 40 \pm 10$ nm.

Immunogold electron microscopy: FimH$_A$-conjugated and naked SCKs were allowed to adsorb onto glow discharged, formvar/carbon-coated copper grids for 10 min. The grids were washed twice with PBS, blocked with 1% fetal bovine serum (FBS) for 5 min, and subsequently incubated with rabbit anti-FimH antibody for 20 min at room temperature. A set of comparator SCK-FimH$_A$ grids received no primary antibody. Grids were again washed twice with PBS, blocked with 1% FBS for 5 min, and incubated with 12-nm colloidal gold-conjugated anti-rabbit IgG (Jackson ImmunoResearch Laboratories, Inc., West Grove, PA) for 20 min at room temperature. Following three washes with distilled H_2O, the grids were stained with 1% aqueous uranyl acetate (Ted Pella Inc., Redding, CA) for 1 min. Excess liquid was gently wicked off and the grids were allowed to air dry. Ten random frames were captured for each experimental condition, and *ca*. 500 SCKs per condition were assessed for immunogold labeling.

Fluorescence and confocal microscopy: For fluorescence microscopy, 5637 bladder epithelial cells (American Type Culture Collection HTB-9, Manassas, VA) were grown to sub-confluence on sterile glass coverslips in RPMI 1640 medium with 10% FBS. On the day of experiment, cells were washed with PBS, inoculated with SCK solution as described above, and incubated for 1 h at 37 °C. After additional washing, cells were fixed with 3% paraformaldehyde (PFA) (Electron Microscopy Sciences, Hatfield, PA) for 10 min, then stained with 1:1000 AlexaFluor 594-conjugated wheat germ agglutinin (WGA) (Molecular Probes). For confocal microscopy, after SCK inoculation as above, cells were liberated by application of 0.05% trypsin-0.02% EDTA for 15 min, collected by gentle centrifugation, and fixed with 3% PFA for 10 min. Subsequently, cell suspensions were washed 3 times with PBS, then stained by resuspending in PBS with

1:1000 AlexaFluor 594-conjugated WGA. After a final PBS wash, cells were applied to poly-L-lysine coated slides by cytocentrifugation before microscopy.

5.3. Results and discussion

The multi-functional SCK nanoparticles were prepared from previously reported PAA_{120}-*b*-PS_{100} amphiphilic block copolymers, through aqueous micellization and further covalent crosslinking and chemical modification reactions.[39] Water (a selective solvent for the PAA block segment) was introduced to a THF (a good solvent for both PAA and PS) solution of the block copolymer dropwise *via* a syringe pump to form discrete spherical micelles. The PAA shell regions of these micelles were then crosslinked *via* amidation chemistry with 2,2′-(ethylenedioxy)bis(ethylamine) (EDDA), as a diamine crosslinker, in the presence of 1-[3′-(dimethylamino)propyl]-3-ethylcarbodiimide methiodide (EDCI) to afford SCK nanoparticles. 5-FITC cadaverine was attached through additional amidation chemistry using the coupling agent EDCI, rendering the SCKs fluorescent, to facilitate *in vitro* tracking of SCKs during functional studies (Figure 5.2A). The conjugation of the targeting ligand $FimH_A$ was then accomplished by non-selective reaction between any of the four lysine residues on $FimH_A$ and residual carboxylic acids on the SCK surface, following a previously established method.[147] The reaction was carried out by first lowering the pH of the SCK solution in nanopure water to 5 with acetic acid and incubating at 4 °C for 30 minutes. Addition of sulfonated *N*-hydroxysuccinimide and coupling agent EDCI followed, and the reaction mixture was then allowed to stir at 4 °C for another 30 minutes before the pH of the solution was adjusted to 7-8 by addition of sodium phosphate. $\mathrm{FimH_A}$ (0.65 mg/mL in PBS, pH 7.4) was added to the reaction solution slowly, and the conjugation process was allowed to proceed for 24 h at 4 °C. Purification by extensive washing using a centrifugal filtration device (MWCO 100 kDa) with PBS solution was performed to remove $\mathrm{FimH_A}$ that was not associated with the nanoparticles. Including lower concentrations of $\mathrm{FimH_A}$ gave less efficient functionalization, as judged by the analytical methods detailed below. The final products were characterized physicochemically to determine their sizes, compositions and structures, and the effects of $\mathrm{FimH_A}$ conjugation on their biological behaviors were evaluated.

The dimensions of the 5-FITC cadaverine-labeled and FimHA-functionalized SCK nanoparticles were characterized by transmission electron microscopy (TEM) and dynamic light scattering (DLS) (Figure 5.2B). The circularly-shaped images observed by TEM suggested that these nanoparticles were spherical with a narrow size distribution of 20 ± 3 nm. The number average hydrodynamic diameter of SCK nanoparticles was determined to be 40 ± 10 nm by DLS.

$\mathrm{FimH_A}$ functionalization efficiency in a biologically active form was determined by immunogold electron microscopy (EM), using primary rabbit anti-FimHA secondary anti-rabbit IgG conjugated to 6-nm gold particles. The SCK nanoparticles were readily visualized by EM, and gold particle labeling of $\mathrm{FimH_A}$-SCKs (33%) was significantly higher than that of naked SCKs (5.6%) or of $\mathrm{FimH_A}$-SCKs omitting primary antibody (8.8%; $p<0.005$ for both comparisons; Figure 5.3). Since the efficiency of the immunolabeling process was not precisely known, we concluded that the conjugation process accomplished FimH$_A$ attachment to a minimum of 1/3 of SCKs.

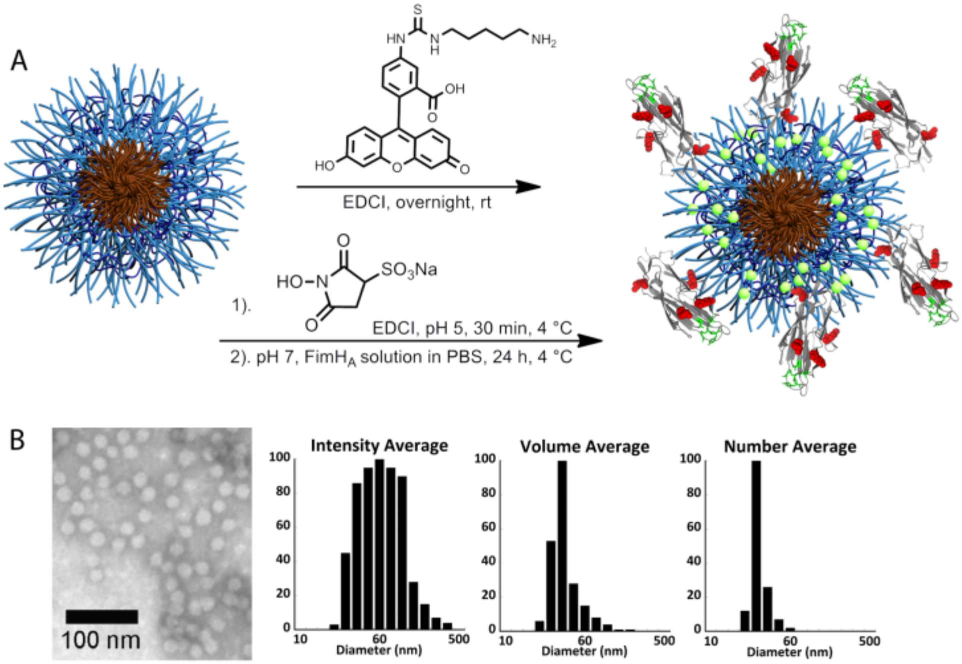

Figure 5.2. A. Schematic representation of 5-FITC cadaverine labeling and FimH$_A$ conjugation to the shell of SCK nanoparticles *via* amidation chemistry; B. TEM and DLS characterization of 5-FITC cadaverine-tagged, FimH$_A$-conjugated SCK nanoparticles. Diameter (TEM) = 20 ± 3 nm, $D_{h(intensity)}$ = 80 ± 30 nm, $D_{h(volume)}$ = 50 ± 20 nm, $D_{h(number)}$ = 40 ± 10 nm.

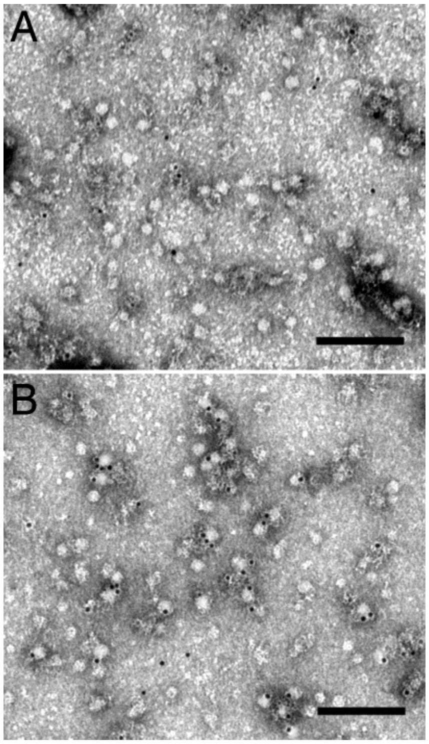

Figure 5.3. Functionalization of $\mathrm{FimH_A}$ onto SCK surfaces. Naked SCKs (A) and FimHA-functionalized SCKs (B) viewed by immunogold transmission EM after incubation with rabbit anti-$\mathrm{FimH_A}$ antibody and gold-conjugated anti-rabbit IgG. Labeling of $\mathrm{FimH_A}$-SCKs was significantly greater than that of naked SCKs; representative images are shown. Scale bars, 100 nm.

We next demonstrated FimH_A-SCK-specific binding to cultured bladder epithelial cells. We then assessed epithelial cell binding and internalization by fluorescent confocal microscopy. Cells were grown to sub-confluence on sterile glass coverslips, overlaid with 5-FITC cadaverine-labeled-, naked- or FimH_A-SCKs, washed and stained with AlexaFluor 594-conjugated wheat germ to visualize the cell surfaces. By fluorescence microscopy the association of SCKs with the cell surfaces was shown to be dose dependent, FimH_A specific, and inhibited by addition of mannose to the medium (Figure 5.4). Confocal analysis demonstrated several examples of internalized SCKs (Figure 5.5), though the majority of particles were localized to the cell surfaces, and internalized SCKs were only occasionally observed.

We then prepared samples by incubating FimH_A protein and nanoparticles in the absence *vs*. presence of the amidation coupling agents to evaluate the relative amount of FimH_A that was physically associated *vs*. covalently conjugated with the SCKs, respectively. More free protein (non-covalently attached) was observed in samples that lacked the coupling agents; however, even the samples that had undergone the complete conjugation conditions contained a minor amount of free protein or protein that was strongly but noncovalently (perhaps electrostatically) associated with the SCKs. On sodium dodecyl sulfate (SDS) gels, the nanoparticles remained mostly in the sample wells but a portion entered the stacking gel (5% acrylamide) and stopped at the interface of the resolving gel (12% acrylamide). By Western blot, FimH_A was co-localized with the FITC signal arising from SCKs in sample wells and at the gel interface. This co-localized signal indicates covalent, detergent-resistant SCK-FimH_A association, although the final functionalized SCKs, even with centrifugal filtration, existed as a mixture of physically- and covalently-associated protein and nanoparticle.

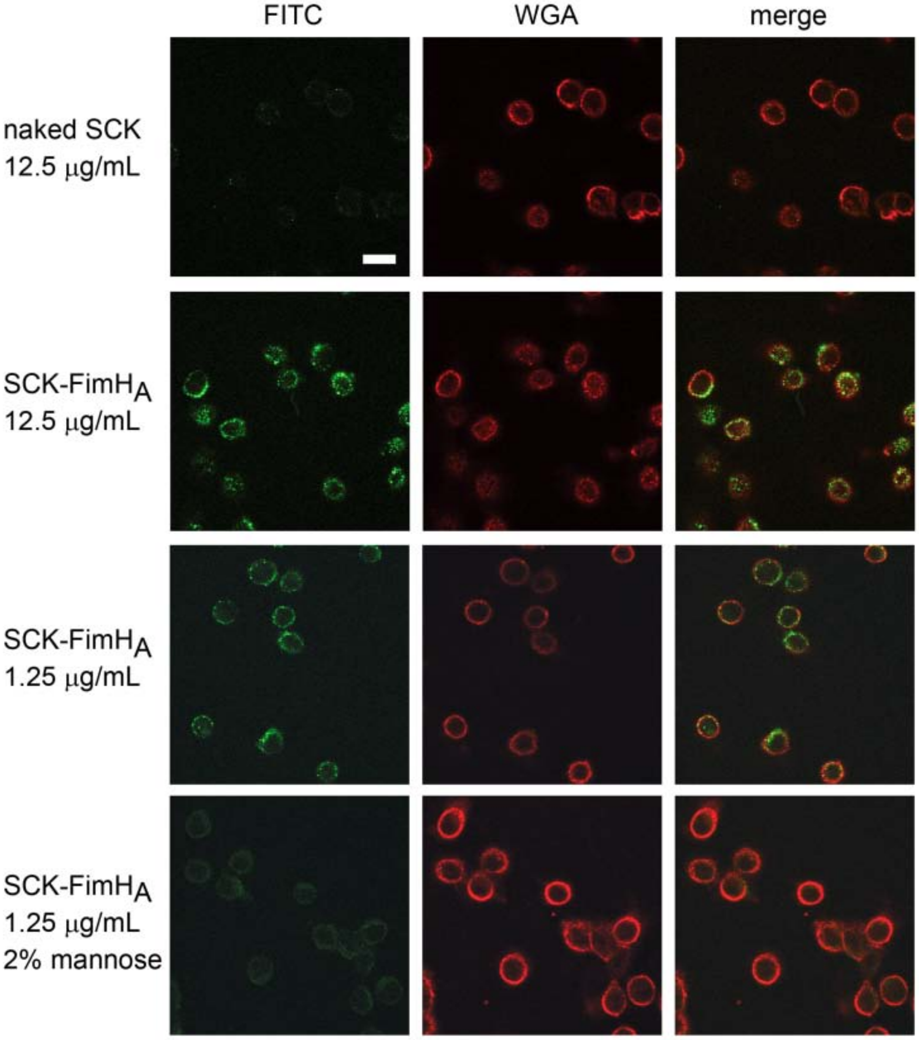

Figure 5.4. Binding of FimH$_A$-SCK nanoparticles to cultured bladder epithelial cells. Monolayers of 5637 cells were treated with the indicated doses of 5-FITC cadaverine-tagged (green) SCKs, naked or conjugated with FimH$_A$, and with or without 2% mannose. Cells were liberated from the surface and stained circumferentially with AlexaFluor 594-conjugated wheat germ agglutinin (WGA; red). Scale bar (upper left panel), 20 μm.

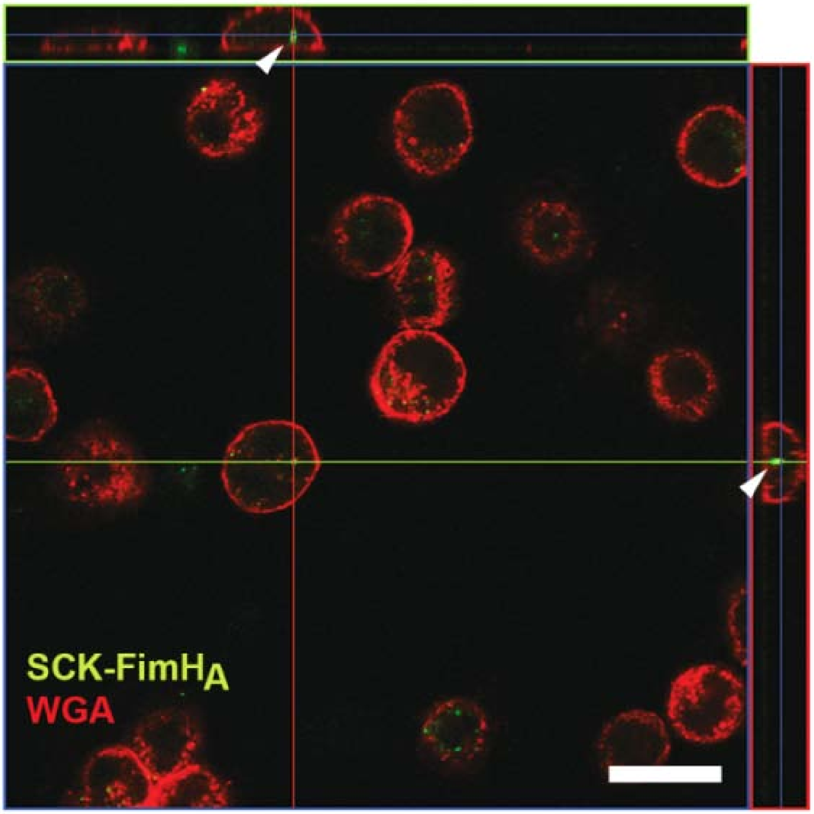

Figure 5.5. Epithelial cell internalization of FimH$_A$-SCKs. In this example of an internalized particle, the SCK of interest is viewed at the cross-hairs in the XY plane; orthogonal views (top and right of the panel) show the particle encircled by the red cell-surface stain (arrowheads). Scale bar, 20 µm.

5.4. Conclusions

We have demonstrated the feasibility of leveraging a known bacterial-host interaction to direct nanostructures to an epithelial cell surface for potential therapeutic use. We recognize a number of opportunities for our ongoing work to optimize facets of our synthetic scheme: increasing FimH$_A$ density on the SCK surface (with full covalent attachment), improving the orientation of conjugated FimH$_A$ (*i.e.*, altering lysine content to make the mannose binding pocket consistently available upon NP conjugation), and promoting increased internalization of SCKs into epithelial cells (*e.g.*, by varying the size and shape of the functionalized SCKs).[148,149] $FimH_A$ is readily amenable to genetic engineering approaches to optimize these parameters and to study the efficiency of alternative conjugation chemistries, and the conservation of mannose-binding capacity in engineered $FimH_A$ variants can be confirmed by readily available methods. Aside from the primary therapeutic aim, an antimicrobial-bearing SCK that would coat the luminal surface of the bladder would also be of interest for prophylaxis against UTI in special populations (those with indwelling catheters, who intermittently catheterize, or who are undergoing cystoscopy or other procedures). Upon identification of a lead $FimH_A$ construct, we will employ a murine model of cystitis to begin studying *in vivo* activities.[150]

An array of antimicrobials might be considered for loading into the functionalized SCKs described here, but silver is an attractive potential cargo,[121-123,151] as it may be loaded in cationic form or incorporated into hydrophobic organometallic compounds and might be effective against reservoir bacteria that appear metabolically quiescent. In fact, our previous work demonstrated loading and release of cationic and organometallic silver with SCKs, as well as antimicrobial activity of these silver-loaded systems against both *E. coli* and *Pseudomonas aeruginosa* at physiologically relevant concentrations.

Finally, functionalized SCKs targeting bladder epithelial cells might be employed in antigen delivery for epithelial vaccines. FimH itself has been studied as a component of candidate vaccines against UTI,[152-154] but results so far have not translated into human efficacy. However, if alternative antigens and adjuvants that induce protective antibody and/or T-cell responses are identified, these could be adapted for presentation alongside $\mathrm{FimH_A}$ on the SCK shell, where epithelial adhesion would promote prolonged antigen exposure in the urinary tract.

5.5. Acknowledgments

We thank W. Beatty for technical imaging expertise. This project has been funded by the National Institute of Diabetes and Digestive and Kidney Diseases of the National Institutes of Health (R01-DK082546), by a March of Dimes Basil O’Connor Award (5-FY09-105), and by the Welch Foundation through the W. T. Doherty-Welch Chair in Chemistry, Grant No. A-0001.

CHAPTER VI

MORPHOLOGICAL EVOLUTION OF A TRIBLOCK COPOLYMER AND CHEMICAL MANIPULATIONS THEREOF

6.1. Introduction

The self assembly of amphiphilic block copolymer into nanoscale objects with complex morphology that have potential biomedical application in the field of nanomedicine is an ever expanding field.[2,3,38,155-157] In recent years, multicompartment micelles (MCMs), which are supramolecular assemblies resulting from phase-segregated block copolymers have attracted significant attention.[158,159] The miktoarm star copolymers are particularly suitable for the formation of MCMs,[158,160-171] however, the self assembly of linear triblock copolymers into MCMs is also being explored.[119,159,172-178] Both the miktoarm star copolymer and linear triblock copolymer consisted of a hydrophilic block segment and two incompatible hydrophobic block segments that are favourable for the formation of MCMs through compartmentalization of the two incompatible blocks during aqueous assembly.

In our previous studies, we have shown self assembly of a linear triblock copolymer composed of hydrophilic ethylene oxide segment for water dispersibility, hydrophobic *N*-acryloxysuccinimide for functionalization and hydrophobic styrene blocks for nucleation into micellar assemblies (PEO-*b*-PNAS-*b*-PS).[95] We have demonstrated the manipulation of the size and number of internal compartments of the assembled MCMs through the hydrolysis of the PNAS domain, and their pH-responsive photophysical properties through functionalization with a pyrazine dye-based crosslinker. Similarly, a diblock copolymer, poly(acrylic acid)-*b*-poly(*p*-hydroxystyrene) (PAA-*b*-P*p*HS), has been shown to access both spherical and cylindrical morphologies, whose unique chemical environments were probed through shell crosslinking chemistry.[93] In this study, with the incorporation of an active ester functionality for facile chemical manipulations,[16,179] the construction of both cylindrical and multicompartment nanostructure with a single type of linear triblock copolymer, PEO_{45}-*b*-$PNAS_{66}$-*b*-PS_{30} was achieved, and their dynamic disembodiment into individual spherical nanoparticles and retention of morphology through shell crosslinking were observed. (Figure 6.1).

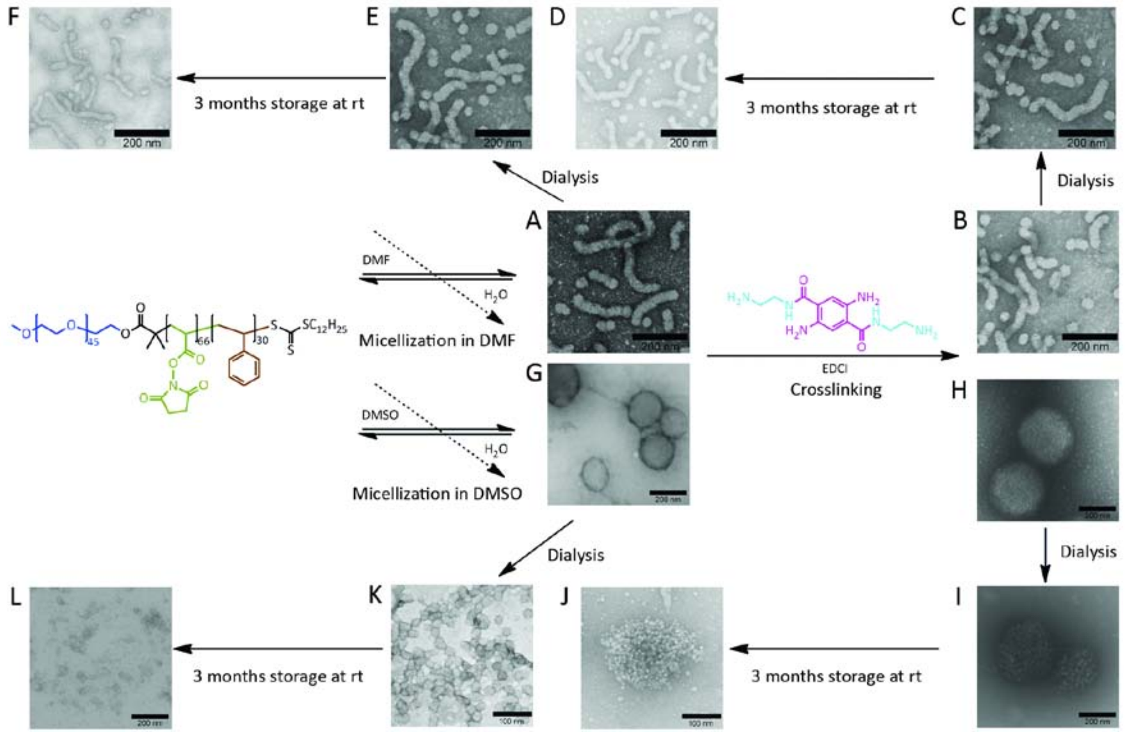

Figure 6.1. Schematic representation of self assembly of PEO$_{45}$-*b*-PNAS$_{66}$-*b*-PS$_{30}$ to form both cylindrical nanostructure and multicompartment nanostructure: A. micellization in DMF to form cylindrical micelles; B. crosslinking with pyrazine crosslinker to form shell crosslinked cylindrical nanostructures (SCCN); C. SCCN after dialysis for 3 days; D. SCCN after 3 months storage at room temperature; E. cylindrical micelles after dialysis for 3 days; F. cylindrical micelles after 3 month storage at room temperature; G. micellization in DMSO to form multicompartment micelles (MCM); H. crosslinking with pyrazine crosslinker to form shell crosslinked multicompartment nanostructure (MCN); I. MCN after dialysis for 3 days; J. MCN after 3 months storage at room temperature. K. MCM dissasembled into individual micelles upon dialysis; L. individual micelles disassembled from MCM are stable after 3 months storage at room temperature.

6.2. Materials and methods

6.2.1. Materials

The mono-methoxy terminated mono-hydroxy poly(ethylene glycol) (mPEG2k, *MW* = 2,000 Da, *PDI* = 1.06) was purchased from Intezyne Technologies and was used for the synthesis of macro-CTA without further purification. The PEO-*b*-PNAS-*b*-PS triblock copolymer (*vide infra*) and the crosslinkers were synthesized according to previous reports. All other chemicals were purchased from Aldrich Chemical Co. (St. Louis, MO) and used without further purification unless otherwise noted. The Supor 25 mm 0.1 μm Spectra/Por Membrane tubes (MWCO 6-8 kDa), used for dialysis, were purchased from Spectrum Medical Industries Inc. Nanopure water (18 MΩ•cm) was acquired by means of a Milli-Q water filtration system, Millipore Corp. (Bedford, MA).

6.2.2. Instruments

The molecular weight distribution was determined by Gel Permeation Chromatography (GPC). The *N*,*N*-dimethylformamide (DMF) GPC was conducted on a Waters Chromatography Inc. (Milford, MA) system equipped with an isocratic pump model 1515, a differential refractometer model 2414, and a two-column set of Styragel HR 4 and HR 4E 5 μm DMF 7.8×300 mm columns. The system was equilibrated at 70 °C in pre-filtered DMF containing 0.05 M LiBr, which served as polymer solvent and eluent (flow rate set to 1.00 mL/min). Polymer solutions were prepared at a concentration of ca. 3 mg/mL and an injection volume of 200 μL was used. Data collection and analysis was performed with Empower Pro software (Waters Inc.). The system was calibrated with poly(ethylene glycol) standards (Polymer Laboratories) ranging from 615 to 442,800 Da.

IR spectra were recorded on an IR Prestige 21 system (Shimadzu Corp.) and analyzed by using the IRsolution software. Dynamic light scattering (DLS) measurements were conducted using Delsa Nano C from Beckman Coulter, Inc. (Fullerton, CA) equipped with a laser diode operating at 658 nm. Size measurements were made in nanopure water. Scattered light was detected at 15° angle and analyzed using a log correlator over 70 accumulations for a 0.5 mL of sample in a glass size cell (0.9 mL capacity). The photomultiplier aperture and the attenuator were automatically adjusted to obtain a photon counting rate of ca. 10 kcps. The calculation of the particle size distribution and distribution averages was performed using CONTIN particle size distribution analysis routines using Delsa Nano 2.31 software. The peak average of histograms from intensity, volume and number distributions out of 100 accumulations were reported as the average diameter of the particles, with the standard deviations being calculated as the breadth of the distributions.

Transmission electron microscopy (TEM) bright-field imaging was conducted on a JOEL 1200 microscope, operating at 100 kV. The samples were prepared as follows: 4 μL of the dilute solution (with a polymer concentration of ca. 0.2 - 0.5 mg/mL) was deposited onto a carbon-coated copper grid, which was glow charged to increase the surface hydrophilicity. After 5 min, the excess of the solution was quickly wicked away by a piece of filter paper. The samples were then negatively stained with 4 μL of 1 wt% uranyl acetate aqueous solution. After 1 min, the excess uranyl acetate solution was quickly wicked away by a piece of filter paper and the samples were left to dry under ambient conditions overnight.

6.2.3. Experiment procedures

Synthesis of mPEG$_{2k}$ macro CTA: To a solution of mPEG$_{2k}$ (3.028 g, 1.5 mmol, 1 eq.) in CH_2Cl_2 (30 mL) was added DDMAT (1.940 g, 5.3 mmol, 1.5 eq.) and dicyclohexylcarbodiimide (0.464 g, 2.3 mmol, 1.5 eq.). The reaction was allowed to stir for 10 min at room temperature before 4-di(methylamino)pyridine (0.055 g, 0.45 mmol, 0.3 eq.) was added to the reaction mixture and was allow to stir for 20 h at room temperature. The reaction mixture was filtered and the filtrate was place at 4 °C overnight and filtered again and concentrated to *ca*. 10 mL before precipitated into 250 mL ether twice. The crude produce was purified further by column chromatography (2 - 3% MeOH/CH_2Cl_2) to afford mPEG2k-CTA as a yellow solid product (2.035 g, 62% yield).

Synthesis of NAS monomer: To a 100 mL round bottom flask, *N*-Hydroxysuccinimide (NHS, 10.4 g, 90.4 mmol) was dissolved in $CHCl_3$ (75 mL). The solution appeared to be cloudy and remained cloudy after the addition of triethylamine (TEA, 10.0 g, 99.4 mmol). Acryol chloride (9.03 g, 99.4 mmol) was added dropwise, the solution became yellowish clear color and allowed to stir in ice/water bath for approximately 30 min, right before white cloudy precipitants appeared. The reaction mixture was washed with nanopure water(50 mL x 3) and brine (50 mL x 2), and the organic layer was dried with $MgSO_4$, and concentrated by rotovap to yield white powdery product. The product was recrystallized with ethyl acetate and pentane and left in the fridge over night to yield 8.0365 g of white crystal product (53% yield). ^{1}H NMR (300 MHz, DMSO-d_6, ppm): δ2.83 (s, OCH_2CH_2O), 6.70, 6.35 (d, CH_2CH), 6.51 (m, CH_2C*H*).

Synthesis of PEO$_{45}$-*b*-PNAS$_{66}$: To a 25 mL Schlenk flask equipped with a magnetic stir bar dried with flame under N_2 atmosphere, mPEG2k macro-CTA (0.120 g, 50 μmol) and 1,4-dioxane (10 mL) was added. The reaction mixture was stirred for 30 min at room temperature to obtain a homogeneous solution. To this solution was added NAS (0.910 g, 5.38 mmol) and AIBN (0.486 mg, 3 μmol). The reaction flask was sealed and allowed to stir for 20 min at room temperature. The reaction mixture was degassed through several cycles of freeze-pump-thaw (>3). After the last cycle, the reaction mixture was allowed to stir for 10 min at room temperature before being immersed into a pre-heated oil bath at 60 °C to start the polymerization. The polymerization was monitored by analyzing reaction aliqouts with ^{1}H NMR spectroscopy and after two and half hours it has reached the desired degree of polymerization. The polymerization was quenched by cooling the reaction flask with liquid N_2. The polymer was purified by precipitation into 400 mL of cold diethyl ether at 0 °C three times. The precipitants were collected, washed with 100 mL of cold ether, and dried under vacuum overnight to afford the PEO$_{45}$-*b*-PNAS$_{66}$ block copolymer precursor as a yellow solid (550 mg, 81% yield based upon monomer conversion). ^{1}H NMR (300 MHz, DMSO-*d*6, ppm): δ 0.86 (t, J = 6 Hz, 3H, dodecyl *CH3*), 1.15 (br, 5H, *CH*3 and dodecyl *CH2*), 1.25 (br, 19H, *CH3* and dodecyl *CH2s*), 1.30 (br, 2H, dodecyl *CH2*), 1.65 (t, J = 6 Hz, 2H, dodecyl *CH2*), 2.10 (br, PNAS backbone protons), 2.82 (NAS *CH2CH2s*), 3.20 (br, PNAS backbone protons), 3.34 (s, mPEG terminal *OCH3*), 3.52 (m, *OCH2CH2O* from the PEG backbone), 4.12 (br, 2H from the PEO backbone terminus connected to the ester linkage); ^{13}C NMR (150 MHz, DMSO-d_6, ppm): δ 25.6, 42.0, 70.1, 172.4. Mn^{NMR} = 136,00 Da, *PDI* = 1.3 (DMF GPC).

Synthesis of PEO$_{45}$-*b*-PNAS$_{66}$-*b*-PS$_{30}$: To a 100 mL Schlenk flask equipped with a magnetic stir bar dried with flame under N_2 atmosphere, was added the PEO$_{45}$-*b*-PNAS$_{66}$ macro-CTA (0.550 g, 40 μmol), 1,4-dioxane (15 mL), and DMF (5 mL). The reaction mixture was allowed to stir for 30 min at room temperature to obtain a homogeneous solution. To this solution was added styrene (1.26 g, 12 mmol) and AIBN (0.39 mg, 2.4 μmol). The reaction flask was sealed and allowed to stir for 10 min at room temperature. The reaction mixture was degassed through several cycles of freeze-pump-thaw (>3). After the last cycle, the reaction mixture was allowed to stir for 10 min at room temperature before being immersed into a pre-heated oil bath at 60 °C to start the polymerization. After 30 h, the monomer conversion reached *ca.* 10% by analyzing aliquots collected through ^{1}H NMR spectroscopy. The polymerization was quenched by cooling the reaction flask with liquid N2. The polymer was purified by precipitation into 500 mL of cold diethyl ether at 0 °C three times. The precipitants were collected and dried under vacuum overnight to afford the block copolymer precursor as a yellow solid (206 mg, quantitative yield based upon monomer conversion). ^{1}H NMR (300 MHz, DMSO-d_6, ppm): δ 0.86 (br, dodecyl *CH3*), 1.20-1.40 (br, dodecyl Hs, PNAS, and PS backbone protons), 2.90 (NAS *CH2CH2s*), 3.18 (br, PNAS backbone protons), 3.24 (s, mPEG terminal *OCH3*), 3.56 (m, *OCH2CH2O* from the PEG backbone), 6.30-7.30 (br, Ar Hs); ^{13}C NMR (150 MHz, DMSO-d6, ppm): δ 25.7, 42.1, 69.6, 126.2, 127.9, 145.7, 173.0. Mn^{NMR} = 167,00 Da, *PDI* = 1.3 (DMF GPC).

General procedure for assembly of PEO$_{45}$-*b*-PNAS$_{66}$-*b*-PS$_{30}$ into micelles: **PEO$_{45}$-*b*-PNAS$_{66}$-*b*-PS$_{30}$** (*ca.* 20 mg) polymers were dissolved in either DMF / DMSO (20 mL) in a 100 mL round bottom flask and allowed to stir for 30 min at room temperature. To this solution, an equal volume of nanopure water was added dropwise *via* a syringe pump at an addition rate of 15 mL/h. The reaction mixture was allowed to stir for additional 24 h at room temperature and dialyzed against nanopure water for 3 days in a presoaked dialysis tubing (MWCO *ca.* 6 - 8 kDa) to afford a micelle solution with a final polymer concentration of *ca*. 0.25 mg/mL.

General procedure for crosslinking the PEO$_{45}$-*b*-PNAS$_{66}$-*b*-PS$_{30}$ micelles with the fluorescent crosslinker to afford SCKs: To the **PEO$_{45}$-*b*-PNAS$_{66}$-*b*-PS$_{30}$** MCM solution was added a solution of pyrazine crosslinker in nanopure water (1.1 eq, nominal 20% crosslinking) dropwise *via* a syringe pump over a period of 2 h and the resulting mixture was allowed to stir overnight before dialysis against nanopure water or PBS for 3 days in a presoaked dialysis tubing (MWCO.ca. 6 - 8 kDa) to afford MCN solutions with a final polymer concentration of *ca.* 0.25 mg/mL. The crosslinking density was measured by UV-vis spectroscopy to be about 7 - 10%.

6.3. Results and discussion

The cylindrical micelles were obtained upon introduction of water into a solution of PEO_{45}-*b*-$PNAS_{66}$-*b*-PS_{30} dissolved in dimethylformamide (DMF). Variation of water addition rate from 10 mL/h, 15 mL/h, 20 mL/h to 30 mL/h, caused no effect on the final cylindrical morphology, and maintained the width and the length comparable across the rates. Number average hydrodynamic diameters were *ca.* 90 ± 30 nm as characterized by dynamic light scattering (DLS, Figure 6.2). Dry state widths were *ca*. 57 ± 5 nm and lengths were *ca*. 180 ± 60 nm by transmission electron microscopy (TEM, Figure 6.3, data summarized in Table 6.1). A closer look at one of the addition rates, 15 mL/h, revealed that as the water weight percent (wt%) increased from 10 wt% to 21 wt% to 32 wt% to 41 wt%, spherical micelles gradually transformed into cylindrical micelles (Figure 6.4). Upon dialysis against water, pH 6.3, pH 7.4 or pH 8.1 PBS for 3 days, cylindrical morphology and size were retained under each condition characterized by both DLS and TEM (Figure 6.5 and Figure 6.6, data summarized in Table 6.2).

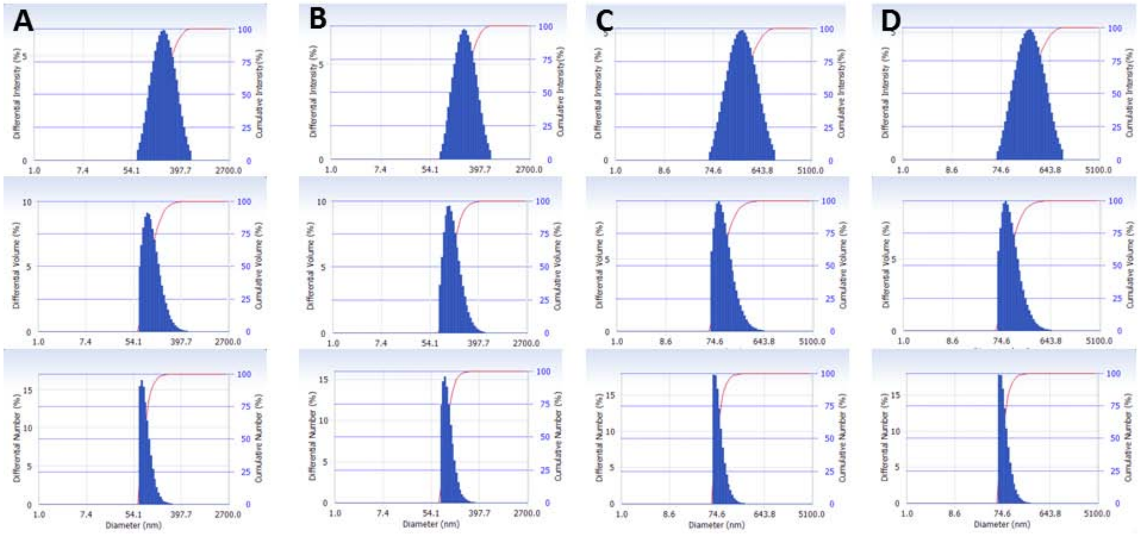

Figure 6.2. DLS histograms of intensity-averaged (first row), volume averaged (second row), and number averaged (third row) hydrodynamic diameters (determinations were average values from ten measurements, with the standard deviations being calculated as the breadth of the distributions) of PEO$_{45}$-*b*-PNAS$_{66}$-*b*-PS$_{30}$ in DMF self assembled into cylindrical micelles upon addition of water at various water addition rate: A. 10 mL/h; B. 15 mL/h; C. 20 mL/h, and D. 30 mL/h.

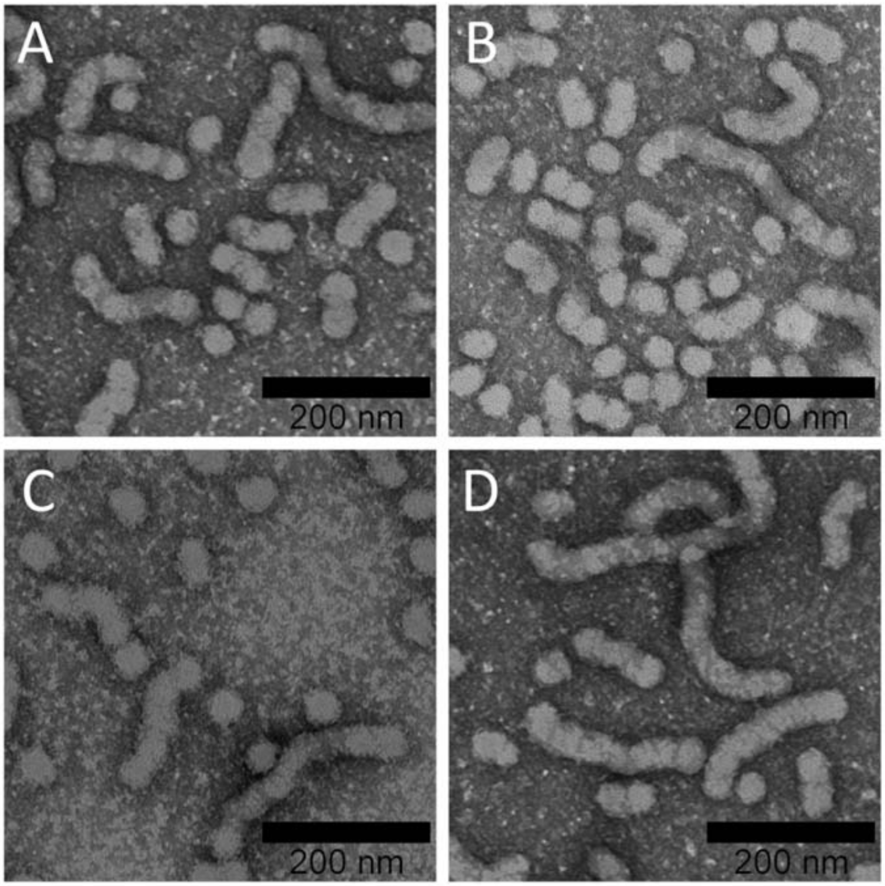

Figure 6.3. TEM images (drop deposited on carbon-coated copper grids and stained negatively with 1% PTA) of PEO_{45}-*b*-$PNAS_{66}$-*b*-PS_{30} in DMF self assembled into cylindrical micelles upon addition of water at : A. 10 mL/h; B. 15 mL/h; C. 20 mL/h; and D. 30 mL/h.

Table 6.1. Summary of characterization data for cylindrical micelles assembled from PEO_{45}-*b*-$PNAS_{66}$-*b*-PS_{30} in DMF by TEM and DLS.

Water addition rate (mL/h)	Diameter by TEM (nm)	D_h (intensity) (nm)	D_h (volume) (nm)	D_h (number) (nm)
10	Width: 60 ± 5 Length:186 ± 65	220 ± 104	124 ± 53	93 ± 25
15	Width: 55 ± 6 Length:212 ± 55	235 ± 102	145 ± 56	110 ± 29
20	Width: 59 ± 4 Length:146 ± 73	312 ± 196	123 ± 65	85 ± 25
30	Width: 52 ± 4 Length:168 ± 48	240 ± 122	130 ± 50	97 ± 26

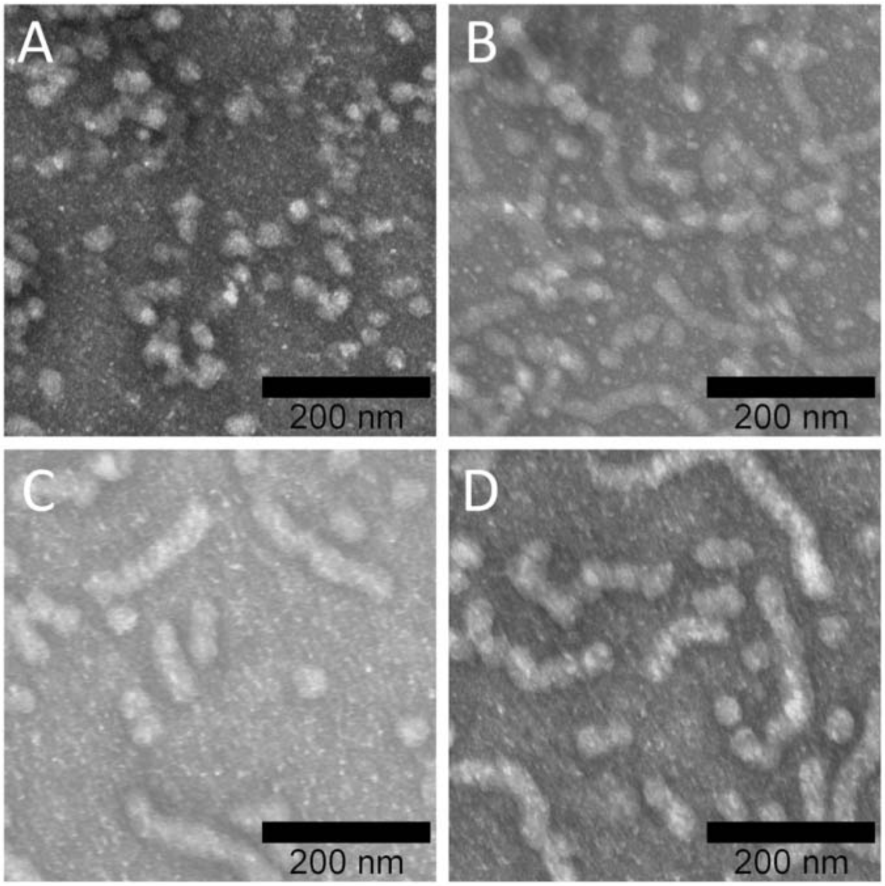

Figure 6.4. TEM images (drop deposited on carbon-coated copper grids and stained negatively with 1% PTA) of the transition of PEO_{45}-*b*-$PNAS_{66}$-*b*-PS_{30} in DMF self assembled into spherical micelles to cylindrical micelles upon increased addition of water from: A. 10 wt%; B. 21 wt%; C. 32 wt%; to D. 41 wt% at a rate of 15 mL/h.

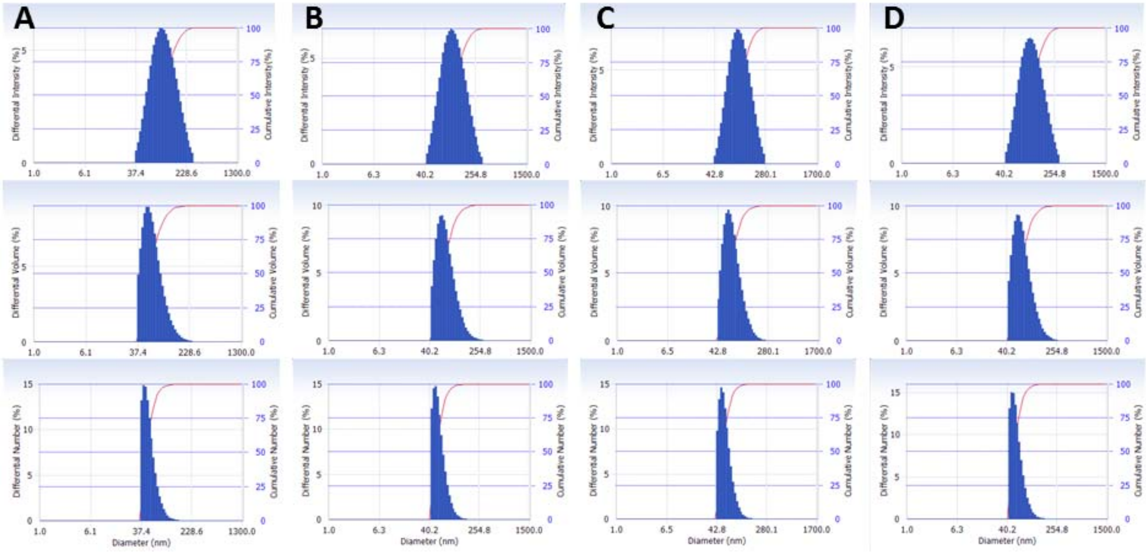

Figure 6.5. DLS histograms of intensity-averaged (first row), volume averaged (second row), and number averaged (third row) hydrodynamic diameters (determinations were average values from ten measurements, with the standard deviations being calculated as the breadth of the distributions) of PEO$_{45}$-*b*-PNAS$_{66}$-*b*-PS$_{30}$ shell crosslinked cylindrical nanoparticles (SCCN) dialyzed against A. nanopure water; B. pH 6.3 PBS; C. pH 7.4 PBS and D. pH 8.1 PBS.

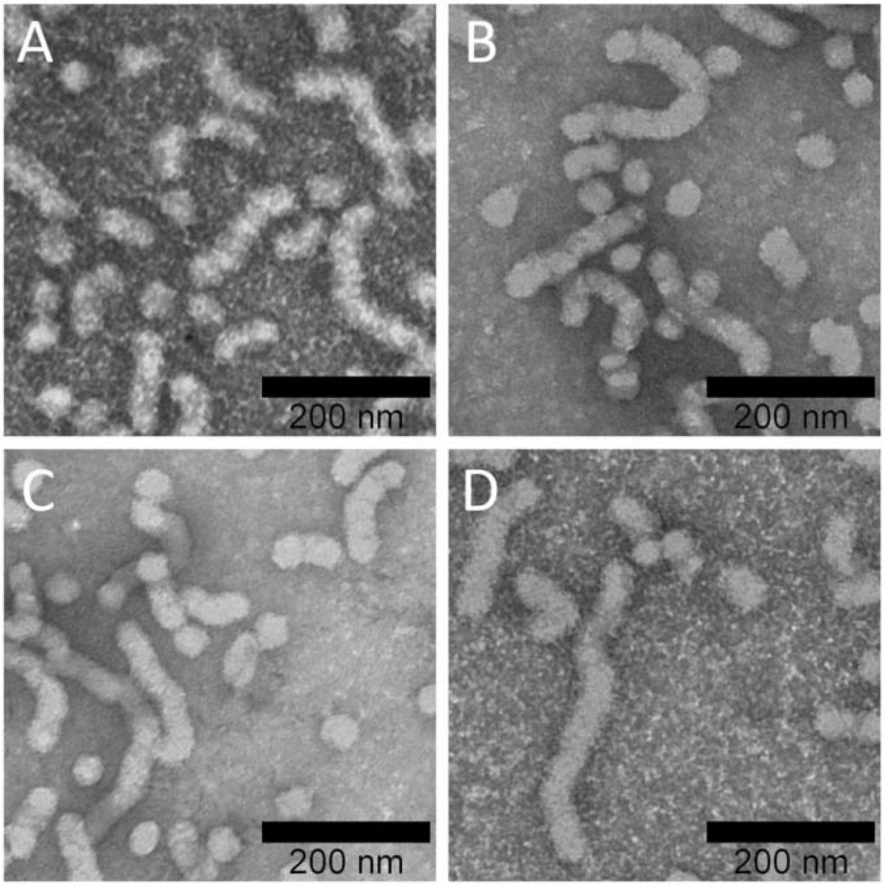

Figure 6.6. TEM images (drop deposited on carbon-coated copper grids and stained negatively with 1% PTA) of PEO_{45}-b-$PNAS_{66}$-b-PS_{30} cylindrical micelles dialyzed against A. nanopure water; B. pH 6.3 PBS; C. pH 7.2 PBS, and D. pH 8.0 PBS for 3 days.

Table 6.2. Summary of characterization data for PEO_{45}-*b*-$PNAS_{66}$-*b*-PS_{30} cylindrical micelles dialyzed against nanopure water and PBS by TEM and DLS.

	Diameter by TEM (nm)	D_h (intensity) (nm)	D_h (volume) (nm)	D_h (number) (nm)
Nanopure water	Width: 62 ± 6 Length:190 ± 82	190 ± 80	136 ± 47	112 ± 35
pH 6.3 PBS	Width: 58 ± 4 Length:185 ± 65	240 ± 130	152 ± 49	105 ± 23
pH 7.2 PBS	Width: 54 ± 6 Length:189 ± 54	235 ± 78	108 ± 72	94 ± 31
pH 8.4 PBS	Width: 59 ± 7 Length:182 ± 42	220 ± 134	142 ± 65	110 ± 34

The outer periphery of cylindrical micelles, consisting partly of PNAS residues, was covalently crosslinked by a facile one-step approach,[93,95] utilizing a pyrazine-based diamine crosslinker, which was designed to determine the crosslinking efficiency. Compared with non-crosslinked cylindrical micelles, the shell crosslinked cylindrical nanostructures (SCCN) with a crosslinking density of *ca.* 7 ~ 10% had the same morphology and comparable size of *ca.* 60 nm by TEM (Figure 6.7), indicating that the crosslinking procedure and crosslinker loading did not affect the size of the nanostructure. After 3 months of storage at room temperature, the cylindrical morphology was retained but the width of SCCNs had become much smaller by TEM (60 nm *vs.* 30 nm), for both the non-crosslinked cylindrical micelle (Figure 6.8) and SCCN (Figure 6.9). It is conceivable that the hydrolysis of PNAS groups over time has increased the effective hydrophilic block lengths together with the PEG thus constituting a smaller final nanostructure.

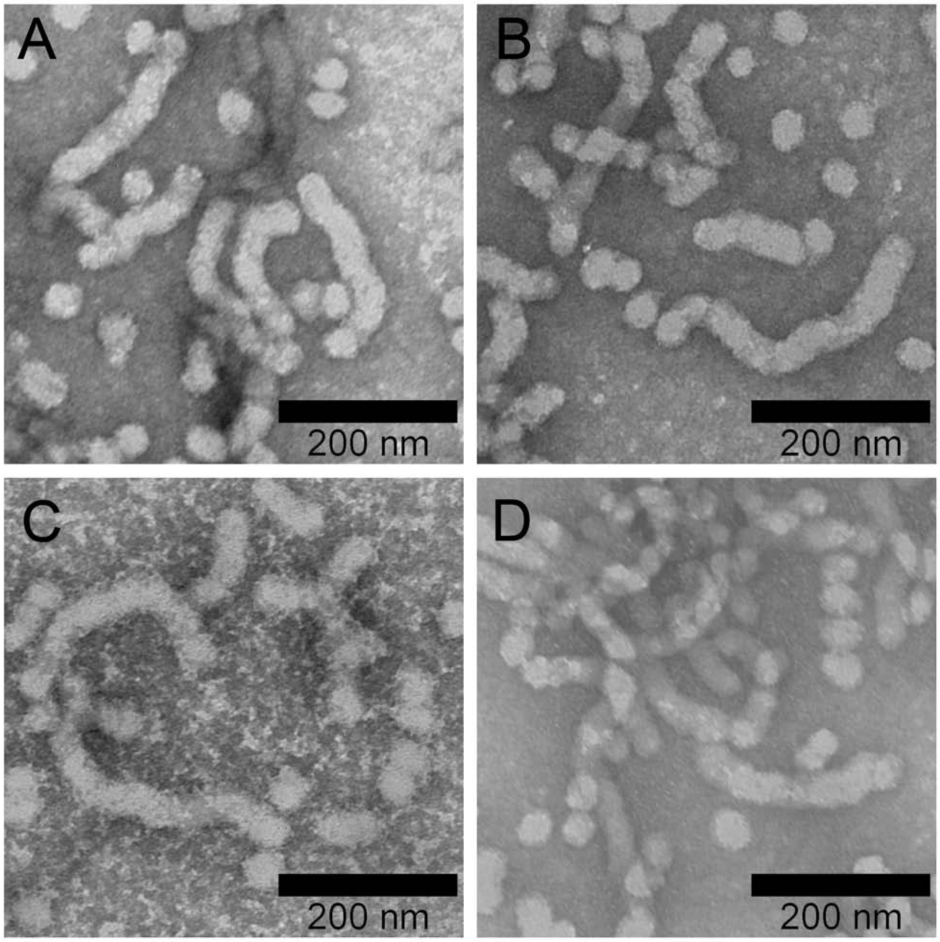

Figure 6.7. TEM images (drop deposited on carbon-coated copper grids and stained negatively with 1% PTA) of shell crosslinked cylindrical nanostructures (SCCN) dialyzed against A. nanopure water; B. pH 6.3 PBS; C. pH 7.2 PBS, and D. pH 8.0 PBS for 3 days.

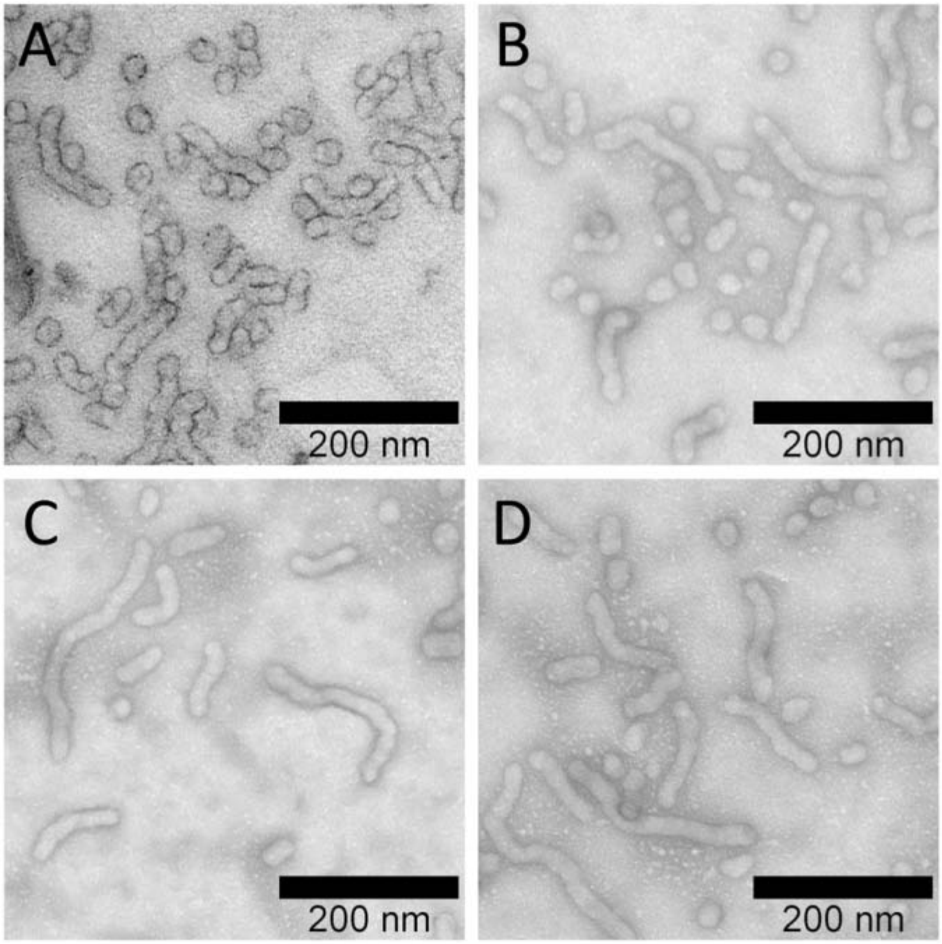

Figure 6.8. TEM images (drop deposited on carbon-coated copper grids and stained negatively with 1% PTA) of cylindrical micelles dialyzed against A. nanopure water 6.3; B. pH 6.3 PBS; C. pH 7.2 PBS, and D. pH 8.0 PBS after 3 months of storage at room temperature

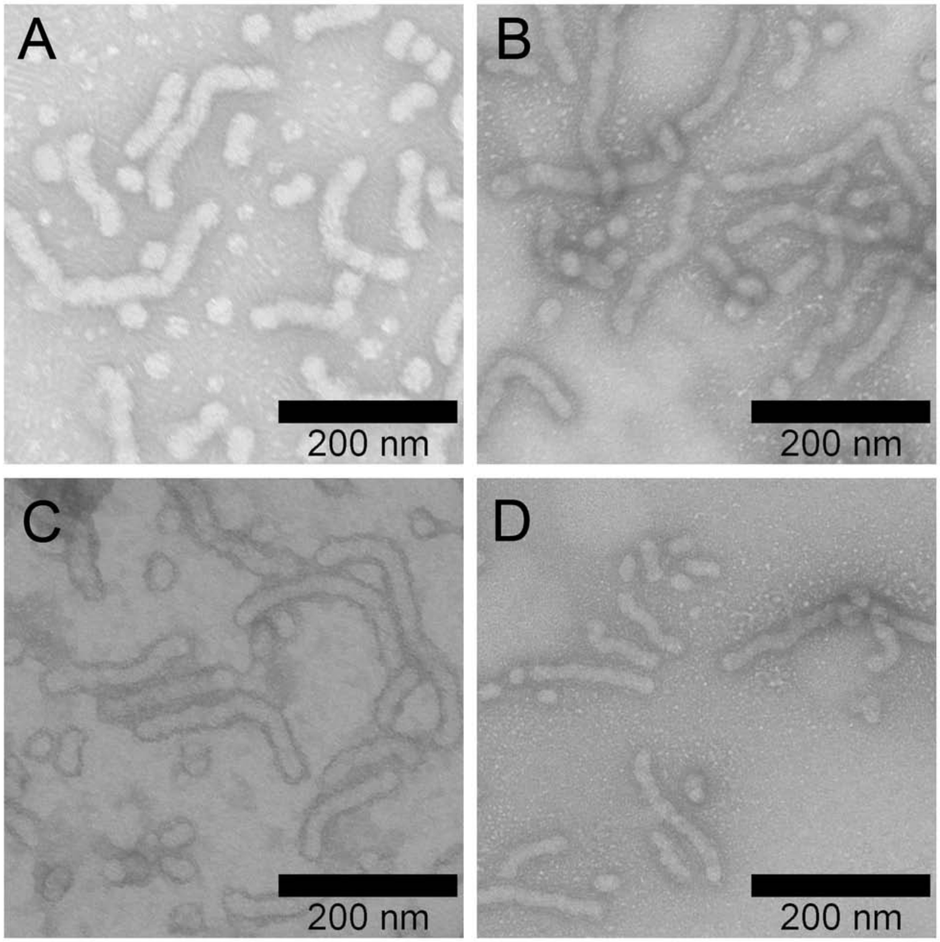

Figure 6.9. TEM images (drop deposited on carbon-coated copper grids and stained negatively with 1% PTA) of shell crosslinked cylindrical nanostructures (SCCN) dialyzed against A. nanopure water; B. pH 6.3 PBS; C. pH 7.2 PBS, and D. pH 8.0 PBS after 3 months storage at room temperature.

Another key parameter that can be used to control the morphology is solvent selectivity. We also investigated the self assembly process of PEO_{45}-*b*-$PNAS_{66}$-*b*-PS_{30} in dimethyl sulfoxide (DMSO) and characterized by DLS (Figure 6.10) and TEM (Figure 6.11, data summarized in Table 6.3). Upon introduction of water into a solution of PEO_{45}-*b*-$PNAS_{66}$-*b*-PS_{30} in DMSO, clusters of individual micelles were observed at 9 wt% water. As the water wt% increased to 19 wt%, 31 wt% and 40 wt%, the transition of individual micelles emerging into multicompartment micelles (MCMs) was captured by TEM (Figure 6.12). The reason for the striking differences in the self assembly process and the final morphology obtained through two different organic solvents is not clear but may be, in part, attributed to the differences in the surface tension of the organic solvents (DMSO 43 mJ/m^2, DMF 34 mJ/cm^2, THF 27 mJ/cm^2, water 73 mJ/cm^2 at 25 °C) among others.

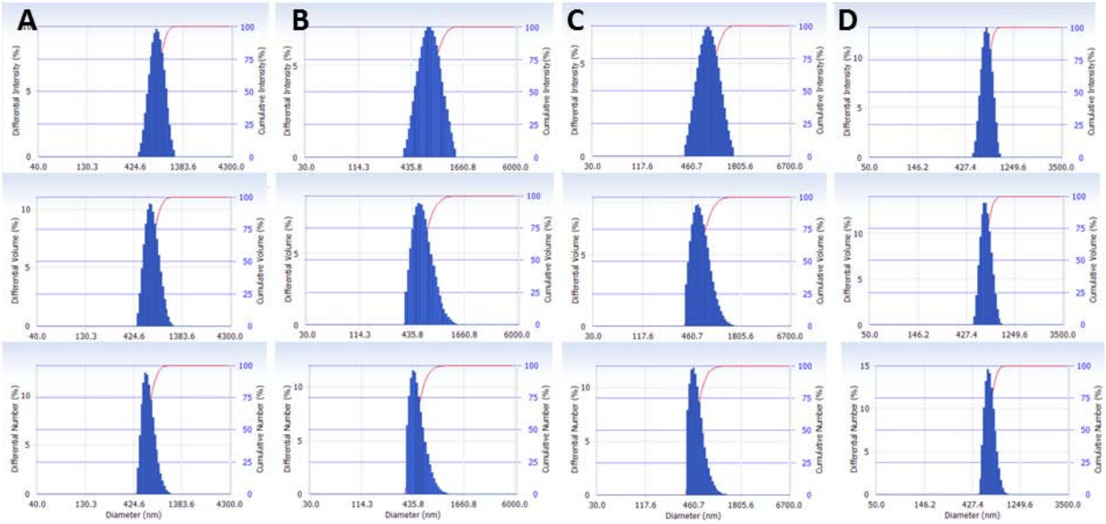

Figure 6.10. DLS histograms of intensity-averaged (first row), volume averaged (second row), and number averaged (third row) hydrodynamic diameters (determinations were average values from ten measurements, with the standard deviations being calculated as the breadth of the distributions) of PEO$_{45}$-*b*-PNAS$_{66}$-*b*-PS$_{30}$ in DMSO self assembled upon addition of water at various water addition rate: A. 10 mL/h; B. 15 mL/h; C. 20 mL/h, and D. 30 mL/h.

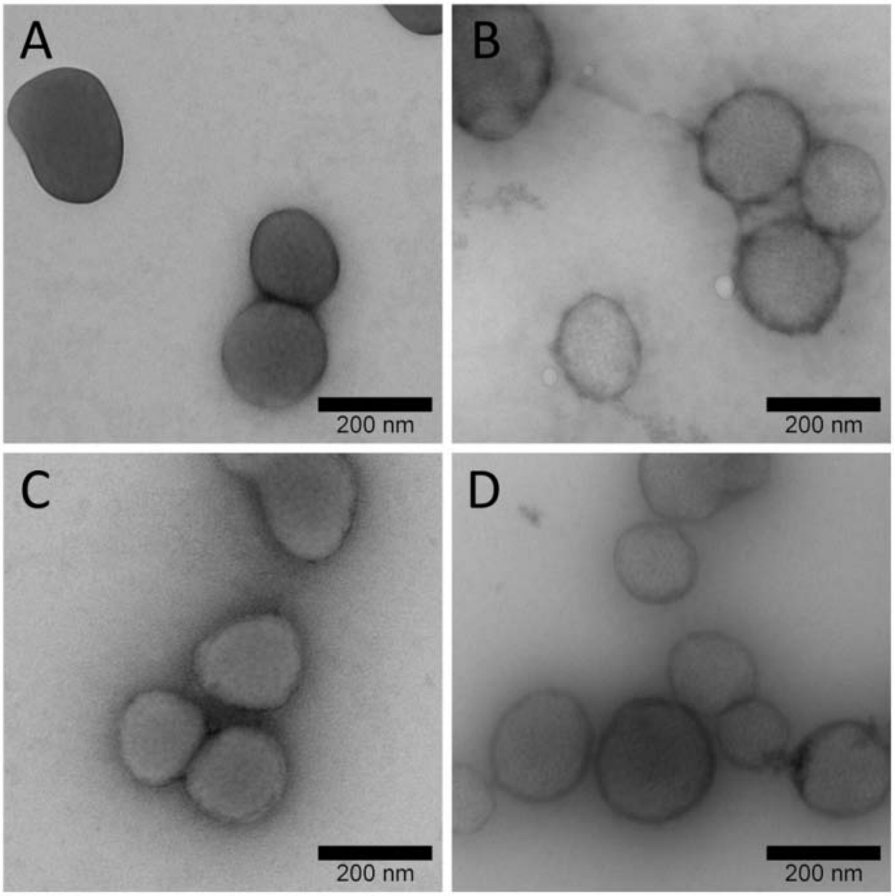

Figure 6.11. TEM images (drop deposited on carbon-coated copper grids and stained negatively with 1% PTA) of PEO$_{45}$-*b*-PNAS$_{66}$-*b*-PS$_{30}$ in DMSO self assembled into MCM upon addition of water at : A. 10 mL/h; B. 15 mL/h; C. 20 mL/h; and D. 30 mL/h.

Table 6.3. Summary of characterization data for MCMs assembled from PEO$_{45}$-*b*-PNAS$_{66}$-*b*-PS$_{30}$ in DMSO by TEM and DLS.

Water addition rate (mL/h)	Diameter by TEM (nm)	D_h (intensity) (nm)	D_h (volume) (nm)	D_h (number) (nm)
10	222 ± 25	730 ± 128	667 ± 116	615 ± 98
15	215 ± 35	722 ± 200	584 ± 153	499 ± 107
20	195 ± 19	770 ± 221	613 ± 166	520 ± 113
30	210 ± 21	689 ± 83	660 ± 80	634 ± 73

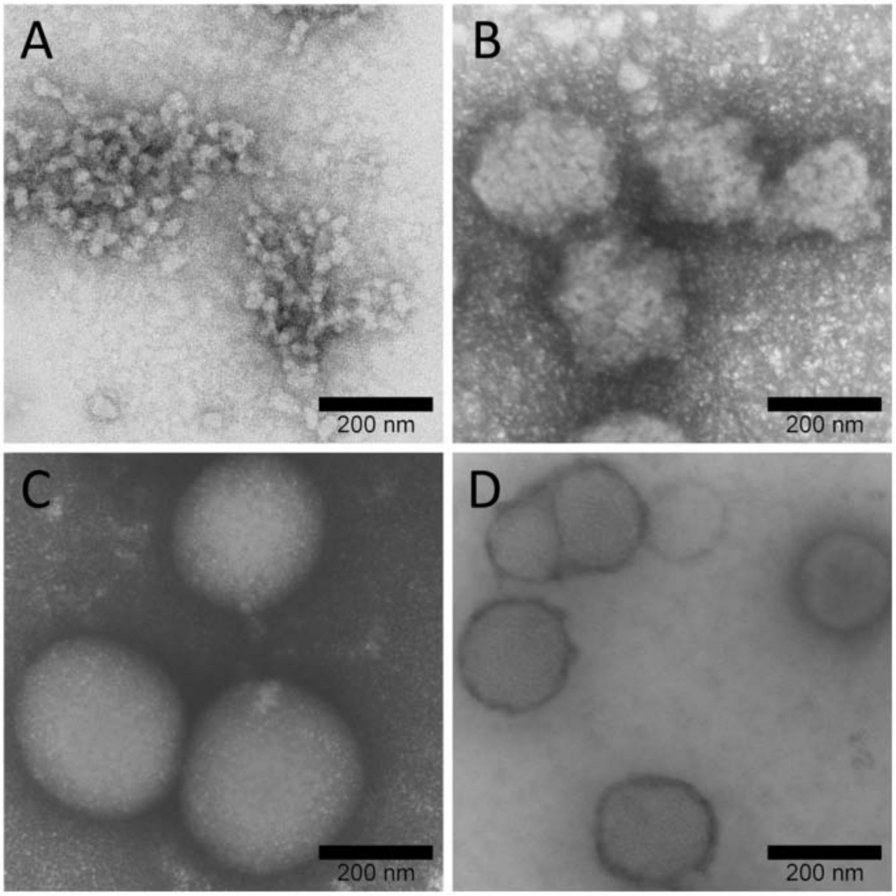

Figure 6.12. TEM images (drop deposited on carbon-coated copper grids and stained negatively with 1% PTA) of the transition of PEO_{45}-*b*-$PNAS_{66}$-*b*-PS_{30} in DMSO self assembled into spherical micelles to MCMs upon increased addition of water from: A. 9 wt%; B. 19 wt%; C. 31 wt%; to D. 40 wt% at a rate of 15 mL/h.

The multicompartment micelle exhibited a more dynamic state of morphology compared to cylinders, where dialysis conditions and the length of storage influenced the stability of the original structure. The multicompartment micelle was not affected when the water addition rate increased from 10 mL/h to 30 mL/h with the number average hydrodynamic diameter of *ca.* 560 ± 100 by DLS (Figure 6.10) and dry state diameter of *ca.* 210 ± 25 nm by TEM (Figure 6.11, Table 6.4). Upon dialysis against nanopure water, the number average hydrodynamic diameter of MCM decreased to *ca.* 300 ± 100 nm (Figure 6.13), the dry state diameter by TEM remained at *ca.* 220 ± 25 nm (Figure 6.14). However, when dialyzed against pH 6.3, pH 7.4 or pH 8.1 PBS, the multicompartment micelles disassembled into individual micelles with hydrodynamic diameter of *ca.* 40 ± 10 nm (Figure 6.13) and dry state diameter of *ca.* 25 ± 5 nm (Figure 6.14). Interestingly, after 3 months of storage at room temperature, MCMs that were dialyzed against water eventually disassembled into individual micelles as well (Figure 6.15).

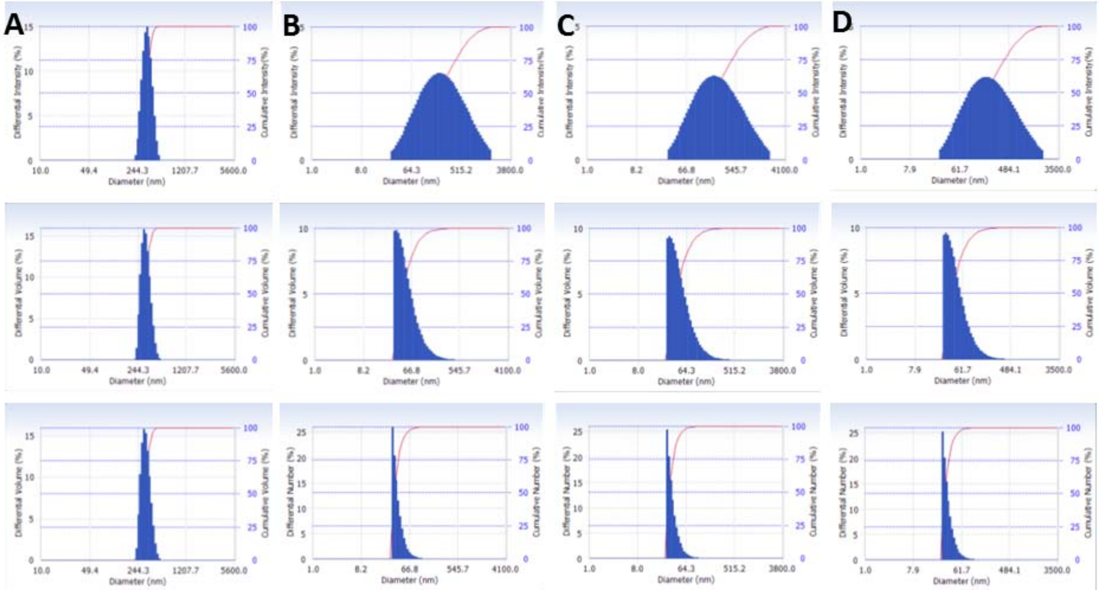

Figure 6.13. DLS histograms of intensity-averaged (first row), volume averaged (second row), and number averaged (third row) hydrodynamic diameters (determinations were average values from ten measurements, with the standard deviations being calculated as the breadth of the distributions) of PEO$_{45}$-*b*-PNAS$_{66}$-*b*-PS$_{30}$ MCM dialyzed against A. nanopure water; B. pH 6.3 PBS; C. pH 7.4 PBS and D. pH 8.1 PBS.

Table 6.4. Summary of characterization data for PEO_{45}-*b*-$PNAS_{66}$-*b*-PS_{30} MCMs dialyzed against nanopure water and PBS by TEM and DLS.

	Diameter by TEM (nm)	D_h (intensity) (nm)	D_h (volume) (nm)	D_h (number) (nm)
Nanopure water	220 ± 42	340 ± 53	315 ± 50	295 ± 42
pH 6.3 PBS	25 ± 4	332 ± 332	54 ± 36	36 ± 10
pH 7.2 PBS	24 ± 3	384 ± 398	60 ± 40	40 ± 11
pH 8.4 PBS	24 ± 5	310 ± 310	54 ± 35	37 ± 10

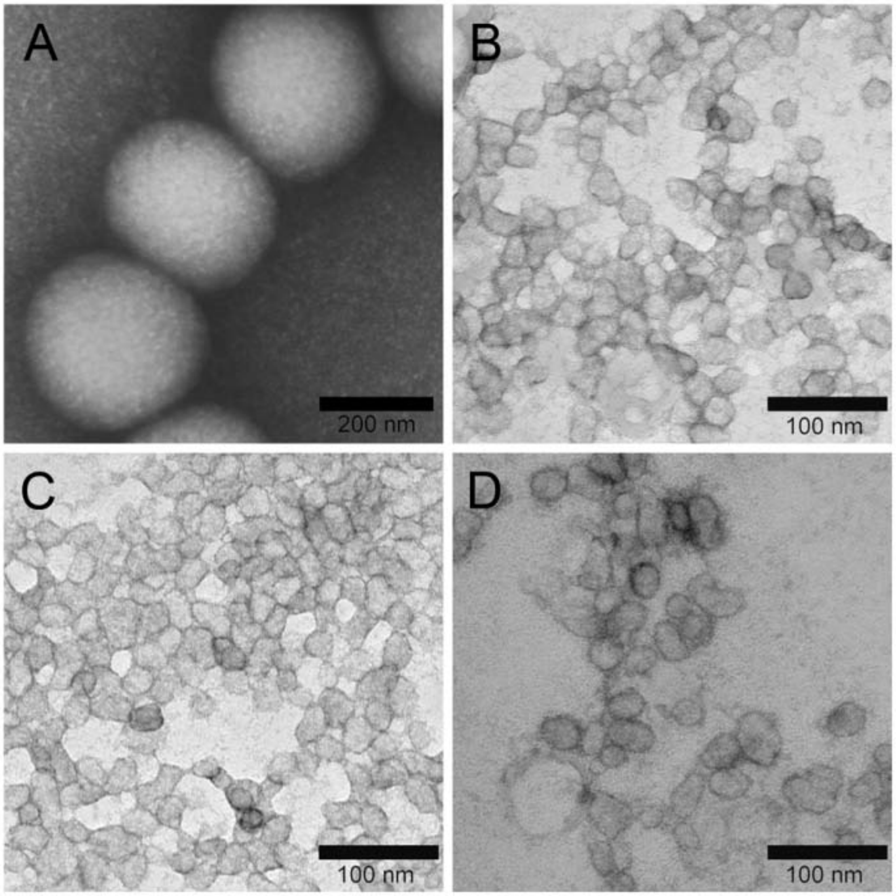

Figure 6.14. TEM images (drop deposited on carbon-coated copper grids and stained negatively with 1% PTA) of MCMs retained structure integrity when dialyzed against A. nanopure water but disassembled into individual nanoparticles upon dialysis against B. pH 6.3 PBS; C. pH 7.2 PBS, and D. pH 8.0 PBS for 3 days.

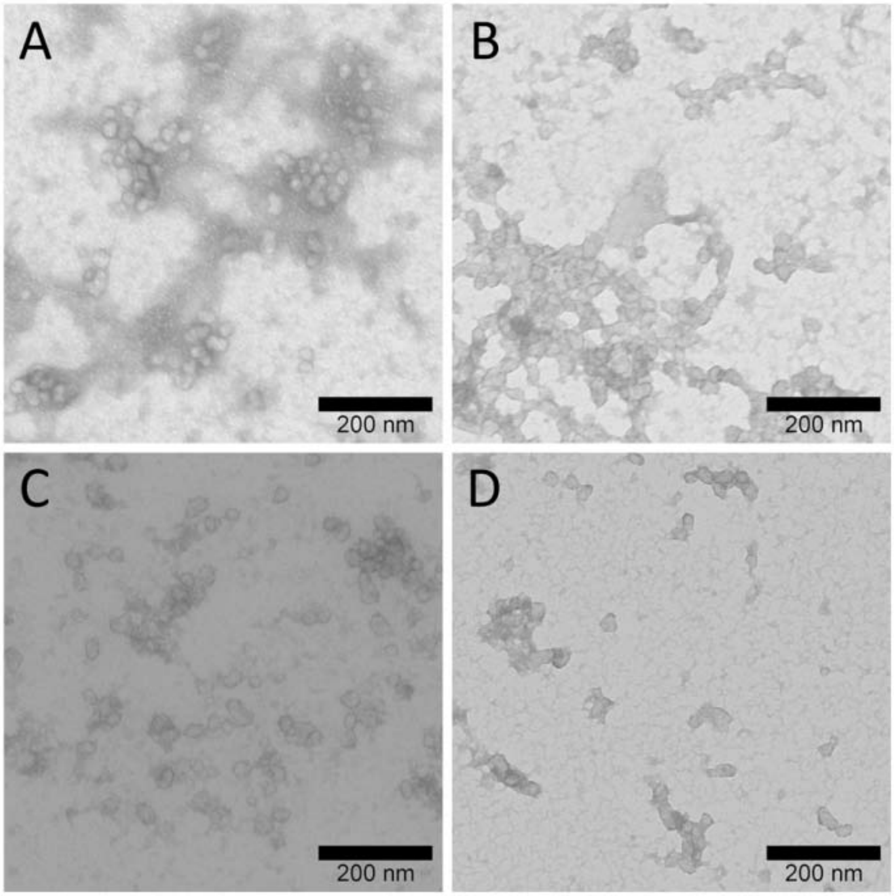

Figure 6.15. TEM images (drop deposited on carbon-coated copper grids and stained negatively with 1% PTA) of MCM dialyzed against A. nanopure water; B. pH 6.3 PBS; C. pH 7.2 PBS, and D. pH 8.0 PBS after 3 months of storage at room temperature

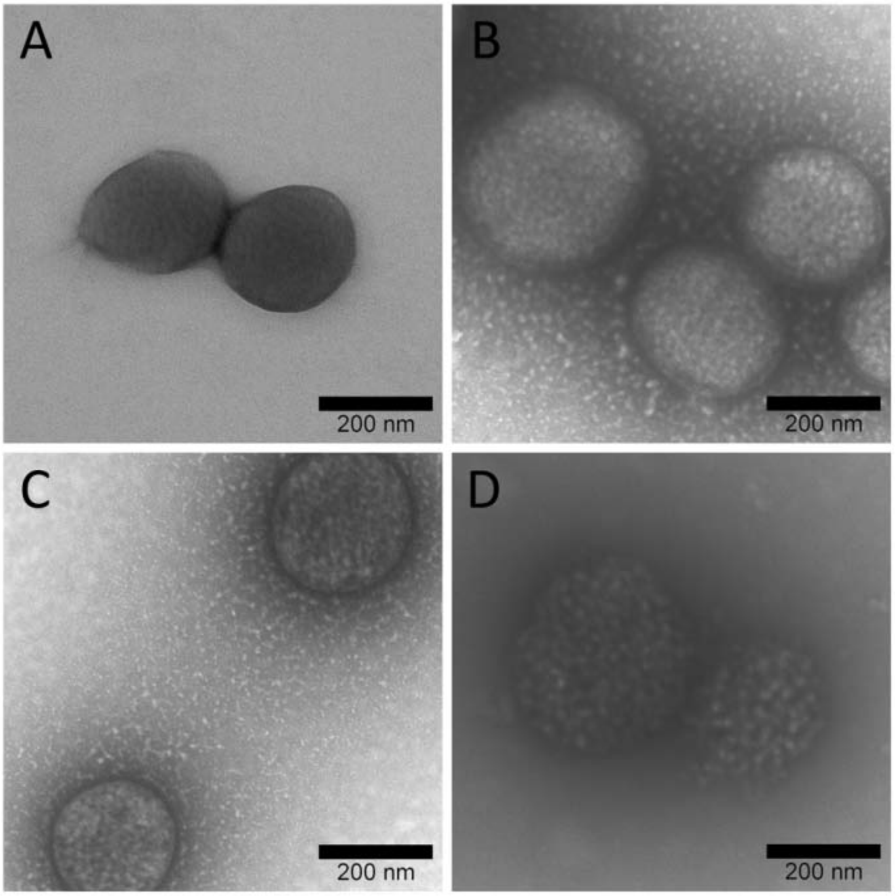

Figure 6.16. TEM images (drop deposited on carbon-coated copper grids and stained negatively with 1% PTA) of MCNs dialyzed against A. nanopure water; B. pH 6.3 PBS; C. pH 7.2 PBS, and D. pH 8.0 PBS for 3 days with retention to morphology.

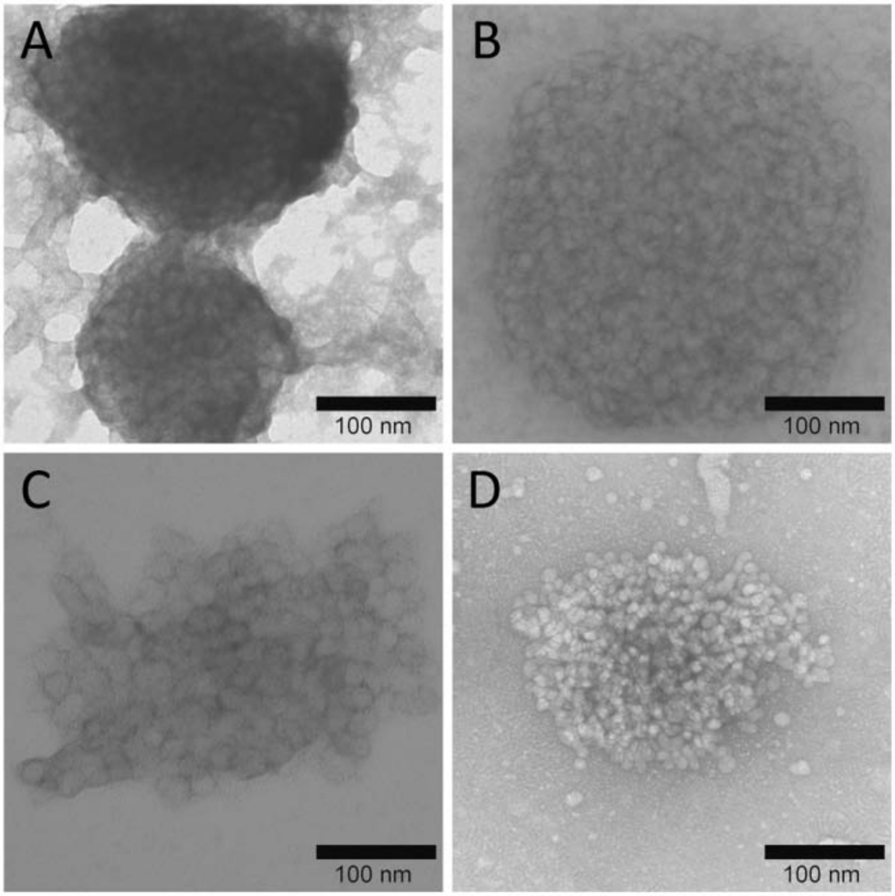

Figure 6.17. TEM images (drop deposited on carbon-coated copper grids and stained negatively with 1% PTA) of MCNs dialyzed against A. nanopure water; B. pH 6.3 PBS; C. pH 7.2 PBS, and D. pH 8.0 PBS after 3 months storage at room temperature.

The dynamic nature of the multicompartment aggregates was suppressed by chemical covalent crosslinking reactions. The MCMs were crosslinked with pyrazine crosslinker to form more stable multicompartment nanostructures (MCNs). The MCNs displayed a similar size of *ca.* 210 ± 30 nm compared with MCMs by TEM, and did not disassemble into individual micelles upon dialysis against water or PBS of varying pH values (Figure 6.16). Even after 3 months of storage at room temperature, the aggregates remained intact with more prominent phase segregation especially at pH 7.2 and pH 8.0 (Figure 6.17).

6.4. Conclusions

Versatility of a triblock copolymer, PEO_{45}-*b*-$PNAS_{66}$-*b*-PS_{30}, was demonstrated through accessing two distinct morphologies *via* facile preparation methods in organic solvent and water mixture. It was further shown that chemically functional moieties regioselectively present within the nanoscale framework of the multicompartment micelles had allowed for a control over morphology stability despite the energetically favourable route to individual spheres.

6.5. Acknowledgements

Financial support from Covidien is gratefully acknowledged. K. L. Wooley serves as a consultant to Covidien. This work was also supported by the Welch Foundation through the W. T. Doherty-Welch Chair in Chemistry, Grant No. A-0001

CHAPTER VII

F3-PEPTIDE-CONJUGATED, DOXORUBICIN LOADED NANOPARTICLES AS COMPLEX THERANOSTICS IN THE TREATMENT OF PEDIATRIC BRAIN CANCERS

7.1. Introduction

Current treatments of brain tumors, especially malignant glioblastomas, the most common and aggressive type of primary brain tumors in human, include surgery, radiation and chemotherapy.[180-182] However, surgical resection is only to the extent that is safely feasible and sometimes poses the greatest challenge as crucial tissues near the tumor that controls critical functions may also be damaged.[182] To further improve eradiation of tumors, other regimens such as radiation and chemotherapy are developed, but radiation is limited by serious side effects including decline in cognitive function and development of secondary malignancy[183] whereas chemotherapy suffers from systemic side effects, and is also limited by the fact that therapeutic agents are unable to penetrate the blood-brain barrier (BBB).[184]

The BBB, formed by the endothelial cells of the cerebral capillaries that line the microvasculatures of the brain, prevents the entry of most blood-borne substance, including potential toxins and therapeutics, into the central nervous system (CNS) through its selective permeability.[185] Doxorubicin (DOX) is a widely used chemotherapy drug in glioblastoma cell lines,[186-188] which unfortunately causes serious side effects and seldom has any effect in brain tumors patients because it lacks the ability to cross the BBB.[189] Passive diffusion of substances across the BBB could sometimes occur but is highly dependent on its lipophilicity and molecular weight.[186,190,191] Therefore, designing paradigm-changing drug delivery systems that can penetrate through the BBB and offer the possibility for local delivery of drugs to the tumor sites are of prime importance.

Nanoparticle-based drug delivery systems for cancer therapy have been successful, in part, due to their size, which allows for biased accumulation of the drug in the tumor sites by enhanced permeability and retention (EPR) effect through leaky vasculature around the tumor cells to achieve passive targeting.[97] Many of such systems have been approved by the U. S. Food and Drug Administration: liposomal doxorubicin (Myocet™, Elan pharmaceuticals), PEGylated liposomal doxorubicin (Doxil®, Ortho Biotech, and Caelyx®, Schering Plough) and albumin-bound paclitaxel-loaded nanoparticles (Abranxane®, Abraxis Bioscience) as some of the examples.[192-194] The EPR effect is a consequence of inherently leaky vasculature created due to the rapid vascularization that is required to serve aggressive cancer cell growth and poor lymphotropic clearance.[97] Small molecular weight compounds, such as conventional chemotherapeutic drugs, can be taken up through free diffusion by both tumor tissue and cancerous tissue with no bias.[180] With increased vascular permeability around the tumor environment, nanoparticles and liposomes ranging from 10 nm to 500 nm in size can accumulate in the tumor area to a greater extent than in the normal tissue area.[156] Nanoparticles loaded with therapeutic cargo in the sub-100 nm size region show much stronger activity with increased drug concentration through the EPR effect compared with free anticancer drugs while avoiding uptake by the mononuclear phagocytic system (MPS).[180,195] For instance, polymeric micelles (*ca.* 80 nm) constructed from poly(ethyleneglycol)-*b*-poly(*N*-2-hydroxypropyl methacrylamide-lactate) conjugated with DOX demonstrated better suppression in the growth rate of melanoma carcinoma tumors in mice compared with free DOX.[196] Pluronic polymer micelles (*ca.* 25 nm) encapsulated with paclitaxel (PTX) showed significant tumor growth delay and increased survival compared with PTX alone.[197] However, accumulation of drugs within the tumor microenviroment by the EPR effect may not be enough for drugs that require cellular internalization for efficacy, thus a combination with active targeting is favored over passive targeting alone. Towards ultimate specificity and elimination of toxicity to healthy cells, active targeting through incorporation of targeting ligands within the nanoparticles delivery system is necessary in addition to the benefits given from being in the nanoscale regime.

Active targeting can be achieved by conjugation of a targeting ligand that recognizes and interacts with a specific site on the tumor cells, which leads to an accumulation of the nanoparticles around the tumor site to increase the therapeutic effectiveness.[75] Many nanoparticle delivery systems today achieve high efficacy in drug delivery through active targeting based on markers for angiogenesis and tumor vasculature, such as vascular endothelial growth factor (VEGF), or markers of tumor cells, such as EGFR. Nucleolin, a shuttle protein that controls DNA and RNA metabolism traffic between the cytoplasm and the nucleus, is found to be over-expressed on the surface of both proliferating angiogenic microvascular endothelial cells and tumor cells, thus has been used as an angiogenesis marker and tumor specific moiety for binding with targeting ligands and/or peptides.[198-200] A 31-amino acid fragment, F3 peptide, corresponds to the nucleosomal binding domain of a high mobility group protein HMGN2 and functions as a tumor homing peptide to the vasculature of various types of tumors by binding to the endothelial cell.[199,201] The attachment of F3 peptide to tumor blood vessel and internalization into tumor cells is due to the binding with the surface over-expressed nucleolin receptor.[202] Many studies have demonstrated that peptide-nanoparticle conjugates retain the ability of peptides to achieve specific targeting: F3 peptide-targeted polyacrylamide nanoparticles were internalized by rat glioma cells *in vitro*, to a higher extent (more than 100 fold) compared with non-targeted nanoparticles,[203] dextran-coated iron oxide nanoparticles conjugated with F3 peptide specifically bound to nucleolin expressed on the surface of breast tumor cells and were quickly internalized and shuttled to the nuclei of the cell.[204] F3 peptide-targeted cisplatin-loaded polyacrylamide nanoparticles showed cytotoxic activity against ovarian tumor cells *in vitro* and bound to tumor vessels *in vivo* and achieved near complete loss of all tumor vessels in a murine model of ovarian cancer.[205]

Our group has developed shell-crosslinked knedel-like nanoparticle (SCK) drug delivery systems as potential treatments for various aspects of disease[146] and investigated their size,[39] shape effect,[91] and conjugation with targeting ligands for active delivery of therapeutics.[206] Among many nanoparticulate systems, supramolecular self-assembled nanoparticle micelles from amphiphilic block copolymers provide unique core-shell morphology, where the hydrophobic core can serve as a reservoir for hydrophobic therapeutic cargos and imaging agents while the hydrophilic shell protects the encapsulated drug molecules from the environment and can be tailored for attaching targeting ligands. The SCK nanoparticles are covalently crosslinked in the shell region allowing them to have greater stability and also gate transport of encapsulated drug molecules.[91,93] The dimensions of the nanoparticles can be easily tuned, by manipulation of polymer precursor length and composition, to accommodate specific drug agents and to control nanoparticle surface chemistry for functionalization to allow site-specific delivery of imaging and therapeutic agents.

In this study, we have designed a multifunctional nanodevice for imaging and drug delivery, constructed from poly(acrylic acid)-*b*-polystyrene (PAA-*b*-PS) polymer precursor, functionalized with a chelator for radio-labeling, polyethylene glycol (PEG) for improved circulation time, targeting ligands, a chromophore and a therapeutic agent for *in vivo* active-targeted delivery and tracking. We were able to tune the dimensions of the nanoparticles, by controlling the relative and overall volumes occupied by the hydrophilic and hydrophobic polymer chain segments, and to alter the surface chemistry for attachment of targeting ligands to achieve high therapeutic efficacy through both passive and active targeting.

7.2. Materials and methods

7.2.1. Materials

All reagents were obtained from Sigma-Aldrich (St. Louis, MO) and used as received unless otherwise indicated. PAA_{52}-*b*-PS_{30} polymer **1** was synthesized as previously reported. Boc-NH-PEG_{3kDa}-NH_2 (Rapp Polymere, Tübingen, Germany), MeO-PEG_{2kDa}-NH_2 (Rapp Polymere, Tübingen, Germany), *N*-hydroxysulfosuccinimide (Sulfo-NHS) (Thermo Scientific, Waltham, MA.), *N*-succinimidyl-S-acetylthiopropionate (SATP) (Pierce, Waltham, MA.) and Ellman's reagent kit (Pierce, Waltham, MA.), Cascade Blue® ethylenediamine, trisodium salt (Invitrogen, Carlsbad, CA.) were used as received. FITC-F3-peptide (FITC-KDEPQRRSARLSAKPAPPKPEPKPKKAPAKK), scrambled FITC peptide (FITC-KDEARALPSQRSRKPAPPKPEPKPKKAPAKK, and unlabeled F3-peptide (KDEPQRRSARLSAKPAPPKPEPKPKKAPAKK) was obtained from Tianma Pharma, China. Spectra/Por membrane tubes were purchased from Spectrum Medical Industries, Inc., and were used for dialysis. Sephadex-G75 medium was obtained from GE Healthcare. Nanopure water (18 MΩ•cm) was acquired by means of a Milli-Q water filtration system (Millipore Corp., Billerica, MA.)

7.2.2. Instruments

^{1}H NMR and ^{13}C NMR spectra were collected on a Varian Mercury 300 spectrometer, using the residual solvent signal as internal standard. Infrared spectra were acquired on an IR Prestige 21 instrument from Shimadzu Corporation (Columbia, MD). UV-Vis spectra were collected at 37 °C in the region of 200 - 800 nm, using a

Varian Cary 100 Bio UV-visible spectrophotometer. Dynamic light scattering measurements were conducted with a Brookhaven Instruments, Co. (Holtsville, NY) DLS system equipped with a model BI-200SM goniometer, BI-9000AT digital correlator, and a model EMI-9865 photomultiplier, and a model Innova 300 Ar ion laser operated at 514.5 nm (Coherent Inc., Santa Clara, CA). Measurements were made at 25 ± 1 °C. Prior to analysis, solutions were filtered through a 0.45 μm Millex®-GV PVDF membrane filter (Millipore Corp., Medford, MA) to remove dust particles. Scattered light was collected at a fixed angle of 90°. The digital correlator was operated with 522 ratio spaced channels, and initial delay of 5 μs, a final delay of 50 ms, and a duration of 8 minutes. A photomultiplier aperture of 400 μm was used, and the incident laser intensity was adjusted to obtain a photon counting of between, 200 and 300 kcps. The calculations of the particle size distributions and distribution averages were performed with the ISDA software package (Brookhaven Instruments Company), which employed single-exponential fitting, Cumulants analysis, and CONTIN particle size distribution analysis routines. All determinations were average values from ten measurements. Transmission electron microscopy (TEM) bright-field imaging was conducted on a Hitachi H-7500 microscope, operating at 80 kV. The samples were prepared as follows: 4 μL of the dilute solution (with a polymer concentration of *ca.* 0.2 - 0.5 mg/mL) was deposited onto a carbon-coated copper grid, which was pre-treated with absolute ethanol to increase the surface hydrophilicity. After 5 min, the excess of the solution was quickly wicked away by a piece of filter paper. The samples were then negatively stained with 4 μL of 1 wt% phosphotungstic acid (PTA) aqueous solution. After 1 min, the excess PTA solution was quickly wicked away by a piece of filter paper and the samples were left to dry under ambient conditions overnight.

7.2.3. Experiment procedures

Preparation of PAA_{52}-*g*-(CONH-lysine-DOTA-Boc)-*b*-PS_{30}, (2): A flame-dried 10 mL round bottom flask equipped with a magnetic stir bar was charged with polymer PAA_{52}-*b*-PS_{30}, **(1)** (200 mg, 27 µmol) and dry DMF (5 mL). To the stirred solution 1-hydroxy-benzotriazole (HOBt) (38 mg, 280 µmol) and 1-ethyl-3-(3-dimethylaminopropyl) carbodiimide (EDCI) (54 mg, 282 µmol) were added and the reaction was left to proceed for 1 h, after which a solution of Boc-DOTA-lysine **3** (58 mg, 83 µmol, 3 eq. with respect to the acrylic acid unit) dissolved in 1 mL of DMF was added. The reaction mixture was further stirred 20 h at room temperature before being transferred to a presoaked dialysis tubing (MWCO *ca*. 6 - 8 kDa), and dialyzed against nanopure water for 4 days, to remove all of the impurities and to afford polymer **2** as a white solid after lyophilization (367 mg, 60 %, 2 DOTA/polymer chain). ^{1}H-NMR: M_n = 8600 Da. ^{1}H NMR (DMF-d_7): δ 0.84 (t, CH_3CH_2-), 1.15 (br, -CH_2- of lysine) 1.24-1.83 (br, -$CHCH_2$- of the polymer backbone, alkyl chain of initiator, and $HOOCC(CH_3)_2$-), 1.49 (s, -CCH_3 DOTA), 1.90-2.21 (br, -$CHCH_2$- of the polymer backbone), 2.33-2.52 and 2.92-4.10 (br, DOTA), 6.49-7.32 (br, *Ar-H*) ppm.

Preparation of PAA_{45}-*g*-(CONH-lysine-DOTA-Boc)$_3$-*g*-(CONH-PEG_{3kDa}-NH-Boc)$_2$-*g*-(CONH-PEG_{2kDa}-OMe)$_2$-*b*-PS_{30} (3): A flame-dried 10 mL round bottom flask equipped with a magnetic stir bar was charged with **2** (0.2 mg, 23 µmol) and dry DMF (5 mL). To the stirred solution HOBt (38 mg, 0.28 mmol, 12 eq.) and EDCI (54 mg, 0.28 mmol) were added and the reaction was left to proceed for 1 h, after which a solution of NH_2-PEG_{3kDa}-NH-Boc (0.21 g, 70 µmol, ~3 eq. with respect to acrylic acid unit), NH_2-PEG_{2kDa}-OMe (0.14 mg, 70 µmol, ~3 eq. with respect to acrylic acid unit) dissolved in DMF (1 mL) was added. The reaction mixture was further allowed to stir for 20 h at room temperature before being transferred to a presoaked dialysis tubing (MWCO *ca*. 6 - 8 kDa), and dialyzed against nanopure water for 4 days, to remove all of the impurities and afford polymer **3** as a white solid after lyophilization (0.44 mg, 76 %, 5 PEG/polymer chain). ^{1}H-NMR: M_n = 18,700 Da. ^{1}H-NMR (DMSO-d_6): δ 0.86 (t, CH_3CH$_2$-), 1.08 (br, -CH$_2$- of lysine) 1.21-1.87 (br, -CHCH_2- of the polymer backbone, alkyl chain of initiator, and HOOCC(CH_3)$_2$-), 1.40 (s, -CCH_3 of PEG), 1.47 (s, -CCH_3 DOTA), 2.10-2.41 (br, -C*H*CH$_2$- of the polymer backbone), 2.45-2.61 and 3.12 (br, -OCH$_3$ of PEG), 3.42-4.12 (br, DOTA, -CH_2CH_2O-), 6.49-7.32 (br, *Ar-H*) ppm.

Preparation of PAA_{45}-*g*-(CONH-lysine-DOTA-COOH)$_3$-*g*-(CONH-PEG_{3kDa}-NH_2)$_2$-*g*-(CONH-PEG_{2kDa}-OMe)$_2$-*b*-PS_{30} (4): A flame-dried 25 mL round bottom flask equipped with a magnetic stir bar was charged with **3** (0.27 mg), and dichloromethane (15 mL). Trifluoroacetic acid (TFA, 10 mL) was added to the stirring solution and the reaction was allowed to stir overnight at room temperature, after which the solvent was removed under vacuum. The crude product was re-suspended in 10 mL of THF and transferred to a pre-soaked dialysis tubing (MWCO *ca*. 6 - 8 kDa), and dialyzed against nanopure water for 4 days, to remove all of the impurities. The solution was then lyophilized to yield the resulting yellowish solid of **4** (218 mg, 85% yield). ^{1}H-NMR: M_n = 18,300 Da. ^{1}H-NMR (DMF-d_7): δ 0.84 (t, CH_3CH$_2$-), 1.26 (br, -CH$_2$- of lysine)

1.20-2.12 (br, -CHCH_2- of the polymer backbone, alkyl chain of initiator, and HOOCC(CH_3)$_2$-), 2.16-2.51 (br, -C*H*CH$_2$- of the polymer backbone), 2.40-2.60 and 3.18 (br, -OCH$_3$ of PEG), 3.32-4.24 (br, DOTA) and (br, -CH_2CH_2O-), 6.42-7.41 (br, *Ar*-*H*) ppm.

Preparation of PAA$_{45}$-*g*-(CONH-lysine-DOTA-COOH)$_3$-*g*-(CONH-PEG$_{3kDa}$-NHCO-C$_3$H$_6$-SCOCH$_3$)$_2$-*g*-(CONH-PEG$_{2kDa}$-OMe)$_2$-*b*-PS$_{30}$ (5), General procedure for the introduction of masked SH groups: Polymer **4** (0.17 g, 9.3 µmol), and SATP (46 mg, 0.19 mmol, 10 eq./NH$_2$) were reacted in dry DMF (5.0 mL) for 24 h at room temperature before being transferred to a presoaked dialysis tubing (MWCO *ca*. 6 - 8 kDa), and dialyzed against nanopure water for 4 days, to remove all of the impurities and afford polymer **5** as a white solid after lyophilization (0.18 g, 95 % yield). ^{1}H-NMR: M$_n$ = 18,800 Da. ^{1}H-NMR (DMSO-d_6): δ 0.83 (t, CH_3CH$_2$-), 1.08-2.01 (br, -CHCH_2- of the polymer backbone, alkyl chain of initiator, and HOOCC(CH_3)$_2$-), 2.10-2.40 (br, -C*H*CH$_2$- of the polymer backbone), 2.30 (s, -SCOCH_3), 2.68-2.81 (br, -CH_2S), 3.47-3.53 (br, -OCH_2CH_2O-), 3.12 (br, -OCH$_3$ of PEG), 6.21-7.31 (br, *Ar*-*H*) ppm.

General procedure for the preparation of the micelles and SCKs (6): Polymer **5** (*ca*. 50 mg) polymers were dissolved in DMF (50 mL) in a 250 mL round bottom flask and allowed to stir for 30 min at room temperature. To this solution, an equal volume of nanopure water was added dropwise *via* a syringe pump over a period of 3 h. The reaction mixture was allowed to stir for additional 24 h at room temperature and dialyzed against nanopure water for 4 days in a presoaked dialysis tubing (MWCO *ca*. 6 - 8 kDa) to afford a micelle solution with a final polymer concentration of 0.24 mg/mL.

To the micelle solution was added a solution of 2,2′-(ethylenedioxy)bis(ethylamine) (EDDA) in nanopure water (*ca*. 10 mg/mL, 1.1 eq, nominal 20% crosslinking) dropwise *via* a syringe pump over a period of 2 h. To this solution, EDCI in nanopure water (12 mg/mL, 1.4 eq) was added dropwise *via* a syringe pump over 20 min and the resulting mixture was allowed to stir overnight before dialysis against nanopure water for 4 days in presoaked dialysis tubing (MWCO.*ca*. 6 - 8 kDa) to afford SCK solutions **6** with a final polymer concentration of *ca*. 0.24 mg/mL. D_{av} (TEM) = 8 ± 2 nm, $(D_h)_n$ (DLS) = 22 ± 6 nm; $(D_h)_v$ (DLS) = 53 ± 11 nm; $(D_h)_i$ (DLS) = 127 ± 15 nm.

General procedure for the fluorescein labeling of the SCKs with cascade blue: A solution of EDCI in nanopure water (20 mg, 66 µmol) was added dropwise over 2 min to a solution of SCK in nanopure water (20 mL, 0.24 mg/mL polymer concentration). The reaction mixture was stirred for *ca*. 15 min at 4 °C. To this solution, a solution of sulfo-NHS in nanopure water (26 mg, 0.12 mmol) was added drop wise over 5 min. The reaction mixture was further stirred 2 h at room temperature, then the pH was adjusted to 7.4 by the addition of 0.1 M PBS pH 8.3 buffer (250 µL), and a solution of 1,3,6-pyrenetrisulfonic acid, 8-[2-[(2-aminoethyl)amino]-2-oxoethoxy], trisodium salt (Cascade Blue® ethylenediamine, trisodium salt) (13 µg, in nanopure water) was added to the reaction. The reaction was left to proceed for 20 h at room temperature before being transferred to presoaked dialysis tubing (MWCO *ca*. 6 - 8 kDa), and dialyzed against buffer (100 mM PBS, 0.1 M NaCl, 10 mM EDTA, pH 7.4) for 4 days, to remove all of the impurities and afford the Cascade Blue labeled SCK solution (CB-SCK) with a final concentration of 0.24 mg/mL. Number of dye molecules was found to be *ca*. 10 per SCK.

General deprotection step for the Cascade Blue labeled SCKs: Hydroxyl amine hydrochloride (200 µL, 0.5 M in aqueous buffer, 100 mM PBS, 0.1 M NaCl, 10 mM EDTA, pH 7.4) was added to a stirred solution of CB-SCK suspended in buffer (2 mL, 100 mM PBS, 0.1 M NaCl, 10 mM EDTA, pH 7.4) and allowed to stir for 3 h at room temperature to expose the thiol group on the CB-SCK. The solution was assayed by Ellman's method resulting in a concentration of 105 ± 12 µM [SH], after which the coupling of maleimide-F3 peptide was performed immediately.

Sulfo-SMCC modification of the F3 peptide and general conjugation protocol to produce F3-CB-SCK, 7: F3 peptide (3.0 mg, 0.75 µmol (M_n = 3,985 Da) was dissolved in buffer (2 mL, 150 mM PBS, 100 mM NaCl, pH 7.2). To this solution, Sulfo-SMCC solution (89 µL, 0.88 mg, 8 eq., 100 % of the available lysine groups) suspended in DMF was added and the reaction was allowed to stir in the dark for 3 h. SMCC activated F3 peptide (122 µL, *ca*. 200 peptides per nanoparticle, 10 µmol/mL) was then added to a stirred solution of CB-SCK (6 mL, 0.235 mg/mL) suspended in buffer (100 mM PBS, 0.1 M NaCl, 10 mM EDTA, pH 7.4). The pH of the reaction was adjusted to 6.7 by the addition of 0.1 M citric acid buffer. The reaction was allowed to proceed for 6 h in the dark at room temperature, after which the reaction was quenched by the addition of 4-maleimido-butyric acid (0.3 mg, suspended in 100 mM PBS, 150 mM NaCl, pH 7.4). The solution was then allowed to stirred for additional 16 h before being transferred to a presoaked dialysis tubing (MWCO *ca*. 15 kDa) and dialyzed against aqueous buffer (5 mM PBS, 5 mM NaCl, pH 7.4) for 2 days. The conjugates were then purified on a 100 mL Sephadex-G75 medium gravity column eluting with aqueous buffer (150 mM PBS, 100 mM NaCl, pH 7.4). Nanoparticles conjugated with F3-peptide were collected and reconstituted to the original volume of 6 mL to give the F3-CB-SCK, **7**.

General procedure for doxorubicin (DOX) loading experiments into F3-CB-DOX-SCK nanoparticles, 8: To a vial containing a magnetic stir bar and F3-CB-SCK solution, **7** (5 mL, polymer concentration 0.24 mg/mL), a solution of DOX (0.5 mg/mL in $CHCl_3$ and 3 eq of triethylamine, 50 wt% with respect to the SCK) was added. The solution was shielded from light and stirred over-night before being transferred to a centrifugal filter device (Amicon Ultra 4, 100 kDa MWCO, Millipore corp., Billerica, MA, USA) and washed extensively with 5 mM pH 7.4 PBS at 37 °C to remove free DOX. The filtrate was analyzed by UV-Vis spectroscopy to confirm the removal of free DOX after several washing cycles. The DOX-nanoparticle solution was then reconstituted to a final volume of 5 mL with 5 mM pH 7.4 PBS buffer. The amount of DOX was determined by UV-vis spectroscopy (488 nm, $\varepsilon = 13{,}050\ M^{-1}cm^{-1}$ determined by a calibration curve in a 4:1 v/v mixture of DMF and DOX-nanoparticle in PBS).

Surface binding of FITC-labeled F3 peptide (FITC-F3) on U87MG glioma Cells by FACS analysis: Human glioma cell line (U87MG, *ca.* 10000 cells) were lifted and incubated with 10 µg/mL of FITC-labeled F3 peptide *in vitro* at 4 °C for 2 h before fixed in 70% ethanol and assayed by FACS analysis.

Cellular uptake of FITC-F3 and scramble F3 peptide (scramble-F3) in normal human astrocytes and human glioma cell line: Primary normal human astrocytes (NHA, SciCell) were cultured with astrocyte conditional media containing 10% FBS and astrocyte supplements. U87MG glioma cells were cultured in DMEM with 10% FBS. Approximately 3000 cells/well of NHA or U87MG cells were plated on 24 well coverslips and were incubated with 1 µM (final concentration) of either FITC-F3 or scrambled-F3 overnight at 37 °C. At the end of incubation, cells were first fixed with 4% paraformaldehyde (PFA) at room temperature for 15 minutes and mounted for microscopic observation. Nuclei were counterstained with 0.5 µg/mL of DAPI for 15 minutes.

***In vitro* cellular uptake of DOX loaded naked SCK (DOX-SCK) and F3-peptide conjugated DOX- loaded SCK (F3-DOX-SCK) in human glioma cell line:** NHA were cultured with astrocyte conditional media containing 10% FBS and astrocyte supplements. U87MG glioma cells were cultured in DMEM with 10% FBS and plated 24 hours before the experiment. DOX-SCK and F3-SCK were directly added into the cells at the same concentration (100 ng/mL). Cells were observed live 24 hours later with an inverted immunofluorescence microscope.

Cell viability assay by MTT: At the end of experiment, U87MG glioma cells that had been treated with naked SCK, DOX-SCK or F3-DOX-SCK, were incubated with MTT stock solution (10 µL of 5mg/mL of MTT solution added into one well in 96-well plate) for 3 hours at 37 °C. At the end of incubation cells were stopped with 10% SDS solution and the blue crystals were dissolved overnight and then the absorbance was read by spectrophotometry at 570 nm. Viability was normalized to the untreated control.

***In vivo* delivery of naked SCK and F3-SCK in U87MG xenograft tumors:** 1 x 10^6 of U87MG cells were injected into immunodeficient nude mice intracranially. When intracranial tumors were fully developed (normally around 3-4 weeks post injection), mice were injected with naked SCK or F3-SCK by tail vein. An intracardiac perfusion was performed on these mice 24 hours later, first with PBS and then with 4% PFA before all internal organs were harvested. All tissues were fixed in 4% PFA overnight and paraffin-embedded sections were used for immunostaining. For the immuno-detection of SCKs, all the tissue sections were stained with anti-cascade blue antibody by ABC method and cellular nuclei were counterstained by hematoxylin for observations.

7.3. Results and discussion

The multi-functional SCK nanoparticles were prepared from previously reported PAA$_{120}$-*b*-PS$_{100}$ amphiphilic block copolymers, through aqueous micellization and further covalent crosslinking and chemical modification reactions. Water (a selective solvent for the PAA block segment) was introduced to a THF (a good solvent for both PAA and PS) solution of the block copolymer dropwise *via* a syringe pump to form discrete spherical micelles. The PAA shell regions of these micelles were then crosslinked *via* amidation chemistry with 2,2′-(ethylenedioxy)bis(ethylamine) (EDDA), as a diamine crosslinker, in the presence of 1-[3′-(dimethylamino)propyl]-3-

ethylcarbodiimide methiodide (EDCI) to afford SCK nanoparticles. 5-FITC cadaverine was attached through additional amidation chemistry using the coupling agent EDCI, rendering the SCKs fluorescent, to facilitate *in vitro* tracking of SCKs during functional studies (Figure 7.1). The conjugation of the targeting ligand $\mathrm{FimH_A}$ was then accomplished by non-selective reaction between any of the four lysine residues on $\mathrm{FimH_A}$ and residual carboxylic acids on the SCK surface, following a previously established method. The reaction was carried out by first lowering the pH of the SCK solution in nanopure water to 5 with acetic acid and incubating at 4 °C for 30 minutes. Addition of sulfonated *N*-hydroxysuccinimide and coupling agent EDCI followed, and the reaction mixture was then allowed to stir at 4 °C for another 30 minutes before the pH of the solution was adjusted to 7-8 by addition of sodium phosphate. $\mathrm{FimH_A}$ (0.65 mg/mL in PBS, pH 7.4) was added to the reaction solution slowly, and the conjugation process was allowed to proceed for 24 h at 4 °C. Purification by extensive washing using a centrifugal filtration device (MWCO 100 kDa) with PBS solution was performed to remove $\mathrm{FimH_A}$ that was not associated with the nanoparticles. Including lower concentrations of $\mathrm{FimH_A}$ gave less efficient functionalization, as judged by the analytical methods detailed below. The final products were characterized physicochemically to determine their sizes, compositions and structures, and the effects of $\mathrm{FimH_A}$ conjugation on their biological behaviors were evaluated.

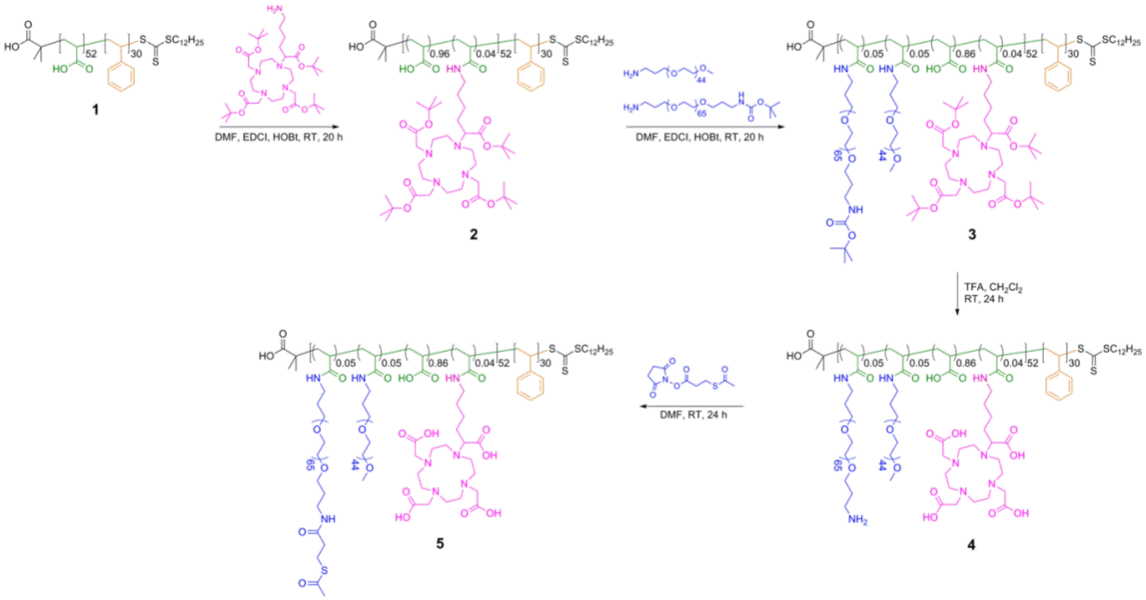

Figure 7.1. Schematic representation of synthesis of DOTA containing PEGylated PAA$_{52}$-*b*-PS$_{30}$ with activated ester-functionalized PEG, PAA$_{45}$-*g*-(CONH-lysine-DOTA-COOH)$_3$-*g*-(CONH-PEG$_{3kDa}$-NHCO-C$_3$H$_6$-SCOCH$_3$)$_2$-*g*-(CONH-PEG$_{2kDa}$-OMe)$_2$-*b*-PS$_{30}$.

The F3-peptide-, cascade blue (CB)-conjugated SCKs (F3-CB-SCK **7**) were modified from naked SCK **6**, constructed from polymer precursor **5**, through aqueous self assembly. Aqueous micellization methodology was adopted to prepare spherical micelles, where block copolymer precursors were dissolved in organic solvent DMF (1 mg/mL) and an equal amount of water was added to the solution drop-wise *via* a syringe pump over a period of 3 h to induce self assembly. The micelles were crosslinked in the PAA shell regions *via* amidation chemistry with 2,2’-(ethylenedioxy)bis(ethylamine), as the diamine crosslinker, in the presence of 1-[3’-(dimethylamino)propyl]-3-ethylcarbodiimide methiodide (EDCI), resulting stable SCK nanoparticles. To allow for immunofluorescence labeling, the PAA shell of the SCKs was conjugated with the chromophore cascade blue (CB) by using sulfonated *N*-hydroxysuccinimide ester as a coupling agent to yield CB-SCK **6** (Figure 7.2). The protected sulfohydryl groups on the PEG$_{3k}$ chains on the SCKs allowed the nanoparticles to maintain storage stability and also introduced surface functionality to conjugate with maleimido functionalized moieties such as peptides and antibodies. The methylester protecting groups on the PEG spacer were removed by treatment with hydroxylamine (0.5 M) in buffer (100 mM PBS, 0.1 M NaCl, 10 mM EDTA, pH 7.4) to expose active -SH groups (the concentration of -SH groups was determined by Ellman's essay in solution to be 100 ± 5 µM, theoretical concentration was 120 µM). Deprotected SCKs with active -SH groups were then conjugated with maleimido-functionalized F3-peptide that had been modified with sulfosuccinimidyl-4-(*N*-maleimidomethyl)cyclohexane-1-carboxylate (Sulfo-SMCC). Free –SH groups were capped by reacting with an excess amount of maleimido butyric acid. F3-CB-SCK **7** was purified with Sephadex G75 gel chromatography column, and the removal of unconjugated peptide and dye was confirmed by fast protein liquid chromatography (FPLC).

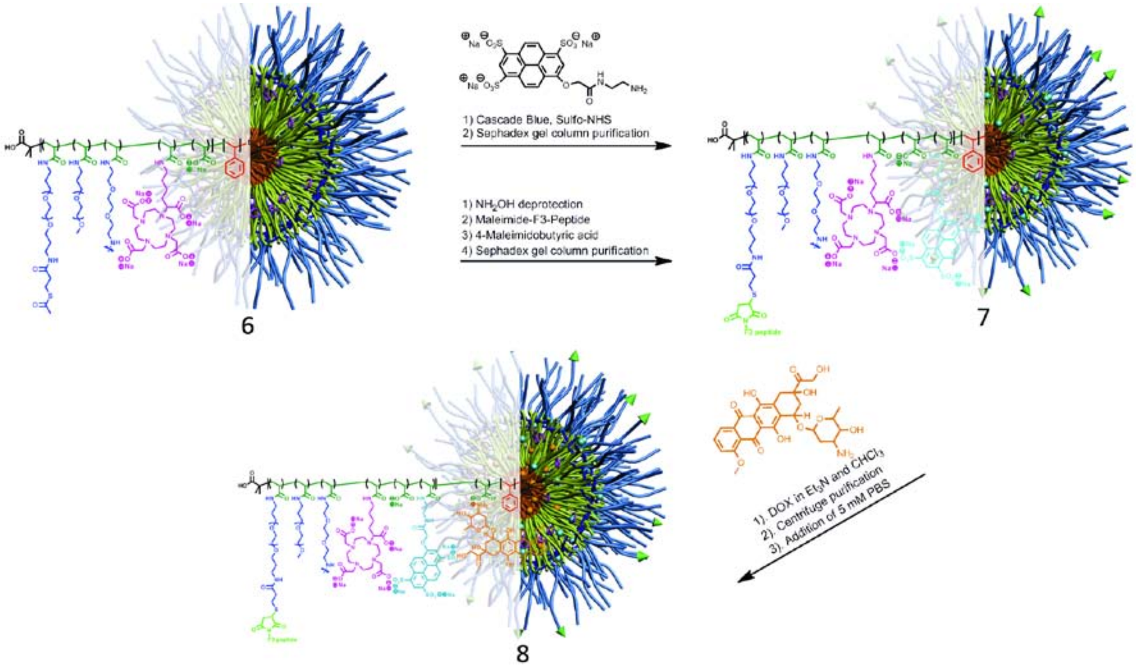

Figure 7.2. Schematic representation of incorporation of cascade blue dye with sulfo-NHS onto the polymer backbone segments within the shell of the SCKs, conjugation of maleimide-functionalized F3 peptide onto the thiol functionalized PEG graft termini to produce F3-CB-SCK **7**, followed by encapsulation of DOX into the nanoparticles through physical encapsulation to produce F3-CB-DOX-SCK **8**.

F3-CB-SCK **7** nanoparticles can also encapsulate therapeutic agents such as DOX for active drug delivery. The incorporation of DOX into the targeted SCK nanoparticles was accomplished by incubating DOX solutions in DMF with SCK nanoparticles in aqueous solutions. The polystyrene core was swollen with the addition of the organic solvent DMF and provided a large hydrophobic reservoir to encapsulate DOX and drive the diffusion-controlled loading/encapsulation process. The unincorporated DOX molecules were purified from the DOX-loaded SCK nanoparticles by centrifugation and extensive washing using a centrifugal-filtration membrane device with PBS (5 mM, with 5 mM NaCl). The F3-peptide-, cascade blue-conjugated, DOX-loaded SCK nanoparticle **8** (F3-CB-DOX-SCK **8**) solution was reconstituted to its original concentration by the addition of PBS, and the resulting DOX concentrations (0.028 mg/mL) in the SCKs were determined using the absorption of DOX at 488 nm.

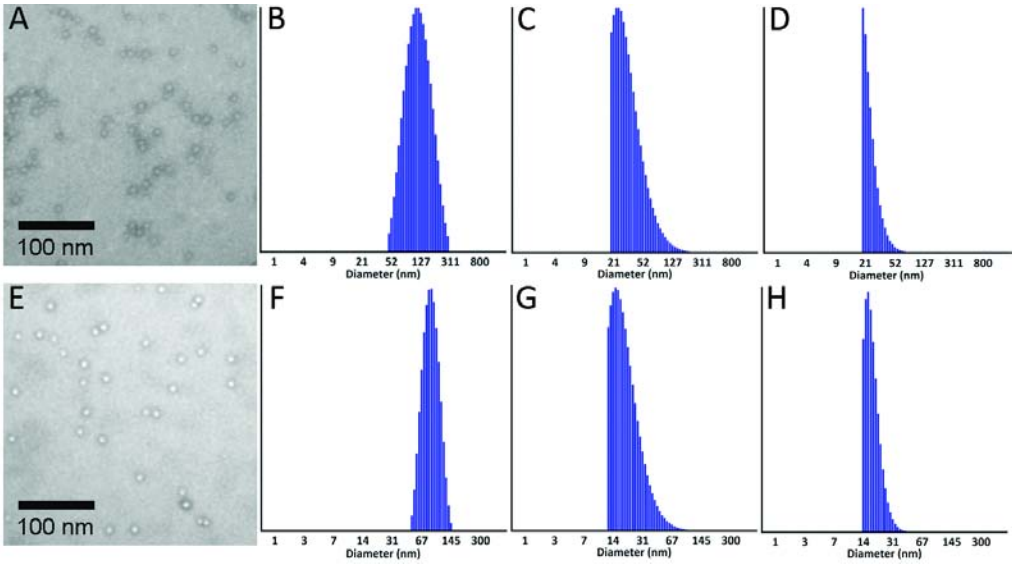

Figure 7.3. Upper row: A. TEM image (drop deposited on carbon-coated copper grids and stained negatively with 1% aqueous uranyl acetate) of SCK, diameter = 8 ± 3 nm; DLS histograms (determinations were average values from ten measurements, with the standard deviations being calculated as the breadth of the distributions) of B. SCK intensity average, 130 ± 60 nm; C. SCK volume average, 40 ± 20 nm; D. SCK number average 26 ± 6 nm; Lower row: E. TEM image of F3-CB-DOX-SCK, diameter = 7 ± 3 nm; DLS histograms of F. F3-CB-DOX-SCK intensity average, 100 ± 70 nm; G. F3-CB-DOX-SCK volume average, 30 ± 10 nm; H. F3-CB-DOX-SCK number average, 21 ± 4 nm.

The dimensions of F3-CB-DOX–SCK **8** nanoparticles were characterized by transmission electron microscopy (TEM) and dynamic light scattering (DLS) (Figure 7.3). As a comparison, non-conjugated SCKs were also characterized. The well-defined, circularly-shaped images observed by TEM suggested that the empty SCKs were spherical with a narrow size distribution of 8 ± 3 nm (Figure 7.3). After F3-peptide conjugation and DOX encapsulation, the SCKs retained the spherical morphology with a comparable size distribution of 7 ± 2 nm, indicating that the peptide conjugation and the drug loading did not affect the size or the shape of the SCKs. The dry-state core diameter of F3-CB-DOX-SCK **8** was about the same as non-conjugated SCKs, as measured by TEM. Their hydrodynamic diameters were also similar with a narrow distribution, as confirmed by DLS measurements.

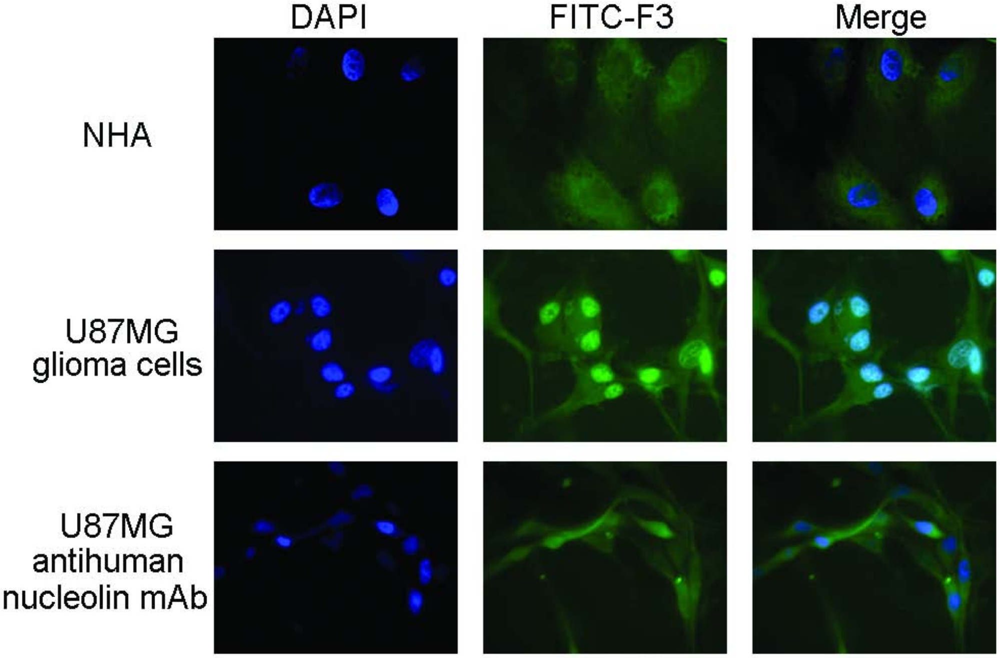

Figure 7.4. Cellular uptake of FITC labeled F3 peptide in primary normal human astrocytes (NHA) and U87MG glioma cells. Primary normal human astrocytes and U87MG glioma cells were both incubated with FITC-labeled F3 peptide (1µM) at 37 °C for 2 h before fixed with 4% PFA and then mounted for observation. As a control, U87MG glioma cells were pre-incubated with anti-human specific nucleolin antibody (10µg/ml) to block the binding. The nuclei were counterstained with DAPI.

To test the hypothesis that F3 peptide preferentially targeted tumor cells compared to scramble-peptide, we utilized two model cell line systems: normal human astrocytes (NHA) and a human glioma cell line (U87MG). Previously, we found that U87MG glioma cells demonstrated significant amount of nucleolin expression both within their nucleolus and on their cell surface compared to normal human astrocytes.

As expected, U87MG glioma cells showed significant uptake of FITC-labeled F3 peptide within their nuclei whereas the amount of FITC-F3 peptide within normal human astrocytes was essentially negligible (Figure 7.4). Likewise, neither NHA nor U87MG cells showed any significant uptake of FITC-labeled scrambled peptide.

We observed that non-targeted naked SCKs (DOX-SCKs) were preferentially being taken up into lysosomal structures and/or the peri-nuclear region among the treated cells, although currently the cellular mechanism of uptake for these SCKs is still unknown. Lysosome localization of SCKs especially with DOX-SCKs among treated cells may potentially attenuate their anti-tumor effects with this system. By conjugating with F3-peptide, which showed specific nuclear targeting in U87MG glioma cells, we hypothesized that there would be enhanced nuclear delivery of DOX by F3-peptide conjugated SCKs compared to naked SCKs. As shown in Figure 7.5, U87MG cells treated with F3-DOX-SCKs indeed had more DOX within their nuclei compared to naked SCKs. Even though free DOX also accumulated within the nuclei of treated cells *in vitro*, the advantage of tumor specific delivery by the F3-peptide conjugated SCKs may potentially lower the dosage of DOX that is needed for killing the tumors and therefore help to prevent systemic side effects observed *in vivo* by free DOX (Figure 7.6).

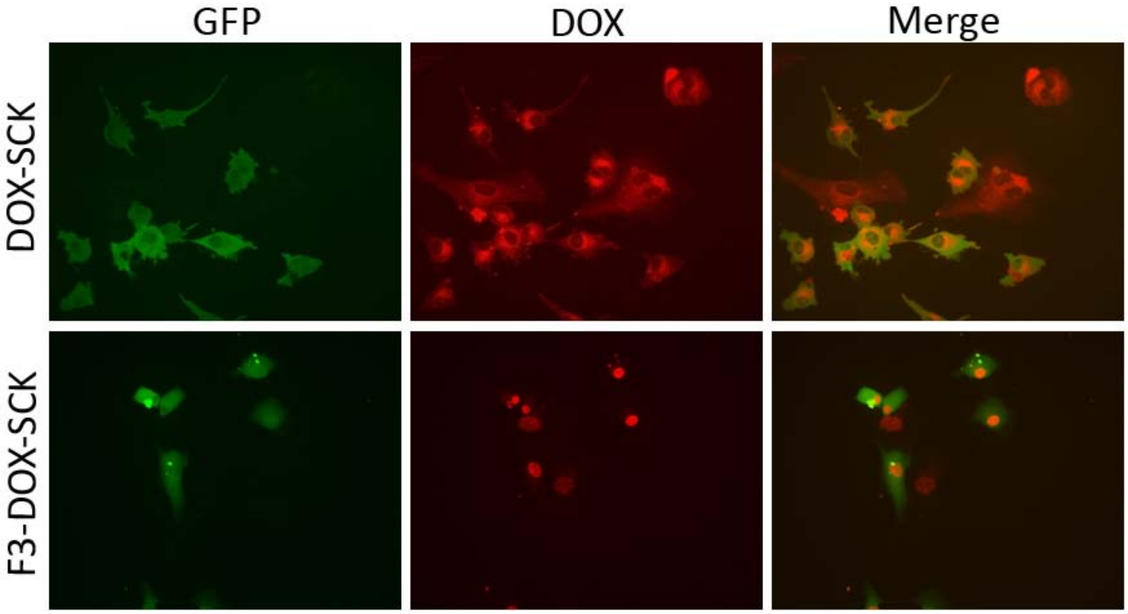

Figure 7.5. Live cell imaging of cellular uptake of untargeted DOX-loaded (DOX-SCK) *vs.* targeted DOX-loaded (F3-DOX-SCK) nanoparticles (at 1 µg/mL x 1 h) into U87MG glioma cells, 20 x magnifications. DOX molecules were shown by intrinsic red fluorescence within the treated cells.

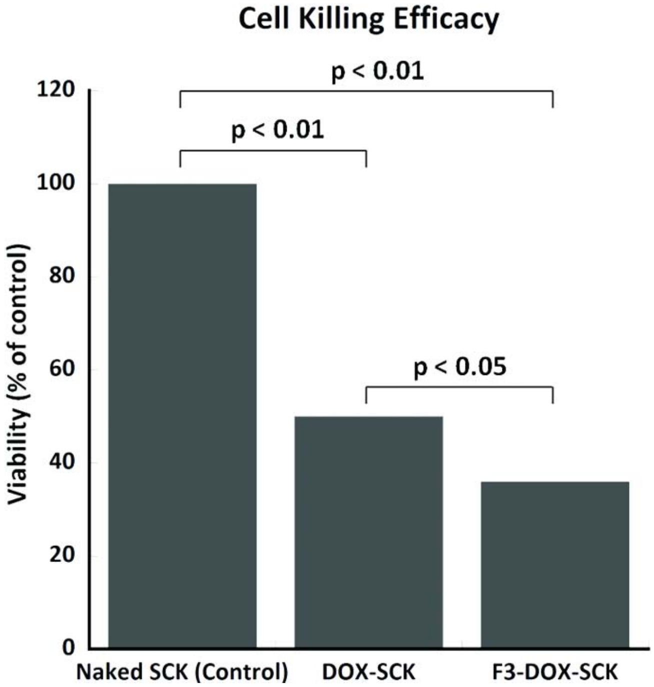

Figure 7.6. Enhanced tumor cell killing effects by F3-DOX-SCK nanoparticle *in vitro* compared with non-targeted SCKs. U87MG glioma cells were treated with naked SCK, DOX-SCK or F3-DOX-SCK for 3 days before assayed for their viability by MTT assay.

To further validate the hypothesis that F3-CB-DOX-SCKs specifically target tumor cells *in vivo* and to investigate the differences of bio-distribution between untargeted SCKs and targeted SCKs, we generated immunodeficient mice bearing intracranial U87MG glioma cells (Figure 7.7). Three to four weeks after tumor implantation, we systemically delivered F3-CB-DOX-SCKs by tail vein injection and subsequently harvested the internal organs including the tumor-bearing mouse brains. To demonstrate cellular localization of targeted SCKs, we used a specific antibody against cascade blue, which was also incorporated into SCKs as a fluorescent label. F3-CB-DOX-SCKs and CB-DOX-SCKs were clearly detected in heart, kidney, liver, and brain tumor tissues. In general, staining was more intense in heart, kidney, and liver in the CB-DOX-SCK treated group, indicating greater system distribution in untargeted SCKs. F3-CD-DOX-SCK treated animals showed greater staining within tumors compared to tumors from untargeted SCKs-treated animals. Both *in vitro* results and *in vivo* tumor specific targeting ability of our F3-peptide conjugated SCKs in U87MG xenograft animals demonstrated a feasibility and clear advantage of the current therapeutic systems as a novel treatment of malignant gliomas. We are currently testing the long-term anti-tumor effects from F3-CB-DOX-SCKs on U87MG xenograft animals.

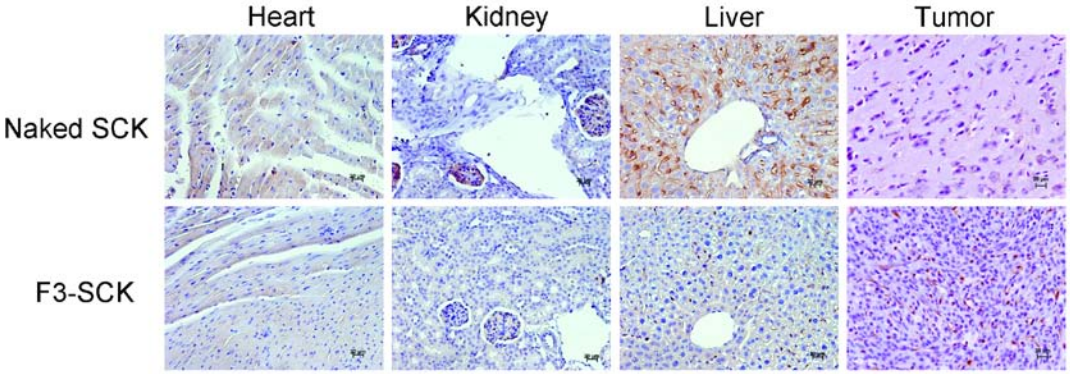

Figure 7.7. Enhanced tumor specific delivery of targeted nanoparticle in U87MG intracranial xenograft *in vivo* of targeted nanoparticles, F3-CB-DOX-SCK, compared with systemic distribution with non-targeted nanoparticles, CB-DOX-SCK, especially within the heart, kidney and liver.

7.4. Conclusions

In this study, multifunctional SCK nanoparticles were conjugated with F3-peptide and physically loaded with DOX to actively deliver the therapeutic payload for the potential treatment of glioblastoma and were able to successfully achieve nuclear localization of the DOX *in vitro* and enhanced uptake into U87MG intracranial xenografts *in vivo*. Compared with non-targeted SCKs, which accumulated mostly in the peri-nuclear region, enhanced nuclear delivery of DOX was observed with F3-peptide conjugated SCKs, resulting in higher killing abilities against U87MG cells *in vitro* compared with the non-targeted analogue. In addition, systemic distribution throughout the heart, kidney and liver was observed with non-targeted SCKs, whereas enhanced tumor uptake was observed with targeted SCKs *in vivo.* We were able to utilize fully the multi-functionality of the SCK nanoparticle system to introduce targeting ligands, imaging moieties and PEG corona layer with facile control over the number of each entity, tailored to maximize the EPR effect and therapeutic efficacy through both passive and active targeting.

7.5. Acknowledgements

This material is based upon work supported by The Children’s Discovery Institute of St. Louis Children’s Hospital and Washington University School of Medicine, and the National Heart, Lung and Blood Institute of the National Institutes of Health as a Program of Excellence in Nanotechnology (HHSN268201000046C). Postdoctoral and assistant professor fellowship provided by the Knut and Alice

Wallenberg Foundation is gratefully acknowledged (A.M.N), as well as financial support from Åke Wibergs foundation, Karolinska Institutet, The Swedish Medical Nanoscience Center, Carl Bennet AB, and Vinnova, Axel and Eva Wallströms foundation, and Jeanssons foundation, are also gratefully acknowledged.

CHAPTER VIII

CONCLUSIONS

Shell crosslinked knedel-like nanoparticles (SCKs) are promising drug delivery platforms in biomedical applications as the treatment of a wide range of diseases. The construction of SCKs involves the supramolecular assembly of amphiphilic block copolymers into micelles with core-shell morphology, followed by regioselective crosslinking throughout the peripheral region to impart the robustness of the nanoparticles. The engineering of multifunctional SCK nanoparticles with precise control over composition, dimension, structure, morphology, external surface chemistry and functionalization has benefited from the advances in polymerization chemistries and the application of efficient and orthogonal chemical modification. The careful design and control over these properties of the SCKs will enable their future development and application as the next generation nanomaterials. In this dissertation, nanoparticle-based drug delivery system was designed and developed for the treatment of cancer, urinary tract infection, lung infection associated with cystic fibrosis and pediatric brain cancer through compositional, dimensional and structural control.

In an effort to understand how the dimension of a nanoparticle, specifically the core volume and shell thickness, can affect their performance as drug delivery vehicles in drug loading and release characteristics, SCK nanoparticles were designed to have various relative and absolute core and shell dimensions to mediate the packaging and release of DOX as a model chemotherapeutic system. Variation over the nanoparticle dimensions was achieved through controlling of the block copolymer precursor chain lengths, to afford a series of well-defined and rigorously characterized nanoscopic vessels for drug molecule loading and release studies. The nanoparticles were constructed from amphiphilic block copolymer poly(acrylic acid)-*block*-polystyrene (PAA-*b*-PS). PAA-*b*-PS block copolymers having different relative block lengths and absolute chain lengths were synthesized *via* sequential reversible addition-fragmentation chain transfer (RAFT) polymerization reactions of *t*-butyl acrylate (*t*BA) and styrene, followed by removal of the *t*-butyl ester protecting groups. The amphiphilic core-shell morphology of the SCK nanostructures provided opportunities for tuning of the drug loading capacities and rates of release. Increasing core diameters and core-shell interfacial surface areas were important for superior guest packaging capacity while lower proportions of shell-to-core volume was the critical parameter for increased kinetics of release. The variety of contributing factors, including chemical composition, dimensions of the core and shell domains and total particle concentrations, made direct determination of the effects of each parameter complicated, although the greatest correlation appeared to be the ratio of the volume of the shell *vs*. the volume of the core. As the relative proportion of PAA shell to PS core volumes decreased, the rate and extent of release increased. These studies, therefore, point to future directions to craft sophisticated devices for controlled drug release.

Continuous efforts were made towards understanding whether or not dimension of the nanoparticle would affect their therapeutic performance *in vitro*. Paclitaxel (PTX), another chemotherapy drug was encapsulated into functional nanoparticles with varying sizes and surface characteristics, all of which demonstrated cell killing abilities that were comparable to or better than free PTX. The size variations in nanoparticles did not result in any significant differentiation in cell killing. In addition, incorporation polyethylene glycol (PEG), which imparts the stealthiness of the nanoparticle, did not affect PTX-loaded SCKs performance *in vitro*. Conjugation of targeting ligands onto the PEG termini or to the PAA chains is expected to further enhance the ability of the overall nanoparticle system to actively target for increased potency. Future studies also include utilization of degradable core or shell units for bioclearance of the nanoparticle upon delivery.

The well-defined SCK nanoparticles were explored as novel antimicrobial agents nanocarriers for the treatment of *Pseudomonas aeruginosa* bacteria caused lung infections associated with cystic fibrosis. The hydrophobic core of the SCK nanoparticles was able to encapsulate novel silver carbene complexes, while the acrylic acid residue on the hydrophilic shell could complex to silver cation moieties. The silver concentrations were determined by inductively coupled plasma mass spectrometry (ICP-MS) and the location of different silver species was revealed by high resolution scanning transmission microscopy (STEM) coupled with energy dispersive X-ray spectroscopy (EDX). The *in vivo* efficacy was investigated by nebuilization treatment in *Pseudomonas aeruginosa* bacteria inoculated mice models to reveal that high therapeutic efficacy was achieved through localization of the silver moieties by the nanoparticles. Targeted delivery of antimicrobial could be achieved with conjugation of targeting ligands onto the surface of these silver loaded SCK nanoparticles resulting in higher therapeutic efficacy.

Next, we demonstrated the feasibility of leveraging a known bacterial-host interaction to direct nanostructures to an epithelial cell surface for potential therapeutic use. Amphiphilic block copolymer nanoparticles were conjugated with uropathogenic *Escherichia coli* type 1 pilus adhesin $\mathrm{FimH_A}$ through amidation chemistry to enable bladder epithelial cell binding and internalization of the nanoparticles *in vitro* thus emulating the bacteria mode of invasion. By fluorescence microscopy the association of SCKs with the cell surfaces was shown to be dose dependent, $\mathrm{FimH_A}$ specific and inhibited by addition of mannose to the medium. Combination of incorporation of antimicrobial agents and conjugation with targeting ligand could allow these SCK nanoparticles to be served as powerful theranostics and play an important role in the prevention and treatment of various infection diseases.

Nanoscale assemblies with complex morphologies have been applied as potential biomedical devices and considerable efforts have been devoted to understanding and manipulating the aqueous self assembly process of amphiphilic block copolymers to obtain theses complex morphologies. As a fundamental study, the construction of both cylindrical and multicompartment nanostructure (MCN) with a single type of linear triblock copolymer, $\mathrm{PEO_{45}}$-b-$\mathrm{PNAS_{66}}$-b-$\mathrm{PS_{30}}$ was investigated and their dynamic disembodiment into individual spherical nanoparticles and retention of morphology through shell crosslinking were observed. The formation of these intricate morphologies, from facile process manipulation of a triblock copolymer, coupled with unique properties, is certainly interesting in biomedical applications.

SCK nanoparticles hold great promise as versatile nanocarriers for a wide range of therapeutics in the diagnosis and treatment of a variety of diseases. In this dissertation, the ease of control over size, shape, composition, structure, surface characteristics and morphology of the SCK nanoparticles was achieved through advanced polymerization techniques, facile and practical chemical manipulations, and control over the supramolecular assembly process, which will secure their future development and success in the biomedical and nanomedicine field.

We have designed and developed a highly multifunctional nanodevice for imaging and therapeutic delivery, functionalized with a chelator for radio-labeling, a chromophore for visualization, polyethylene glycol for improved biodistribution, targeting peptides to redirect biodistribution, and a therapeutic agent for treatment of pediatric glioblastomas. This complex yet sophisticated system, employed the combination of passive targeting with control over the size of the nanoparticle through advanced polymerization techniques, and active targeting with chemical manipulation and functionalization utilizing a targeting peptide, was able to achieve high *in vitro* therapeutic performance and *in vivo* tumor specific targeting. However, there are still parameters that need to be optimized in order to perfect the therapeutic performances SCK nanoparticles and achieve efficacy as natural systems. For example, while some active agents, such as DOX, have the tendency to be prematurely diffused out of the nanoparticles and being released before they reach the desired location, other payloads, including PTX, will not release even over an extended period of time and need degradation triggered release to achieve high therapeutic performance. Other therapeutic cargos, such as silver, if released early in the blood stream, precipitation issue can become problematic, and the loss of its active form will lower its therapeutic performance. Thus, the development to balance the nanoparticle as a robust and stable drug delivery vehicle but also incorporating stimuli-responsive degradation to allow triggered release still remains as a challenge.

There are other factors related to these synthetic nanoparticles' performance and parameters that need to be optimized to allow them to be as efficient as natural systems. For instance, challenges towards optimizing the coupling chemistry used to efficiently introduce the targeting ligands still exist. Once the targeting ligands are conjugated onto the nanoparticle system, quantification and their surface accessibility and bioavailability must be further looked into. Other considerations such as physical, chemical and biological evaluations of the nanoparticle systems, their immunological reaction and toxicity need to be addressed with a combined effort of scientists from all fields, which create exciting opportunities for collaboration and interdisciplinary research.

REFERENCES

(1) Wagner, V.; Dullaart, A.; Bock, A.; Zweck, A. *Nat. Biotech.* **2006**, *24*, 1211.

(2) Zhang, L.; Gu, F. X.; Chan, J. M.; Wang, A. Z.; Langer, R. S.; Farokhzad, O. C. *Clin. Pharmacol. Ther.* **2008**, *83*, 761.

(3) Elsabahy, M.; Wooley, K. L. *Chem. Soc. Rev.* **in press**.

(4) Wooley, K. L. *J. Polym. Sci., Part A: Polym. Chem.* **2000**, *38*, 1397.

(5) Kataoka, K.; Kwon, G. S.; Yokoyama, M.; Okano, T.; Sakurai, Y. *J. Controlled Release* **1993**, *24*, 119.

(6) Cho, K. J.; Wang, X.; Nie, S. M.; Chen, Z.; Shin, D. M. *Clin. Cancer Res.* **2008**, *14*, 1310.

(7) Langer, R. *Science* **1990**, *249*, 1527.

(8) Carrico, Z. M.; Romanini, D. W.; Mehl, R. A.; Francis, M. B. *Chem. Commun.* **2008**, 1205.

(9) Schlick, T. L.; Ding, Z. B.; Kovacs, E. W.; Francis, M. B. *J. Am. Chem. Soc.* **2005**, *127*, 3718.

(10) Hooker, J. M.; Kovacs, E. W.; Francis, M. B. *J. Am. Chem. Soc.* **2004**, *126*, 3718.

(11) Le Droumaguet, C.; Wang, C.; Wang, Q. *Chem. Soc. Rev.* **2010**, *39*, 1233.

(12) Li, K.; Nguyen, H. G.; Lu, X. B.; Wang, Q. *Analyst* **2010**, *135*, 21.

(13) Destito, G.; Yeh, R.; Rae, C. S.; Finn, M. G.; Manchester, M. *Chem. Biol.* **2007**, *14*, 1152.

(14) Koudelka, K. J.; Destito, G.; Plummer, E. M.; Trauger, S. A.; Siuzdak, G.; Manchester, M. *PLoS Pathog.* **2009**, *5*, 10.

(15) Strable, E.; Finn, M. G. In *Viruses and Nanotechnology*; Springer-Verlag Berlin: Berlin, 2009; Vol. 327, p 1.

(16) Iha, R. K.; Wooley, K. L.; Nystrom, A. M.; Burke, D. J.; Kade, M. J.; Hawker, C. J. *Chem. Rev.* **2009**, *109*, 5620.

(17) Henselwood, F.; Liu, G. J. *Macromolecules* **1997**, *30*, 488.

(18) Kataoka, K.; Harada, A.; Nagasaki, Y. *Adv. Drug Deliv. Rev.* **2001**, *47*, 113.

(19) Freiberg, S.; Zhu, X. *Int. J. Pharm.* **2004**, *282*, 1.

(20) Kabanov, A. V.; Batrakova, E. V.; Alakhov, V. Y. *Adv. Drug Deliv. Rev.* **2002**, *54*, 759.

(21) Kabanov, A. V.; Batrakova, E. V.; Alakhov, V. Y. *J. Controlled Release* **2002**, *82*, 189.

(22) Gref, R.; Minamitake, Y.; Peracchia, M. T.; Trubetskoy, V.; Torchilin, V.; Langer, R. *Science* **1994**, *263,* 1600.

(23) Moghimi, S. M.; Hunter, A. C.; Murray, J. C. *Pharmacol. Rev.* **2001**, *53*, 283.

(24) Lee, N. S.; Li, Y. L.; Ruda, C. M.; Wooley, K. L. *Chem. Commun.* **2008**, 5339.

(25) Adams, M. L.; Lavasanifar, A.; Kwon, G. S. *J. Pharm. Sci.* **2003**, *92*, 1343.

(26) Lee, A. S.; Gast, A. P.; Butun, V.; Armes, S. P. *Macromolecules* **1999**, *32*, 4302.

(27) Sumerlin, B. S.; Lowe, A. B.; Thomas, D. B.; McCormick, C. L. *Macromolecules* **2003**, *36*, 5982.

(28) Khougaz, K.; Gao, Z. S.; Esienberg, A. *Macromolecules* **1994**, *27*, 6341.

(29) Kabanov, A. V.; Bronich, T. K.; Kabanov, V. A.; Yu, K.; Eisenberg, A. *Macromolecules* **1996**, *29*, 6797.

(30) Astafieva, I.; Khougaz, K.; Eisenberg, A. *Macromolecules* **1995**, *28*, 7127.

(31) Choucair, A.; Soo, P. L.; Eisenberg, A. *Langmuir* **2005**, *21*, 9308.

(32) O'Reilly, R. K.; Hawker, C. J.; Wooley, K. L. *Chem. Soc. Rev.* **2006**, *35*, 1068.

(33) Thurmond, K. B.; Kowalewski, T.; Wooley, K. L. *J. Am. Chem. Soc.* **1996**, *118*, 7239.

(34) Thurmond, K. B.; Kowalewski, T.; Wooley, K. L. *J. Am. Chem. Soc.* **1997**, *119*, 6656.

(35) Baugher, A. H.; Goetz, J. M.; McDowell, L. M.; Huang, H. Y.; Wooley, K. L.; Schaefer, J. *Biophys. J.* **1998**, *75*, 2574.

(36) Kao, H. M.; O'Connor, R. D.; Mehta, A. K.; Huang, H. Y.; Poliks, B.; Wooley, K. L.; Schaefer, J. *Macromolecules* **2001**, *34*, 544.

(37) Kao, H. M.; Stefanescu, A. D.; Wooley, K. L.; Schaefer, J. *Macromolecules* **2000**, *33*, 6214.

(38) Elsabahy, M.; Wooley, K. L. *J. Polym. Sci., Part A: Polym. Chem.* **in press**.

(39) Lin, L. Y.; Lee, N. S.; Zhu, J.; Nyström, A. M.; Pochan, D. J.; Dorshow, R. B.; Wooley, K. L. *J. Controlled Release* **2011**, *152*, 37.

(40) Sun, G.; Hagooly, A.; Xu, J.; Nystrom, A. M.; Li, Z. C.; Rossin, R.; Moore, D. A.; Wooley, K. L.; Welch, M. J. *Biomacromolecules* **2008**, *9*, 1997.

(41) Engin, K.; Leeper, D. B.; Cater, J. R.; Thistlethwaite, A. J.; Tupchong, L.; McFarlane, J. D. *Int. J. Hyperthermia* **1995**, *11*, 211.

(42) Jain, R. *Biomaterials* **2000**, *21*, 2475.

(43) Jain, R. A.; Shah, N. H.; Malick, A. W.; Rhodes, C. T. *Drug Dev. Ind. Pharm.* **1998**, *24*, 703.

(44) Heller, J.; Himmelstein, K. J. *Methods Enzymol.* **1985**, *112*, 422.

(45) Gopferich, A.; Alonso, M. J.; Langer, R. *Pharm. Res.* **1994**, *11*, 1568.

(46) Arshady, R. *J. Controlled Release* **1991**, *17*, 1.

(47) Zweers, M. L. T.; Grijpma, D. W.; Engbers, G. H. M.; Feijen, J. *J. Biomed. Mater. Res. Part B* **2003**, *66B*, 559.

(48) Kalarickal, N. C.; Rimmer, S.; Sarker, P.; Leroux, J. C. *Macromolecules* **2007**, *40*, 1874.

(49) Lele, B. S.; Leroux, J. C. *Macromolecules* **2002**, *35*, 6714.

(50) Acharya, G.; Shin, C. S.; Vedantham, K.; McDermott, M.; Rish, T.; Hansen, K.; Fu, Y.; Park, K. *J. Controlled Release* **2010**, *146*, 201.

(51) Davis, K. A.; Anseth, K. S. *Crit. Rev. Ther. Drug Carrier Syst.* **2002**, *19*, 385.

(52) Murthy, K. S.; Ma, Q. G.; Clark, C. G.; Remsen, E. E.; Wooley, K. L. *Chem. Commun.* **2001**, 773.

(53) Nyström, A. M.; Xu, Z. Q.; Xu, J. Q.; Taylor, S.; Nittis, T.; Stewart, S. A.; Leonard, J.; Wooley, K. L. *Chem. Commun.* **2008**, 3579.

(54) Nystrom, A. M.; Wooley, K. L. *Soft Matter* **2008**, *4*, 849.

(55) Kline, S. R. *J. Appl. Crystallogr.* **2006**, *39*, 895.

(56) Vo, C. D.; Rosselgong, J.; Armes, S. P.; Tirelli, N. *J. Polym. Sci., Part A: Polym. Chem.* **2010**, *48*, 2032.

(57) Schumers, J. M.; Fustin, C. A.; Can, A.; Hoogenboom, R.; Schubert, U. S.; Gohy, J. F. *J. Polym. Sci., Part A: Polym. Chem.* **2009**, *47*, 6504.

(58) O'Donnell, J. M.; Kaler, E. W. *J. Polym. Sci., Part A: Polym. Chem.* **2010**, *48*, 604.

(59) Luzon, M.; Boyer, C.; Peinado, C.; Corrales, T.; Whittaker, M.; Tao, L.; Davis, T. P. *J. Polym. Sci., Part A: Polym. Chem.* **2010**, *48*, 2783.

(60) Kakwere, H.; Perrier, S. *J. Polym. Sci., Part A: Polym. Chem.* **2009**, *47*, 6396.

(61) Gibson, M. I.; Froehlich, E.; Klok, H. A. *J. Polym. Sci., Part A: Polym. Chem.* **2009**, *47*, 4332.

(62) Boyer, C.; Granville, A.; Davis, T. P.; Bulmus, V. *J. Polym. Sci., Part A: Polym. Chem.* **2009**, *47*, 3773.

(63) Alidedeoglu, A. H.; York, A. W.; McCormick, C. L.; Morgan, S. E. *J. Polym. Sci., Part A: Polym. Chem.* **2009**, *47*, 5405.

(64) Perrier, S.; Takolpuckdee, P. *J. Polym. Sci., Part A: Polym. Chem.* **2005**, *43*, 5347.

(65) Bousquet, A.; Barner-Kowollik, C.; Stenzel, M. H. *J. Polym. Sci., Part A: Polym. Chem.* **2010**, *48*, 1773.

(66) Tian, Y.; Bromberg, L.; Lin, S. N.; Hatton, T. A.; Tam, K. C. *J. Controlled Release* **2007**, *121*, 137.

(67) Gillies, E. R.; Frechet, J. M. J. *Bioconjugate Chem.* **2005**, *16*, 361.

(68) Sturgeon, R. J.; Schulman, S. G. *J. Pharm. Sci.* **1977**, *66*, 958.

(69) Brophy, M. R.; Deasy, P. B. *Int. J. Pharm.* **1987**, *37*, 41.

(70) Higuchi, T. *J. Pharm. Sci.* **1963**, *52*, 1145.

(71) Serra, L.; Domenech, J.; Peppas, N. A. *Biomaterials* **2006**, *27*, 5440.

(72) Costa, F. O.; Sousa, J. J. S.; Pais, A.; Formosinho, S. J. *J. Controlled Release* **2003**, *89*, 199.

(73) Moore, J. W.; Flanner, H. H. *Pharm. Tech.* **1996**, *20*, 67.

(74) Bollag, D. M.; McQueney, P. A.; Zhu, J.; Hensens, O.; Koupal, L.; Liesch, J.; Goetz, M.; Lazarides, E.; Woods, C. M. *Cancer Res.* **1995**, *55*, 2325.

(75) Brannon-Peppas, L.; Blanchette, J. O. *Adv. Drug Deliv. Rev.* **2004**, *56*, 1649.

(76) Kratz, F. *J. Controlled Release* **2008**, *132*, 171.

(77) Shin, H.; Alani, A. W. G.; Cho, H.; Bae, Y.; Kolesar, J. M.; Kwon, G. S. *Mol. Pharmaceutics* **2011**, *8*, 1257.

(78) Luo, J.; Xiao, K.; Li, Y.; Lee, J.; Shi, L.; Tan, Y.; Xing, L.; Cheng, R. H.; Liu, G.; Lam, K. S. *Bioconjugate Chem.* **2010**, *21*, 1216.

(79) Li, Y.; Xiao, K.; Luo, J.; Lee, J.; Pan, S.; Lam, K. S. *J. Controlled Release* **2010**, *144*, 314.

(80) Li, X.; Qian, Y.; Liu, T.; Hu, X.; Zhang, G.; You, Y.; Liu, S. *Biomaterials* **2011**, *32*, 6595.

(81) Shenoy, D.; Little, S.; Langer, R.; Amiji, M. *Mol. Pharmaceutics* **2005**, *2*, 357.

(82) Chen, W.; Meng, F.; Li, F.; Ji, S.; Zhong, Z. *Biomacromolecules* **2009**, *10*, 1727.

(83) Lin, W.; Kim, D. *Langmuir* **2011**, *27*, 12090.

(84) Kim, S. H.; Tan, J. P. K.; Fukushima, K.; Nederberg, F.; Yang, Y. Y.; Waymouth, R. M.; Hedrick, J. L. *Biomaterials* **2011**, *32*.

(85) Hamaguchi, T.; Matsumura, Y.; Suzuki, M.; Shimizu, K.; Goda, R.; Nakamura, I.; Nakatomi, I.; Yokoyama, M.; Kataoka, K.; Kakizoe, T. *Brit. J. Cancer* **2005**, *92*, 1240.

(86) Matsumura, Y.; Kataoka, K. *Cancer Sci.* **2009**, *100*, 572.

(87) Kim, T. Y.; Kim, D. W.; Chung, J. Y.; Shin, S. G.; Kim, S. C.; Heo, D. S.; Kim, N. K.; Bang, Y. J. *Clin. Cancer Res.* **2004**, *10*, 3708.

(88) Lee, K. S.; Chung, H. C.; Im, S. A.; Park, Y. H.; Kim, C. S.; Kim, S. B.; Rha, S. Y.; Lee, M. Y.; Ro, J. *Breast Cancer Res. Tr.* **2008**, *108*, 241.

(89) Wang, J.; Liu, W.; Tu, Q.; Wang, J.; Song, N.; Zhang, N.; Nie, N.; Wang, J. *Biomacromolecules* **2011**, *12*, 228.

(90) Oerlemans, C.; Bult, W.; Bos, M.; Storm, G.; Nijsen, J. F. W.; Hennink, W. E. *Pharm. Res.* **2010**, *27*, 2569.

(91) Lee, N. S.; Lin, L. Y.; Neumann, W. L.; Freskos, J. N.; Karwa, A.; Shieh, J. J.; Dorshow, R. B.; Wooley, K. L. *Small* **2011**, *7*, 1998.

(92) Sun, G.; Lee, N. S.; Neumann, W. L.; Freskos, J. N.; Shieh, J. J.; Dorshow, R. B.; Wooley, K. L. *Soft Matter* **2009**, *5*, 3422.

(93) Lee, N. S.; Sun, G.; Lin, L. Y.; Neumann, W. L.; Freskos, J. N.; Karwa, A.; SHieh, J. J.; Dorshow, R. B.; Wooley, K. L. *J. Mater. Chem.* **2011**, *21*, 14193.

(94) Lee, N. S.; Sun, G.; Neumann, W. L.; Freskos, J. N.; Shieh, J. J.; Dorshow, R. B.; Wooley, K. L. *Adv. Mater.* **2009**, *21*, 1344.

(95) Sun, G.; Cui, H.; Lin, L. Y.; Lee, N. S.; Yang, C.; Neumann, W. L.; Freskos, J. N.; Shieh, J. J.; Dorshow, R. B.; Wooley, K. L. *J. Am. Chem. Soc.* **2011**, *133*, 8534.

(96) Sun, X. K.; Rossin, R.; Turner, J. L.; Becker, M. L.; Joralemon, M. J.; Welch, M. J.; Wooley, K. L. *Biomacromolecules* **2005**, *6*, 2541.

(97) Maeda, H.; Wu, J.; Sawa, T.; Matsumura, Y.; Hori, K. *J. Controlled Release* **2000**, *65*, 271.

(98) Hu, C. J.; Kaushal, S.; Cao, H. S. T.; Aryal, S.; Sartor, M.; Esener, S.; Bouvet, M.; Zhang, L. *Mol. Pharmaceutics* **2009**, *7*, 914.

(99) Kumagai, M.; Sarma, T. K.; Cabral, H.; Kaida, S.; Sekino, M.; Herlambang, N.; Osada, K.; Kano, M. R.; Nishiyama, N.; Kataoka, K. *Macromol. Rapid Commun.* **2010**, *31*, 1521.

(100) Cabral, H.; Matsumoto, Y.; Mizuno, K.; Chen, Q.; Murakami, M.; Kimura, M.; Terada, Y.; Kano, M. R.; Miyazono, K.; Uesaka, M.; Nishiyama, N.; Kataoka, K. *Nat. Nanotechnol.* **2011**, *6*, 815.

(101) Torchilin, V. P. *Adv. Drug Deliv. Rev.* **2005**, *57*, 95.

(102) Wang, T.; Petrenko, V. A.; Torchilin, V. P. *Mol. Pharmaceutics* **2010**, *7*, 1007.

(103) Lyczak, J. B.; Cannon, C. L.; Pier, G. B. *Clin. Microbiol. Rev.* **2002**, *15*, 197.

(104) Driscoll, J. A.; Brody, S. L.; Kollef, M. H. *Drugs* **2007**, *67*, 351.

(105) Drenkard, E. *Microbes and Infection* **2003**, *5*, 1213.

(106) Singh, P. K.; Schaefer, A. L.; Parsek, M. R.; Moninger, T. O.; Welsh, M. J.; Greenberg, E. P. *Nature* **2000**, *407*, 762.

(107) Livermore, D. M. *Clin. Infect. Dis.* **2002**, *34*, 634.

(108) Oliver, A.; Canton, R.; Campo, P.; Baquero, F.; Blazquez, J. *Science* **2000**, *288*, 1251.

(109) Miall, L. S.; McGinley, N. T.; Brownlee, K. G.; Conway, S. P. *Arch. Dis. Child.* **2001**, *84*, 160.

(110) Elizur, A.; Orscheln, R. C.; Ferkol, T. W.; Atkinson, J. J.; Dunne, W. M.; Buller, R. S.; Armstrong, J. R.; Mardis, E. R.; Storch, G. A.; Cannon, C. L. *Chest* **2007**, *131*, 1718.

(111) Mahenthiralingam, E.; Baldwin, A.; Vandamme, P. *J. Med. Microbiol.* **2002**, *51*, 533.

(112) Greenberg, D. E.; Marshall-Batty, K. R.; Brinster, L. R.; Zarember, K. A.; Shaw, P. A.; Mellbye, B. L.; Iversen, P. L.; Holland, S. M.; Geller, B. L. *J. Infect. Dis.* **2010**, *201*, 1822.

(113) Silver, S.; Phung, L. T.; Silver, G. *J. Ind. Microbiol. Biotechnol.* **2006**, *33*, 627.

(114) Klasen, H. J. *Burns* **2000**, *26*, 131.

(115) Secer, H. I.; Kural, C.; Kaplan, M.; Kilic, A.; Duz, B.; Gonul, E.; Izci, Y. *Pediatr. Neurosurg.* **2008**, *44*, 444.

(116) Melaiye, A.; Youngs, W. J. *Expert Opin. Ther. Pat.* **2005**, *15*, 125.

(117) Kollef, M. H.; Afessa, B.; Anzueto, A.; Veremakis, C.; Kerr, K. M.; Margolis, B. D.; Craven, D. E.; Roberts, P. R.; Arroliga, A. C.; Hubmayr, R. D.; Restrepo, M. I.; Auger, W. R.; Schinner, R.; Grp, N. I. *JAMA* **2008**, *300*, 805.

(118) Birla, S. S.; Tiwari, V. V.; Gade, A. K.; Ingle, A. P.; Yadav, A. P.; Rai, M. K. *Lett. Appl. Microbiol.* **2009**, *48*, 173.

(119) Fang, B.; Walther, A.; Wolf, A.; Xu, Y. Y.; Yuan, J. Y.; Muller, A. H. E. *Angew. Chem., Int. Ed.* **2009**, *48*, 2877.

(120) Gupta, A.; Matsui, K.; Lo, J. F.; Silver, S. *Nat. Med.* **1999**, *5*, 183.

(121) Silver, S. *FEMS. Microbiol. Rev.* **2003**, *27*, 341.

(122) Sambhy, V.; MacBride, M. M.; Peterson, B. R.; Sen, A. *J. Am. Chem. Soc.* **2006**, *128*, 9798.

(123) Aymonier, C.; Schlotterbeck, U.; Antonietti, L.; Zacharias, P.; Thomann, R.; Tiller, J. C.; Mecking, S. *Chem. Commun.* **2002**.

(124) Kascatan-Nebioglu, A.; Melaiye, A.; Hindi, K.; Durmus, S.; Panzner, M. J.; Hogue, L. A.; Mallett, R. J.; Hovis, C. E.; Coughenour, M.; Crosby, S. D.; Milsted, A.; Ely, D. L.; Tessier, C. A.; Cannon, C. L.; Youngs, W. J. *J. Med. Chem.* **2006**, *49*, 6811.

(125) Kascatan-Nebioglu, A.; Panzner, M. J.; Tessier, C. A.; Cannon, C. L.; Youngs, W. J. *Coord. Chem. Rev.* **2007**, *251*, 884.

(126) Panzner, M. J.; Deeraksa, A.; Smith, A.; Wright, B. D.; Hindi, K. M.; Kascatan-Nebioglu, A.; Torres, A. G.; Judy, B. M.; Hovis, C. E.; Hilliard, J. K.; Mallett, R. J.; Cope, E.; Estes, D. M.; Cannon, C. L.; Leid, J. G.; Youngs, W. J. *Eur. J. Inorg. Chem.* **2009**, 1739.

(127) Hindi, K. M.; Siciliano, T. J.; Durmus, S.; Panzner, M. J.; Medvetz, D. A.; Reddy, D. V.; Hogue, L. A.; Hovis, C. E.; Hilliard, J. K.; Mallet, R. J.; Tessier, C. A.; Cannon, C. L.; Youngs, W. J. *J. Med. Chem.* **2008**, *51*, 1577.

(128) Meers, P.; Neville, M.; Malinin, V.; Scotto, A. W.; Sardaryan, G.; Kurumunda, R.; Mackinson, C.; James, G.; Fisher, S.; Perkins, W. R. *J. Antimicrob. Chemother.* **2008**, *61*, 859.

(129) Hindi, K. M.; Ditto, A. J.; Panzner, M. J.; Medvetz, D. A.; Han, D. S.; Hovis, C. E.; Hilliard, J. K.; Taylor, J. B.; Yun, Y. H.; Cannon, C. L.; Youngs, W. J. *Biomaterials* **2009**, *30*, 3771.

(130) Hindi, K. M.; Panzner, M. J.; Tessier, C. A.; Cannon, C. L.; Youngs, W. J. *Chem. Rev.* **2009**, *109*, 3859.

(131) Li, Y.; Hindi, K.; Watts, K. M.; Taylor, J. B.; Zhang, K.; Li, Z. C.; Hunstad, D. A.; Cannon, C. L.; Youngs, W. J.; Wooley, K. L. *Chem. Commun.* **2010**, 121.

(132) Nicolle, L. E. *Infect. Med.* **2001**, *18*, 153.

(133) Foxman, B. *Am. J. Med.* **2002**, *113*, 53.

(134) Andriole, V. T.; Patterson, T. F. *Med. Clin. N. Am.* **1991**, *75*, 359.

(135) Kaper, J. B.; Nataro, J. P.; Mobley, H. L. T. *Nat. Rev. Microbiol.* **2004**, *2*, 123.

(136) Johnson, J. R. *Clin. Microbiol. Rev.* **1991**, *4*, 80.

(137) Jones, C. H.; Pinkner, J. S.; Roth, R.; Heuser, J.; Nicholes, A. V.; Abraham, S. N.; Hultgren, S. J. *Proc. Natl. Acad. Sci. U. S. A.* **1995**, *92*, 2081.

(138) Min, G. W.; Stolz, M.; Zhou, G.; Liang, F. X.; Sebbel, P.; Stoffler, D.; Glockshuber, R.; Sun, T. T.; Aebi, U.; Kong, X. P. *J. Mol. Biol.* **2002**, *317*, 697.

(139) Mulvey, M. A.; Lopez-Boado, Y. S.; Wilson, C. L.; Roth, R.; Parks, W. C.; Heuser, J.; Hultgren, S. J. *Science* **1998**, *282*, 1494.

(140) Zhou, G.; Mo, W. J.; Sebbel, P.; Min, G. W.; Neubert, T. A.; Glockshuber, R.; Wu, X. R.; Sun, T. T.; Kong, X. P. *J. Cell. Sci* **2001**, *114*, 4095.

(141) Martinez, J. J.; Mulvey, M. A.; Schilling, J. D.; Pinkner, J. S.; Hultgren, S. J. *EMBO. J.* **2000**, *19*, 2803.

(142) Hung, C. S.; Bouckaert, J.; Hung, D.; Pinkner, J. S.; Widberg, C.; DeFusco, A.; Auguste, C. G.; Strouse, R.; Langermann, S.; Waksman, G.; Hultgren, S. J. *Mol. Microbiol.* **2002**, *44*, 903.

(143) Anderson, G. G.; Palermo, J. J.; Schilling, J. D.; Roth, R.; Heuser, J.; Hultgren, S. J. *Science* **2003**, *301*, 105.

(144) Mulvey, M. A.; Schilling, J. D.; Hultgren, S. J. *Infect. Immun.* **2001**, *69*, 4572.

(145) Mysorekar, I. U.; Hultgren, S. J. *Proc. Natl. Acad. Sci. U. S. A.* **2006**, *103*, 14170.

(146) Nyström, A. M.; Wooley, K. L. *Acc. Chem. Res.* **2011**, *44*, 969.

(147) Xu, J. Q.; Sun, G. R.; Rossin, R. H., A.; Li, Z. C.; Fukukawa, K.; Messmore, B. W.; Moore, D. A.; Welch, M. J.; Hawker, C. J.; Wooley, K. L. *Macromolecules* **2007**, *40*, 2971.

(148) Champion, J. A.; Mitragotri, S. *Proc. Natl. Acad. Sci. U. S. A.* **2006**, *103*, 4930.

(149) Sharma, G.; Valenta, D. T.; Altman, Y.; Harvey, S.; Xie, H.; Mitragotri, S.; Smith, J. W. *J. Controlled Release* **2010**, *147*, 408.

(150) Hung, C. S.; Dodson, K. W.; Hultgren, S. J. *Nat. Protoc.* **2009**, *4*, 1230.

(151) Russell, A. D.; Hugo, W. B. *Med. Chem.* **1994**, *31*.

(152) Langermann, S.; Mollby, R.; Burlein, J. E.; Palaszynski, S. R.; Auguste, C. G.; DeFusco, A.; Strouse, R.; Schenerman, M. A.; Hultgren, S. J.; Pinkner, J. S.; Winberg, J.; Guldevall, L.; Soderhall, M.; Ishikawa, K.; Normark, S.; Koenig, S. *J. Infect. Dis.* **2000**, *181*, 774.

(153) Langermann, S.; Palaszynski, S.; Barnhart, M.; Auguste, G.; Pinkner, J. S.; Burlein, J.; Barren, P.; Koenig, S.; Leath, S.; Jones, C. H.; Hultgren, S. J. *Science* **1997**, *276*, 607.

(154) Tchesnokova, V.; Aprikian, P.; Kisiela, D.; Gowey, S.; Korotkova, N.; Thomas, W.; Sokurenko, E. *Infect. Immun.* **2011**, *79*, 3895.

(155) Euliss, L. E.; DuPont, J. A.; Gratton, S.; DeSimone, J. M. *Chem. Soc. Rev.* **2006**, *35*, 1095.

(156) Torchilin, V. P. *Eur. J. Pharm. Sci.* **2000**, *11*, S81.

(157) Champion, J. A.; Katare, Y. K.; Mitragotri, S. *Proc. Natl. Acad. Sci. U.S.A.* **2007**, *104*, 11901.

(158) Li, Z. B.; Kesselman, E.; Talmon, Y.; Hillmyer, M. A.; Lodge, T. P. *Science* **2004**, *306*, 98.

(159) Kubowicz, S.; Baussard, J. F.; Lutz, J. F.; Thunemann, A. F.; von Berlepsch, H.; Laschewsky, A. *Angew. Chem., Int. Ed.* **2005**, *44*, 5262.

(160) Li, Z. B.; Hillmyer, M. A.; Lodge, T. P. *Macromolecules* **2006**, *39*, 765.

(161) Liu, C.; Hillmyer, M. A.; Lodge, T. P. *Langmuir* **2008**, *24*, 12001.

(162) Liu, C.; Hillmyer, M. A.; Lodge, T. P. *Langmuir* **2009**, *25*, 13718.

(163) Lodge, T. P.; Bang, J. A.; Li, Z. B.; Hillmyer, M. A.; Talmon, Y. *Faraday Discuss.* **2005**, *128*, 1.

(164) Saito, N.; Liu, C.; Lodge, T. P.; Hillmyer, M. A. *Macromolecules* **2008**, *41*, 8815.

(165) Saito, N.; Liu, C.; Lodge, T. P.; Hillmyer, M. A. *ACS Nano* **2010**, *4*, 1907.

(166) Betthausen, E.; Drechsler, M.; Fortsch, M.; Schacher, F. H.; Muller, A. H. E. *Soft Matter* **2011**, *7*, 8880.

(167) Schacher, F.; Walther, A.; Ruppel, M.; Drechsler, M.; Muller, A. H. E. *Macromolecules* **2009**, *42*, 3540.

(168) Lutz, J. F.; Laschewsky, A. *Macromol. Chem. Phys.* **2005**, *206*, 813.

(169) Mao, J.; Ni, P. H.; Mai, Y. Y.; Yan, D. Y. *Langmuir* **2007**, *23*, 5127.

(170) Stavrouli, N.; Triftaridou, A. I.; Patrickios, C. S.; Tsitsilianis, C. *Macromol. Rapid Commun.* **2007**, *28*, 560.

(171) Walther, A.; Muller, A. H. E. *Chem. Commun.* **2009**, 1127.

(172) Skrabania, K.; Laschewsky, A.; von Berlepsch, H.; Bottcher, C. *Langmuir* **2009**, *25*, 7594.

(173) Jiang, T.; Wang, L. Q.; Lin, S. L.; Lin, J. P.; Li, Y. L. *Langmuir* **2011**, *27*, 6440.

(174) Gohy, J. F.; Ott, C.; Hoeppener, S.; Schubert, U. S. *Chem. Commun.* **2009**, 6038.

(175) von Berlepsch, H.; Bottcher, C.; Skrabania, K.; Laschewsky, A. *Chem. Commun.* **2009**, 2290.

(176) Skrabania, K.; von Berlepsch, H.; Bottcher, C.; Laschewsky, A. *Macromolecules* **2010**, *43*, 271.

(177) Walther, A.; Barner-Kowollik, C.; Muller, A. H. E. *Langmuir* **2010**, *26*, 12237.

(178) Uchman, M.; Stepanek, M.; Prochazka, K.; Mountrichas, G.; Pispas, S.; Voets, I. K.; Walther, A. *Macromolecules* **2009**, *42*, 5605.

(179) Hawker, C. J.; Wooley, K. L. *Science* **2005**, *309*, 1200.

(180) Bhojani, M. S.; Van Dort, M.; Rehemtulla, A.; Ross, B. D. *Mol. Pharmacol.* **2010**, *7*, 1921.

(181) Reddy, G. R.; Bhojani, M. S.; McConville, P.; Moody, J.; Moffat, B. A.; Hall, D. E.; Kim, G.; Koo, Y. E. L.; Woolliscroft, M. J.; Sugai, J. V.; Johnson, T. D.; Philbert, M. A.; Kopelman, R.; Rehemtulla, A.; Ross, B. D. *Clin. Cancer Res.* **2006**, *12*, 6677.

(182) Stupp, R.; Mason, W. P.; van den Bent, M. J.; Weller, M.; Fisher, B.; Taphoorn, M. J. B.; Belanger, K.; Brandes, A. A.; Marosi, C.; Bogdahn, U.; Curschmann, J.; Janzer, R. C.; Ludwin, S. K.; Gorlia, T.; Allgeier, A.; Lacombe, D.; Cairncross, J. G.; Eisenhauer, E.; Mirimanoff, R. O.; Van Den Weyngaert, D.; Kaendler, S.; Krauseneck, P.; Vinolas, N.; Villa, S.; Wurm, R. E.; Maillot, M. H. B.; Spagnolli, F.; Kantor, G.; Malhaire, J. P.; Renard, L.; De Witte, O.; Scandolaro, L.; Vecht, C. J.; Maingon, P.; Lutterbach, J.; Kobierska, A.; Bolla, M.; Souchon, R.; Mitine, C.; Tzuk-

Shina, T.; Kuten, A.; Haferkamp, G.; de Greve, J.; Priou, F.; Menten, J.; Rutten, I.; Clavere, P.; Malmstrom, A.; Jancar, B.; Newlands, E.; Pigott, K.; Twijnstra, A.; Chinot, O.; Reni, M.; Boiardi, A.; Fabbro, M.; Campone, M.; Bozzino, J.; Frenay, M.; Gijtenbeek, J.; Delattre, J. Y.; De Paula, U.; Hanzen, C.; Pavanato, G.; Schraub, S.; Pfeffer, R.; Soffietti, R.; Kortmann, R. D.; Taphoorn, M.; Torrecilla, J. L.; Grisold, W.; Huget, P.; Forsyth, P.; Fulton, D.; Kirby, S.; Wong, R.; Fenton, D.; Cairncross, G.; Whitlock, P.; Burdette-Radoux, S.; Gertler, S.; Saunders, S.; Laing, K.; Siddiqui, J.; Martin, L. A.; Gulavita, S.; Perry, J.; Mason, W.; Thiessen, B.; Pai, H.; Alam, Z. Y.; Eisenstat, D.; Mingrone, W.; Hofer, S.; Pesce, G.; Dietrich, P. Y.; Thum, P.; Baumert, B.; Ryan, G. *N. Engl. J. Med.* **2005**, *352*, 987.

(183) Armstrong, C. L.; Hunter, J. V.; Ledakis, G. E.; Cohen, B.; Tallent, E. M.; Goldstein, B. H.; Tochner, Z.; Lustig, R.; Judy, K. D.; Pruitt, A.; Mollman, J. E.; Stanczak, E. M.; Jo, M. Y.; Than, T. L.; Phillips, P. *Neurology* **2002**, *59*, 40.

(184) Misra, A.; Ganesh, S.; Shahiwala, A.; Shah, S. P. *J. Pharm. Sci.* **2003**, *6*, 252.

(185) Kroll, R. A.; Neuwelt, E. A. *Neurosurgery* **1998**, *42*, 1083.

(186) Steiniger, S. C. J.; Kreuter, J.; Khalansky, A. S.; Skidan, I. N.; Bobruskin, A. I.; Smirnova, Z. S.; Severin, S. E.; Uhl, R.; Kock, M.; Geiger, K. D.; Gelperina, S. E. *Int. J. Cancer* **2004**, *109*, 759.

(187) Stan, A. C.; Casares, S.; Radu, D.; Walter, G. F.; Brumeanu, T. D. *Anticancer Res.* **1999**, *19*, 941.

(188) Szakacs, G.; Paterson, J. K.; Ludwig, J. A.; Booth-Genthe, C.; Gottesman, M. M. *Nat. Rev. Drug Discov.* **2006**, *5*, 219.

(189) Brigger, I.; Dubernet, C.; Couvreur, P. *Adv. Drug Deliv. Rev.* **2002**, *54*, 631.

(190) Juillerate-Jeanneret, L. *Drug Discovery Today* **2008**, *13*, 1099.

(191) Kreuter, J. *Adv. Drug Deliv. Rev.* **2001**, *47*, 65.

(192) Byrne, F.; Betancourt, T.; Peppas-Brannon, L. *Adv. Drug Deliv. Rev.* **2008**, *60*, 1615.

(193) Koo, O. M.; Rubinstein, I.; Onyuksel, H. *Nanomed. Nanotechnol. Biol. Med.* **2005**, *1*, 193.

(194) Haley, B.; Frenkel, E. *Urol. Oncol.-Semin. Orig. Investig.* **2008**, *26*, 57.

(195) Nakanishi, T.; Fukushima, S.; Okamoto, K.; Suzuki, M.; Matsumura, Y.; Yokoyama, M.; Okano, T.; Sakurai, Y.; Kataoka, K. *J. Controlled Release* **2001**, *74*, 295.

(196) Talelli, M.; Iman, M.; Varkouhi, A. K.; Rijcken, C. J. F.; Schiffelers, R. M.; Etrych, T.; Ulbrich, K.; van Nostrum, C. F.; Lammers, T.; Storm, G.; Hennink, W. E. *Biomaterials* **2010**, *31*, 7797.

(197) Zhang, W.; Shi, Y.; Chen, Y. Z.; Hao, J. G.; Sha, X. Y.; Fang, X. L. *Biomaterials* **2011**, *32*, 5934.

(198) Folkman, J. *Blood* **2007**, *110*, 2786.

(199) Christian, S.; Pilch, J.; Akerman, M. E.; Porkka, K.; Laakkonen, P.; Ruoslahti, E. *J. Cell Biol.* **2003**, *163*, 871.

(200) Destouches, D.; El Khoury, D.; Hamma-Kourbali, Y.; Krust, B.; Albanese, P.; Katsoris, P.; Guichard, G.; Briand, J. P.; Courty, J.; Hovanessian, A. G. *PLoS One* **2008**, *3*, e2518.

(201) Porkka, K.; Laakkonen, P.; Hoffman, J. A.; Bernasconi, M.; Ruoslahti, E. *Proc. Natl. Acad. Sci. U.S.A.* **2002**, *99*, 7444.

(202) Makela, A. R.; Narvanen, A.; Oker-Blom, C. *J. Biotechnol.* **2008**, *134*, 20.

(203) Orringer, D. A.; Koo, Y. E. L.; Chen, T.; Kim, G.; Hah, H. J.; Xu, H.; Wang, S. Y.; Keep, R.; Philbert, M. A.; Kopelman, R.; Sagher, O. *Neurosurgery* **2009**, *64*, 965.

(204) Zhang, Y.; Yang, M.; Park, J. H.; Singelyn, J.; Ma, H. Q.; Sailor, M. J.; Ruoslahti, E.; Ozkan, M.; Ozkan, C. *Small* **2009**, *5*, 1990.

(205) Winer, I.; Wang, S. Y.; Lee, Y. E. K.; Fan, W. Z.; Gong, Y. S.; Burgos-Ojeda, D.; Spahlinger, G.; Kopelman, R.; Buckanovich, R. J. *Cancer Res.* **2010**, *70*, 8674.

(206) Zhang, K.; Rossin, R.; Hagooly, A.; Chen, Z. Y.; Welch, M. J.; Wooley, K. L. *J. Polym. Sci., Part A: Polym. Chem.* **2008**, *46*, 7578.

VITA

Yun Lin received her Bachelor of Science degree in chemistry from The University of Nebraska at Omaha in 2007. She entered the Ph.D program in the Chemistry Department at Washington University in St. Louis in June 2007 under the guidance of Professor Karen L. Wooley and received her Master of Science degree in July 2009. She moved to Texas A&M University with Dr. Wooley in November 2009 and continued her Ph.D studies. She obtained her Doctor of Philosophy degree in polymer chemistry in May, 2012.

Yun Lin may be reached at Department of Chemistry, Texas A&M University, P.O. Box 30012, College Station, TX 77842 and *via* email at yun.lin@chem.tamu.edu.